


Spring 5-1-2018

## Photoelectrochemical Studies on Non-Noble Metal Based Catalysts towards Tandem Solar Water Splitting

Arun Siddarth Sridhar  
*University of Southern Mississippi*

Follow this and additional works at: <https://aquila.usm.edu/dissertations>

 Part of the [Analytical Chemistry Commons](#), [Inorganic Chemistry Commons](#), [Materials Chemistry Commons](#), [Oil, Gas, and Energy Commons](#), [Other Chemistry Commons](#), and the [Physical Chemistry Commons](#)

---

### Recommended Citation

Sridhar, Arun Siddarth, "Photoelectrochemical Studies on Non-Noble Metal Based Catalysts towards Tandem Solar Water Splitting" (2018). *Dissertations*. 1528.  
<https://aquila.usm.edu/dissertations/1528>

This Dissertation is brought to you for free and open access by The Aquila Digital Community. It has been accepted for inclusion in Dissertations by an authorized administrator of The Aquila Digital Community. For more information, please contact [Joshua.Cromwell@usm.edu](mailto:Joshua.Cromwell@usm.edu).

Photoelectrochemical Studies on Non-Noble Metal Based Catalysts towards  
Tandem Solar Water Splitting

by

Arun Siddarth Sridhar

A Dissertation  
Submitted to the Graduate School,  
the College of Science and Technology  
and the Department of Chemistry and Biochemistry  
at The University of Southern Mississippi  
in Partial Fulfillment of the Requirements  
for the Degree of Doctor of Philosophy

Approved by:

Dr. Wujian Miao, Committee Chair

Dr. Song Guo

Dr. Douglas S. Masterson

Dr. Sarah E. Morgan

Dr. Karl J. Wallace

---

Dr. Wujian Miao  
Committee Chair

---

Dr. Vijay Rangachari  
Department Chair

---

Dr. Karen S. Coats  
Dean of the Graduate School

May 2018

COPYRIGHT BY

Arun Siddarth Sridhar

2018

*Published by the Graduate School*



THE UNIVERSITY OF  
**SOUTHERN**  
**MISSISSIPPI.**

## ABSTRACT

Photoelectrochemical (PEC) water splitting makes direct use of solar energy incident on semiconductor photoelectrodes, and it is a convenient, economic option to produce high purity hydrogen at low temperatures. The use of multiple light absorbers can increase overall solar energy utilization and provide a solution to the trade-off between overall band gap and band edge positioning of photoelectrodes specific to solar water oxidation and water reduction. The study of non-noble metal based catalysts for hydrogen evolution reaction (HER) and oxygen evolution reactions (OER) are essential for economic practical commercialization of photo-electrolyzers. This dissertation focuses on the use of a variety of non-noble transition metal chalcogenide based heterogeneous co-catalysts, and solution based water redox catalysts immobilized in polyoxometalate (POM) ensembles for water splitting in single and multiple absorber based systems. With a brief discussion on background and literature review in Chapter I, Chapter II reports PEC studies on TiO<sub>2</sub> photoanode in contact with solution-phase nickel-POM co-catalyst viz. K<sub>10</sub>H<sub>2</sub>[Ni<sub>5</sub>(OH)<sub>6</sub>(OH<sub>2</sub>)<sub>3</sub>(Si<sub>2</sub>W<sub>18</sub>O<sub>66</sub>)]•34H<sub>2</sub>O (Ni<sub>5</sub>-POM) for water oxidation, whereas Chapter III presents PEC studies on Cu<sub>x</sub>Se photocathode using cobalt-POM co-catalyst viz. [Co<sub>9</sub>(OH)<sub>3</sub>(H<sub>2</sub>O)<sub>6</sub>(HPO<sub>4</sub>)<sub>2</sub>(PW<sub>9</sub>O<sub>34</sub>)<sub>3</sub>]<sup>16-</sup> (Co<sub>9</sub>-POM) for water reduction. Chapters IV focuses on the use of electrodeposited transition metal selenide based co-catalysts for solar water reduction with Cu<sub>2</sub>O photocathodes, and Chapter V demonstrates the results of solar water oxidation using transition metal phosphide and selenide based co-catalysts electrodeposited on Fe<sub>2</sub>O<sub>3</sub> and BiVO<sub>4</sub> photoanodes. UV-Vis spectroscopy, scanning electron microscopy, and energy dispersive energy diffraction (EDX) were used for characterization of photoelectrodes and heterogeneous co-catalysts.

Synthesized metal-POMs were characterized using FT-IR and mass spectrometry. PEC measurements conducted under simulated solar irradiation provided evidence of significantly increased photocurrents, lowered onset potential and increased electron-hole separation in the presence of co-catalysts. Production of oxygen during solar water oxidation was verified with a dissolved oxygen sensor, and the stability of photoelectrodes were examined with multi-potential step experiments. An approximate 10 times increase in photocurrent (i.e., from  $\sim 0.008$  to  $0.08$  mA/cm<sup>2</sup>) was observed under zero biased water splitting at TiO<sub>2</sub> photoanodes upon the addition of Ni<sub>5</sub>-POM co-catalyst to the electrolyte solution. A maximum water reduction photocurrent of  $\sim 2$  mA/cm<sup>2</sup> at  $-0.45$  V vs Ag/AgCl was observed from Cu<sub>2</sub>O photocathodes with electrodeposited MnSe as water reduction co-catalyst. In Chapter VI, multiple-absorber configurations based on the above studied metal oxide photoanode/photocathode and a commercially available amorphous Si triple junction (3 jn Si) photoanode with Ni- or Co-POM solution-phase co-catalysts or heterogeneous transition metal chalcogenide co-catalysts are presented. The maximum zero bias photocurrents of  $-3.60$  and  $-0.60$  mA/cm<sup>2</sup> were observed from the tandem cells of 3 jn Si/Ni<sub>5</sub>-POM [photoanode] : FTO/Cu<sub>2</sub>O-MnSe [photocathode] and FTO/TiO<sub>2</sub>/Ni<sub>5</sub>-POM [photoanode] : FTO/Cu<sub>2</sub>O-MnSe [photocathode] water splitting systems, respectively. As of date, there have been limited studies on the use of non-noble metal POMs and chalcogenide based catalysts for PEC water splitting, and the large unbiased photocurrents obtained from this dissertation with respect to those shown in recent literature are clearly promising. Hence, the present studies provide a useful insight into the investigation of more efficient and commercially viable tandem water splitting systems in the future as discussed in Chapter VII.

## ACKNOWLEDGMENTS

I would like to express my earnest gratitude to my research advisor, Dr. Wujian Miao for allowing me to pursue my research interests throughout the graduate tenure. I want to acknowledge all the past and present members of the Miao research group, especially Dr. Tamanna Shanta, Dr. Yiliyasi Wusimanjiang and Dr. Pradip Bastola for their support and help.

My sincere appreciations to my committee members, Dr. Douglas S. Masterson, Dr. Karl J. Wallace, Dr. Sarah Morgan and Dr. Song Guo for always being encouraging and providing constructive discussions throughout the progress of this dissertation.

I would like to acknowledge partial financial support for the project from the National Science Foundation (NSF Career award CHE-0955878) and The University of Southern Mississippi (USM).

I want to thank Mr. Ryan Dufrene and Mrs. Jessica Douglas at the electron microscopy facility of the school of polymers and high-performance materials for their help in SEM and EDX characterization.

I would like to acknowledge the Department of Chemistry and Biochemistry, USM for the financial support and opportunity to pursue my graduate career.

Finally, I would like to thank my family and friends for their support during my PhD studies.

## DEDICATION

I would like to dedicate this Dissertation to Dr. A. P. J. Abdul Kalam, a pioneering rocket scientist, statesman and the former President of India who inspired millions of young students to pursue their dreams.

## TABLE OF CONTENTS

ABSTRACT.....	ii
ACKNOWLEDGMENTS .....	iv
DEDICATION.....	v
LIST OF TABLES .....	xii
LIST OF ILLUSTRATIONS.....	xiii
CHAPTER I – BACKGROUND AND LITERATURE REVIEW .....	1
1.1 Fundamentals of Photoelectrochemistry.....	1
1.1.1 Energy Levels in Semiconductors .....	1
1.1.2 The Semiconductor-Electrolyte Interface .....	2
1.2 Solar Hydrogen Economy and Photoelectrochemical Water Splitting.....	4
1.2.1 Global Energy Crisis and Solar Hydrogen Economy .....	4
1.2.2 PEC Water Splitting.....	5
1.2.3 Solar Water Splitting Approaches .....	7
1.2.3.1 The Single Absorber-Two Photon Approach .....	7
1.2.3.2 Multiple-Absorber Approaches for PEC Water Splitting.....	9
1.3 Cocatalysts for Solar Water Splitting .....	11
1.3.1 Role of Catalysts in PEC Water Splitting.....	11
1.3.2 Polyoxometalates (POMs).....	13
1.3.3 Metal chalcogenide based HER and OER catalyst .....	15



1.4 Overall Research Scope and Methodology .....	16
1.4.1 Preparation of Photoelectrode Films.....	17
1.4.1.1 Electrodeposition .....	17
1.4.1.2 Solution deposition/Spin coating .....	18
1.4.2 Physico-Chemical Characterization Techniques .....	18
1.4.3 Fundamentals of PEC Techniques .....	19
1.4.3.1 Illuminated Open Circuit Potential (OCP).....	19
1.4.3.2 PEC Impedance Spectroscopy .....	19
1.4.3.3 Mott Schottky analysis.....	21
1.4.3.4 Three Electrode $j$ - $V$ and Photocurrent Onset Measurements .....	22
1.4.3.5 Two Electrode Short Circuit and $j$ - $V$ .....	24
CHAPTER II – PHOTOELECTROCHEMICAL STUDIES ON EARTH ABUNDANT PENTANICKEL POLYOXOMETALATES AS CO-CATALYST FOR SOLAR WATER OXIDATION* .....	25
2.1 Introduction.....	25
2.2 Materials and Methods.....	27
2.2.1 Chemicals.....	27
2.2.2 Preparation of FTO/TiO <sub>2</sub> and Ni <sub>5</sub> -POM .....	28
2.2.3 Physico-Chemical Characterization of FTO/TiO <sub>2</sub> Photoanode .....	32
2.2.4 Photoelectrochemical Studies .....	32

2.3 Results and Discussion .....	33
2.3.1 Physico-Chemical Characterization.....	33
2.3.2 Three-Electrode Photocurrent Measurements And Electrochemical Impedance Spectroscopy .....	36
2.3.3 Unbiased two-electrode photocurrent measurements .....	43
2.3.4 Stability studies .....	44
2.3.5 Detection of Oxygen .....	46
2.4 Conclusion .....	50
 CHAPTER III - PHOTOELECTROCHEMICAL INVESTIGATIONS ON COBALT POLYOXOMETALATES AS CO-CATALYSTS FOR SOLAR WATER REDUCTION USING $\text{Cu}_x\text{Se}$ PHOTOCATHODES.....	
3.1 Introduction.....	52
3.2 Materials and Methods.....	55
3.2.1 Chemicals.....	55
3.2.2 Preparation of $\text{Cu}_x\text{Se}$ Photocathodes and $\text{Co}_9\text{-POM}$ .....	55
3.2.3 Physico-Chemical Characterization.....	56
3.2.4 Photoelectrochemical Measurements.....	56
3.3 Results and Discussion .....	57
3.3.1 Physico-Chemical Characterization.....	57
3.3.2 Photocurrent Measurements.....	61

3.3.3 Electrochemical Impedance Spectroscopy .....	66
3.3.4 Mott Schottky Plots.....	68
3.3.5 Stability Studies .....	71
3.4 Conclusion .....	73
CHAPTER IV – PHOTOELECTROCHEMICAL STUDIES ON TRANSITION METAL SELENIDE BASED CO-CATALYSTS FOR SOLAR WATER REDUCTION .....	75
4.1 Introduction.....	75
4.2 Materials and Methods.....	76
4.2.1 Materials .....	76
4.2.2 Physico-Chemical Characterization.....	76
4.2.3 Preparation of Photocathodes .....	77
4.2.4 Photoelectrochemical Studies .....	79
4.3 Results and Discussion .....	80
4.3.1 Photocurrent Measurements and Effect of Catalyst Thickness .....	80
4.3.2 Electrochemical Impedance Spectroscopic (EIS) Studies .....	87
4.4 Conclusion .....	88
CHAPTER V - PHOTOELECTROCHEMICAL STUDIES ON TRANSITION METAL PHOSPHIDE AND SELENIDE BASED PHOTOANODES FOR SOLAR WATER OXIDATION .....	90
5.1 Introduction.....	90

5.2 Materials and Methods.....	91
5.2.1 Materials .....	91
5.2.2 Preparation of Photoanodes .....	92
5.2.3 Physico-chemical Characterization.....	93
5.2.4 Photoelectrochemical Studies .....	94
5.3 Results and Discussion .....	95
5.3.1 Photocurrent Measurements.....	95
5.3.2 Electrochemical Impedance Spectroscopy and Mott Schottky Plots.....	99
5.3.3 Surface Morphology of FTO/BiVO <sub>4</sub> -Co <sub>x</sub> P Photoanodes .....	101
5.3.4 Dissolved Oxygen Measurements.....	102
5.3.5 Stability Studies .....	104
5.4 Conclusion .....	106
 CHAPTER VI – PHOTOELECTROCHEMICAL STUDIES ON TANDEM SOLAR WATER SPLITTING .....	
6.1 Introduction.....	108
6.2 Materials and Methods.....	110
6.2.1 Materials .....	110
6.2.2 Preparation of Photoelectrodes .....	110
6.2.3 Photoelectrochemical Measurements.....	110
6.3 Results and Discussion .....	112

6.3.1 Photocurrent Measurements.....	112
6.3.2 Dissolved Oxygen Measurements.....	118
6.3.3 Stability Studies .....	120
6.4 Conclusion .....	122
CHAPTER VII . SUMMARY AND FUTURE PERSPECTIVES.....	123
REFERENCES .....	127

## LIST OF TABLES

Table 2.1 Peak assignments for mass spectra of Ni <sub>5</sub> -POM shown in Figure 2.2 .....	32
Table 2.2 Comparison of photocurrents obtained at different TiO <sub>2</sub> based photoelectrodes for water splitting under various experimental conditions .....	38
Table 2.3 Oxygen Quantification and faradaic efficiency. ....	48
Table 3.1 Mass spectral peak assignments for Co <sub>9</sub> -POM catalyst.....	61
Table 3.2 Comparison of photocurrents obtained at different reported photocathodes for water splitting under various experimental conditions. ....	65
Table 4.1 Electrodeposition conditions for HER catalysts .....	79
Table 4.2 Se to Mn ratios in electrodeposited MnSe films.....	85
Table 6.1 Comparison of zero bias photocurrents of single absorber and tandem water splitting systems (conditions in Section 6.2.3). ....	113
Table 6.2 Zero bias photocurrent comparison .....	117

## LIST OF ILLUSTRATIONS

Figure 1.1 Energy bands in (a) intrinsic (b) n-type and (c) p-type semiconductor.....	2
Figure 1.2 Band energetics in an n-type semiconductor (Obtained with permission from Ref. 1) .....	3
Figure 1.3 Solar H <sub>2</sub> economy (Obtained with permission from Ref. 21). .....	4
Figure 1.4 Photoanode/metal cathode water splitting cell. ....	6
Figure 1.5 S <sub>2</sub> water splitting scheme. ....	8
Figure 1.6 Energy gaps of light absorbers (Obtained with permission from Ref. 29).....	9
Figure 1.7 D <sub>4</sub> water splitting scheme. ....	10
Figure 1.8 Photoanode/Photocathode tandem cell scheme. ....	10
Figure 1.9 Keggin and Dawson heteropolytungstates. Black: tungsten, Red: oxygen, Green: heteroatom (Obtained with permission from Ref. 50). ....	14
Figure 1.10 Structure of Ru <sub>4</sub> POM (Obtained with permission from Ref. 60).....	14
Figure 1.11 EIS equivalent circuit. ....	20
Figure 1.12 Nyquist Plot. ....	20
Figure 1.13 Mott Schottky Plot.....	22
Figure 1.14 Representative photocurrent plot.....	23
Figure 2.1 FT-IR spectra of Ni <sub>5</sub> -POM. (a) Entire spectral region from 400 to 4000 cm <sup>-1</sup> and (b) scaled in the fingerprint region of 400 to 1100 cm <sup>-1</sup> . ....	30
Figure 2.2 Mass spectra of Ni <sub>5</sub> -POM in different m/z regions. ....	31
Figure 2.3 SEM images of spin coated TiO <sub>2</sub> films on FTO substrate at (a) 206 X, (b) 704 X, and (c) 2.35 kX magnification. ....	34

Figure 2.4 Energy dispersive X-ray (EDX) spectrum of spin coated TiO <sub>2</sub> films on FTO substrate. The analysis was spotted on the TiO <sub>2</sub> microflake shown in the inset. ....	35
Figure 2.5 UV-vis spectra of (a) spin coated TiO <sub>2</sub> film on FTO substrate, (b) FTO substrate only, and (c) TiO <sub>2</sub> film obtained by subtracting (b) from (a). ....	36
Figure 2.6 Linear sweep voltammograms of TiO <sub>2</sub> /FTO photoanodes in the (a) absence and (b) presence of water oxidation catalyst Ni <sub>5</sub> -POM (20 μM in 0.050 M pH 9.0 borate buffer) under dark conditions and TiO <sub>2</sub> /FTO photoanodes in the (c) absence and (d) presence of water oxidation catalyst Ni <sub>5</sub> -POM (20 μM in 0.050 M pH 9.0 borate buffer) under simulated solar radiation. ....	39
Figure 2.7 Linear sweep voltammograms of FTO anodes in the (a) absence and (b) presence of water oxidation catalyst Ni <sub>5</sub> -POM (20 μM in 0.050 M pH 9.0 borate buffer) under dark. ....	39
Figure 2.8 Nyquist plots of TiO <sub>2</sub> /FTO photoanodes in the (A) absence and (B) presence of water oxidation catalyst Ni <sub>5</sub> -POM (20 μM in 0.050 M pH 9.0 borate buffer) under (a) simulated solar irradiation and (b) dark. (C) Nyquist plots of TiO <sub>2</sub> /FTO photoanodes in the (a) presence and (b) absence of water oxidation catalyst Ni <sub>5</sub> -POM (20 μM in 0.050 M pH 9.0 borate buffer) under simulated solar irradiation. ....	42
Figure 2.9 Unbiased two-electrode photocurrent plots of TiO <sub>2</sub> /FTO photoanodes under intermittent simulated solar light in the (a) absence and (b) presence of water oxidation catalyst Ni <sub>5</sub> -POM (20 μM in 0.050 M pH 9.0 borate buffer). ....	44
Figure 2.10 Stability studies of TiO <sub>2</sub> /FTO photoanodes under simulated solar light in the presence of water oxidation catalyst Ni <sub>5</sub> -POM (20 μM in 0.050 M pH 9.0 borate buffer)	



for the time region of (a) 0-200 s, (b) 1800-2000 s, and (c) 3800-4000 s. Potentials applied at step 1: 0 V vs Ag/AgCl and step 2: 1.10 V vs Ag/AgCl.....	46
Figure 2.11 Dissolved oxygen (DO) for (a) borate buffer blank, (b) during multi-potential step experiments in the absence and (c) presence of water oxidation catalyst Ni <sub>5</sub> -POM (20 μM in 0.050 M pH 9.0 borate buffer) under dark conditions, (d) TiO <sub>2</sub> /FTO photoanodes in the absence and (e) presence of water oxidation catalyst Ni <sub>5</sub> -POM (20 μM in 0.050 M pH 9.0 borate buffer) under simulated solar irradiation.....	49
Figure 3.1 Molecular structure of Co <sub>9</sub> -POM (WO <sub>6</sub> : Grey Octahedra, CoO <sub>6</sub> : Pink Octahedra, PO <sub>4</sub> : Yellow Tetrahedra). Obtained with permission from from Ref. 131. ...	54
Figure 3.2 SEM images of electrodeposited Cu <sub>x</sub> Se films with a deposition potential of -0.5 V vs Ag/AgCl on FTO substrate at (a) 1.50 KX, and (b) 2.60 KX. ....	57
Figure 3.3 EDX maps of electrodeposited FTO/Cu <sub>x</sub> Se films on FTO substrate at (a) Cu and (b) Se, using (c) the sample area. (d) EDX spectrum of FTO/Cu <sub>x</sub> Se.....	58
Figure 3.4 UV-vis spectra of Cu <sub>x</sub> Se film on FTO substrate.....	60
Figure 3.5 Mass spectra of Co <sub>9</sub> -POM catalyst in (a) 1900-1800 and (b) 940-980 m/z range.....	60
Figure 3.6 Dependence of HER current density at -0.40 V vs Ag/AgCl on Cu <sub>x</sub> Se electrodeposition potential. ....	62
Figure 3.7 Linear sweep voltammograms of FTO/Cu <sub>x</sub> Se photocathodes in the (a) absence and (b) presence of water reduction catalyst Co <sub>9</sub> -POM (20 μM in 0.050 M pH 9.0 borate buffer) under dark conditions and FTO/Cu <sub>x</sub> Se photocathodes in the (c) absence and (d) presence of water reduction catalyst Co <sub>9</sub> -POM (20 μM in 0.050 M pH 9.0 borate buffer) under simulated solar radiation at a scan rate 0.020 V/s.....	64

Figure 3.8 Bode plots of FTO/Cu<sub>x</sub>Se photocathodes in the (A) absence and (B) presence of water reduction catalyst Co<sub>9</sub>-POM (20 μM in 0.050 M pH 9 borate buffer) under (a) simulated solar irradiation and (b) dark. (C) Bode plots of FTO/Cu<sub>x</sub>Se photocathodes in the (a) presence and (b) absence of water reduction catalyst Co<sub>9</sub>-POM (20 μM in 0.050 M pH 9.0 borate buffer) under simulated solar irradiation. .... 68

Figure 3.9 Mott Schottky plots of FTO/Cu<sub>x</sub>Se photocathodes in the (a) presence and (b) absence of water reduction catalyst Co<sub>9</sub>-POM (20 μM in 0.050 M pH 9.0 borate buffer) under simulated solar irradiation. .... 70

Figure 3.10 Stability studies of FTO/Cu<sub>x</sub>Se photocathodes under simulated solar light in the presence of reduction with catalyst Co<sub>9</sub>-POM (20 μM in 0.050 M pH 9.0 borate buffer) for the time region of (A) 0-600 s, (b) 1500-2000 s, Potentials applied at step 1: 0 V vs Ag/AgCl and step 2: -0.4 V vs Ag/AgCl. (c) Linear sweep voltammogram recorded after stability study..... 73

Figure 4.1 UV-Vis spectroscopic plot of FTO/Cu<sub>2</sub>O (Blanked with FTO substrate)..... 78

Figure 4.2 PEC cell representation for water splitting using FTO/Cu<sub>2</sub>O-MnSe photocathodes. .... 80

Figure 4.3 Relationship between HER current density at -0.45 V (A,C) or -0.40 V (B) vs Ag/AgCl and catalyst electrodeposition time for (A) FTO/Cu<sub>2</sub>O-MnSe, (B) FTO/Cu<sub>2</sub>O-Co<sub>x</sub>Se-Ni<sub>y</sub>Se and (C) FTO/Cu<sub>2</sub>O-WSe<sub>x</sub>..... 82

Figure 4.4 SEM images of MnSe films electrodeposited for 20 min on FTO/Cu<sub>2</sub>O substrate at (a) 5.00 KX and (b) 15.00 KX. .... 84

Figure 4.5 SEM images of MnSe films electrodeposited for 40 min on FTO/Cu<sub>2</sub>O substrate at (a) 5.00 KX and (b) 15.00 KX. .... 84

Figure 4.6 Energy dispersive X ray spectra of MnSe films electrodeposited on FTO/Cu <sub>2</sub> O for (a) 20 min and (b) 40 min.....	85
Figure 4.7 Linear sweep voltammogram of (a) FTO/Cu <sub>2</sub> O under dark compared to (b) FTO/Cu <sub>2</sub> O, (c) FTO/Cu <sub>2</sub> O-Co <sub>x</sub> Se-Ni <sub>y</sub> Se, (d) FTO/Cu <sub>2</sub> O-MnSe under simulated solar irradiation.....	86
Figure 4.8 Linear sweep voltammogram of (a) FTO/Cu <sub>2</sub> O and (b) FTO/Cu <sub>2</sub> O-WSe <sub>x</sub> under dark, compared to (c) FTO/Cu <sub>2</sub> O and (d) FTO/Cu <sub>2</sub> O-WSe <sub>x</sub> under simulated solar irradiation.....	87
Figure 4.9 Electrochemical impedance spectroscopic plots of (a) FTO/Cu <sub>2</sub> O-MnSe compared to (b) FTO/Cu <sub>2</sub> O under simulated solar irradiation. ....	88
Figure 5.1 UV-vis spectra of (a) FTO/Fe <sub>2</sub> O <sub>3</sub> and (b) FTO/BiVO <sub>4</sub> photoanodes (Blanked with FTO).....	93
Figure 5.2 Representative cell scheme for photoelectrochemical water splitting using FTO/BiVO <sub>4</sub> -Co <sub>x</sub> P photoanodes. ....	94
Figure 5.3 Catalyst deposition time (thickness) vs current density for FTO/Fe <sub>2</sub> O <sub>3</sub> -FeSe photoanodes at 0.70 V vs Ag/AgCl. ....	95
Figure 5.4 Catalyst deposition linear scans (thickness) vs current density for FTO/BiVO <sub>4</sub> -Co <sub>x</sub> P photoanodes at 0.70 V vs Ag/AgCl. ....	96
Figure 5.5 Linear sweep voltammograms of FTO/Fe <sub>2</sub> O <sub>3</sub> photoanodes in the (a) presence and (b) absence of FeSe under simulated solar radiation, as compared to those in the (c) presence (d) absence of FeSe under dark conditions. See Section 5.2.4 for experimental conditions.....	97

Figure 5.6 (A) Linear sweep voltammograms of FTO/BiVO <sub>4</sub> photoanodes in the(a) presence of and (b) absence of Co <sub>x</sub> P under dark conditions. (B) Linear sweep voltammograms of FTO/BiVO <sub>4</sub> photoanodes in the (a) presence and (b) absence of Co <sub>x</sub> P under simulated solar irradiation. ....	98
Figure 5.7 Electrochemical Impedance spectra of FTO/FeSe photoanodes in the (a) presence and (b) absence of FeSe under simulated solar irradiation. ....	99
Figure 5.8 Mott Schottky plots of FTO/BiVO <sub>4</sub> photoanodes in the (a) absence of and (b) presence of Co <sub>x</sub> P under simulated solar irradiation. ....	101
Figure 5.9 SEM images of FTO/BiVO <sub>4</sub> -Co <sub>x</sub> P photoanodes at (a) 4KX and (b) 10 KX. ....	102
Figure 5.10 EDX spectrum of FTO/BiVO <sub>4</sub> -Co <sub>x</sub> P photoanode. ....	102
Figure 5.11 Dissolved oxygen measurements FTO/BiVO <sub>4</sub> photoanodes in the (a) absence and (b) presence of Co <sub>x</sub> P under simulated solar irradiation. ....	103
Figure 5.12 Stability studies of FTO/BiVO <sub>4</sub> -Co <sub>x</sub> P photoanodes under simulated solar light for the time region of (A) 0-3400 s, (b) 0-400 s, and (c) 3000-3400 s. Potentials applied at a: 1.10 V vs Ag/AgCl and b: 0 V vs Ag/AgCl. ....	106
Figure 6.1 Representative scheme for solar water splitting using 3jn Si/Ni <sub>5</sub> -POM [photoanode]:FTO/Cu <sub>2</sub> O-MnSe [photocathode] water splitting cell. ....	112
Figure 6.2 Zero bias photocurrent measurements on 3jn Si/Ni <sub>5</sub> -POM [photoanode]:FTO/Cu <sub>2</sub> O-MnSe [photocathode]. L: light irradiation, D: dark conditions. Conditions mentioned in Section 6.2.3. ....	115
Figure 6.3 Zero bias photocurrent measurements on FTO/TiO <sub>2</sub> /Ni <sub>5</sub> -POM [photoanode]:FTO/Cu <sub>2</sub> O-MnSe [photocathode]. L: light irradiation, D: dark conditions. Conditions mentioned in Section 6.2.3. ....	115

Figure 6.4 Two-electrode photocurrent measurements on (a) 3jn Si/Ni<sub>5</sub>-POM [photoanode]:FTO/Cu<sub>2</sub>O-MnSe [photocathode], (b) 3jn Si [photoanode]:FTO/Cu<sub>2</sub>O-MnSe [photocathode], (c) 3jn Si/Ni<sub>5</sub>-POM [photoanode]:Pt [cathode] and (d) 3jn Si [photoanode]: Pt [cathode] under simulated solar irradiation. Conditions mentioned in Section 6.2.3..... 116

Figure 6.5 Two electrode dissolved oxygen measurements on (a) 3jn Si/Ni<sub>5</sub>-POM [photoanode]:Pt [cathode] (b) FTO/TiO<sub>2</sub>/Ni<sub>5</sub>-POM [photoanode]:FTO/Cu<sub>2</sub>O-MnSe [photocathode] (c) 3jn Si/Ni<sub>5</sub>-POM [Photoanode]:FTO/Cu<sub>2</sub>O-MnSe [Photocathode]. Conditions mentioned in Section 6.2.3. .... 119

Figure 6.6 (A) Multi-potential step stability studies of 3jn Si/Ni<sub>5</sub>-POM [Photoanode]:FTO/Cu<sub>2</sub>O-MnSe [Photocathode] under simulated solar light. Potentials applied at a. 1.10 V and b. 0 V. (B) Zero bias photocurrent plot of 3jn Si/Ni<sub>5</sub>-POM [Photoanode]:FTO/Cu<sub>2</sub>O-MnSe [Photocathode] after stability measurements. L: light irradiation, D: dark conditions. Conditions mentioned in Section 6.2.3..... 121

## CHAPTER I – BACKGROUND AND LITERATURE REVIEW

### 1.1 Fundamentals of Photoelectrochemistry

#### 1.1.1 Energy Levels in Semiconductors

The energy levels in semiconductors are dense and form broad energy bands instead of discrete molecular orbital energy levels. Solid state semiconductors have two distinct energy bands viz. the valance band (VB) and the conduction band (CB). The VB is the lower energy level that is occupied, whereas the CB is the higher energy level that is primarily empty. The distance between VB and CB is called the energy band gap ( $E_g$ ) and it is equivalent to the energy required to excite electrons from the VB to CB. The Fermi level ( $E_F$ ) is the energy between the VB and the CB, at which there is a 50% probability of finding an electron. It can be equated to the electrochemical potential in a particular phase.

Two kinds of electronic charge carriers are possible in the case of semiconductors. In the event of electron excitation from the VB to CB, a vacancy or hole is created in the VB. This results in an equal number of oppositely charged carriers in the case of intrinsic semiconductors, and the Fermi Level lies in the middle of the energy band gap, as shown in Figure 1.1 (a).

In the case of extrinsic semiconductors, addition of altrivalent impurities (doping) leads to an uneven number of electrons and holes, resulting in the formation of majority and minority charge carriers. Extrinsic semiconductors in which electrons are the majority charge carriers are called “n-type”, whereas those that have positive charges or holes as the majority charge carriers are called “p-type. In addition to doping, extrinsic semiconductors can also be formed due to non-stoichiometry and other factors such as

crystal defects and trap states. The Fermi level  $E_F$  lies close to the CB and VB edge for n-type and p-type extrinsic semiconductors respectively, as shown in Figures 1.1 (b) and 1.1 (c).

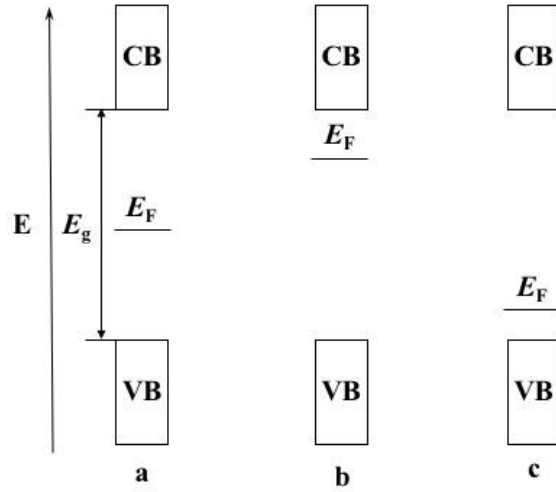


Figure 1.1 Energy bands in (a) intrinsic (b) n-type and (c) p-type semiconductor.

### 1.1.2 The Semiconductor-Electrolyte Interface

The formation of space charge is key feature of semiconductors, and plays an important role in energy conversion devices where efficient separation of photogenerated electrons and holes is crucial. Figure 1.2.<sup>1</sup> depicts the band energetics for an n-type semiconductor in contact with aqueous electrolyte. When a semiconductor electrode is placed in solution, there arises a difference in energy between the fermi level of the semiconductor and electrochemical potential of the electrolyte solution ( $E^\circ(\text{H}_2\text{O}/\text{O}_2)$ ). This results transfer of charge between them until equilibrium is established. As a result of charge flow, the electrode has excess positive charge over the depletion layer of width  $W$ , and the solution has an excess negative charge across a much narrower Helmholtz layer close to the electrode.

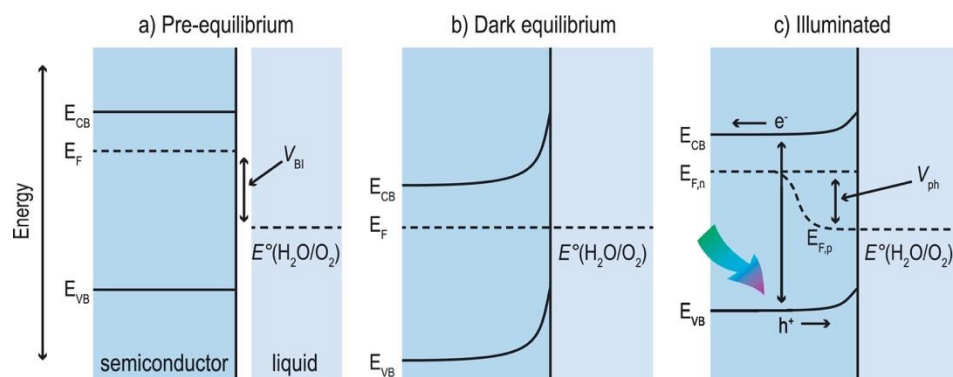


Figure 1.2 Band energetics in an n-type semiconductor (Obtained with permission from Ref. 1)

Upon light illumination, the production of photogenerated charge carriers leads to a non-equilibrium population of electrons and holes. This results in the formation of quasi Fermi levels  $E_{F,n}$  for electrons and  $E_{F,p}$  for holes. The difference between  $E_{F,n}$  and  $(E^\circ(\text{H}_2\text{O}/\text{O}_2))$  is the photogenerated voltage ( $V_{\text{ph}}$ ) for the n-type semiconductor. The electric field created causes the photo-generated free minority carriers (holes) to move into solution, where they can take part in redox reactions. Hence, n-type semiconductors are typically used as photoanodes. p-type semiconductors are similar but behave in an inverse manner, and are used as photocathodes. An ideal photoelectrochemical system will have to be designed in such a way that the photogenerated charge carriers are effectively separated to take part in redox reactions (water electrolysis in the case of this work).



## 1.2 Solar Hydrogen Economy and Photoelectrochemical Water Splitting

### 1.2.1 Global Energy Crisis and Solar Hydrogen Economy

The provision of sufficient alternate energy to meet up with living standards in the wake of rapid fossil fuel consumption is one of the foremost present day scientific challenges. A 30 terawatt (TW,  $10^{12}$  W) global power necessity to provide for a population of 7 billion people by the year 2050 has been estimated,<sup>2-3</sup> and conventional fuel sources such as coal, oil, and natural gas have been predicted to deplete completely within the next 150 years. Moreover, as stated by the international energy agency the production of conventional oil has already peaked by the year 2006.<sup>4</sup>

In terms of global power generating capacity, solar energy ranks the highest amongst all sustainable energy sources with a potential to deliver over 20 TW.<sup>5-6</sup> However, solid state photovoltaics faces challenges related to intermittent nature of solar power and area requirements for grid based storage.<sup>7-8</sup> Thus, the storage of chemical energy in the form of fuel is a viable option.<sup>9-12</sup>

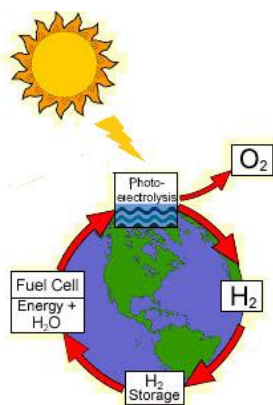


Figure 1.3 Solar H<sub>2</sub> economy (Obtained with permission from Ref. 21).

Hydrogen stands at the foremost amongst all conventional fuels, having the highest volumetric energy density,<sup>5-6</sup> in addition to being a non-carbon energy source. Hence, it has been globally accepted as an emerging future power source with a latent potential to deliver more than 50% of the world's energy need by the year 2050.

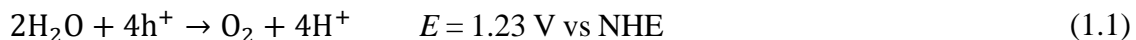
There are several methods<sup>13-14</sup> that are being pursued for solar to hydrogen conversion, such as photovoltaic electrolysis,<sup>15</sup> thermochemical conversion,<sup>16-17</sup> photobiological hydrogen production,<sup>18-19</sup> and PEC water splitting.<sup>12, 20</sup>

Photoelectrochemistry combines the abundance of solar energy with the low temperature, controlled and localized nature of electrochemical process design, offering an effective platform for the production of hydrogen from water, which is one of the earth's most abundant natural resources. Electrochemically produced molecular hydrogen is in its purest form available, rendering it the best fuel and process gas of choice for fuel cell and industrial applications. Hence, it is the best choice for development of a cyclic solar hydrogen economy<sup>21</sup> (Figure 1.3) in future integrated solar water electrolysis-fuel cell systems, beginning with the splitting of water (in photoelectrolyser) and ending with generation of electricity and regeneration of water (in fuel cell).

### **1.2.2 PEC Water Splitting**

PEC water splitting is a versatile strategy for the direct solar to hydrogen conversion at room temperature.<sup>12</sup> At the heart of the system is the semiconductor electrode which absorbs solar photons resulting in the formation of separated interfacial electron hole pairs. Holes are utilized for oxidation of water in the anodic half cell (Eq. 1.1), whereas electrons reduce water to form hydrogen at the cathode (Eq. 1.2). Figure

1.4 depicts a PEC water splitting cell with a semiconductor photoanode and metal cathode.



As seen from Eqs. 1.1 and 1.2, the PEC splitting of water has a standard potential of 1.23 V vs NHE. This potential, however, does not account for added “overpotential”, which is the addition potential barrier arising from activation, concentration, and ohmic barriers. Thus under real conditions, the potential required for the splitting of water is in the range of 1.9-2 V.<sup>12, 20</sup>

In an ideal PEC system, the electrochemical bias for water splitting is provided by potential arising from photogenerated charge carrier generation and separation at the semiconductor electrolyte interface. However, this pursuit has been in progress for four decades.<sup>11, 20, 22-24</sup>

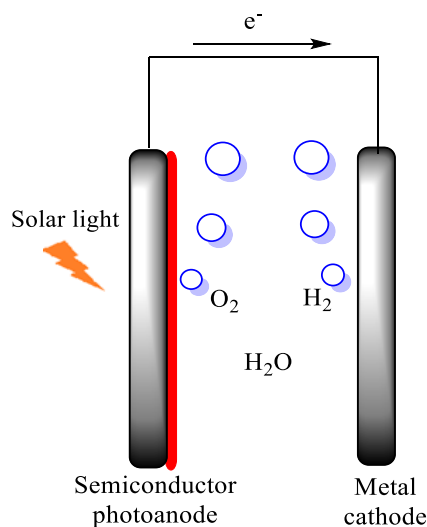


Figure 1.4 Photoanode/metal cathode water splitting cell.

## 1.2.3 Solar Water Splitting Approaches

### 1.2.3.1 The Single Absorber-Two Photon Approach

The single absorber with two photon (S2) approach is the most well explored strategies for solar water splitting.<sup>20,25</sup> This strategy works on the concept that a single light absorber (photoanode or photocathode) absorbs two photons, resulting in the formation of one molecule of H<sub>2</sub>. In other words, each photon absorbed is assumed to produce an electron-hole pair, and four electron-hole pairs are required for water splitting to generate one molecule of O<sub>2</sub> and two molecules of H<sub>2</sub>. A number of comprehensive reviews have been published that discuss the splitting of water using single photoanodes or photocathodes.<sup>20, 24, 26</sup>

Figure 1.5 provides the overall scheme for S2 water splitting in a photoanode/metal cathode system, where the excitation of the photoanode produces electron-hole pairs. While holes are utilized for water oxidation, electrons are transported to metal cathode for hydrogen evolution. The molecular mechanism of water splitting on semiconductor photoanodes has been a subject of contrasted scientific views. However, it has been generally accepted that the reaction proceeds through nucleophilic attack of water molecules on surface trapped holes at the photoanode surface.<sup>27-28</sup> This dissertation will not focus on molecular mechanisms, and place more emphasis on design efficient systems for photon absorption, carrier generation, and charge transport for PEC water splitting.

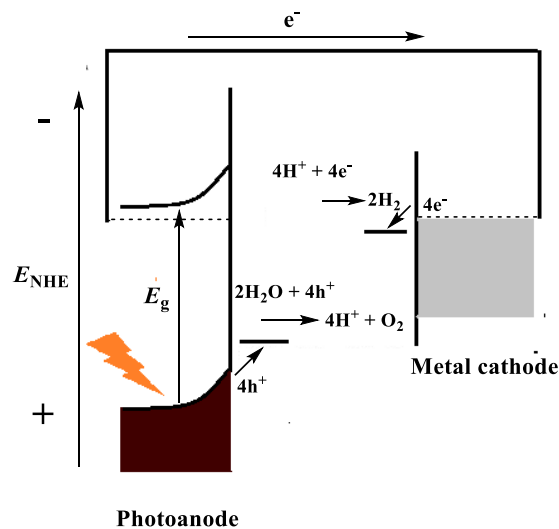


Figure 1.5 S2 water splitting scheme.

On the outset, this approach would seem versatile, since the standard potential of water splitting is 1.23 V vs NHE on a thermodynamic standpoint, which could be effectively transgressed by any light absorber having an optical band gap greater than 1.23 eV. However, the real scenario is complicated by a diverse variety of factors, which include (1) Availability of semiconductor light absorbers whose Fermi levels cross both hydrogen evolution and oxygen evolution potentials, yet do not fall in visible absorption range (Figure. 1.6)<sup>29</sup>, (2) Lack of photostability in band edge favourable light absorbers, (3) Higher energy to be provided for water splitting by single absorbers systems due to overpotential losses, and light absorption losses from chemical potential of excited state  $\Delta\mu_{\text{ex}}$ <sup>26</sup> being lesser than band gap  $E_g$  ( $\Delta\mu_{\text{ex}} = 0.75E_g$  for standard solar intensities<sup>30</sup>), and (4) Narrow and inefficient utilization of energy from the solar spectrum.

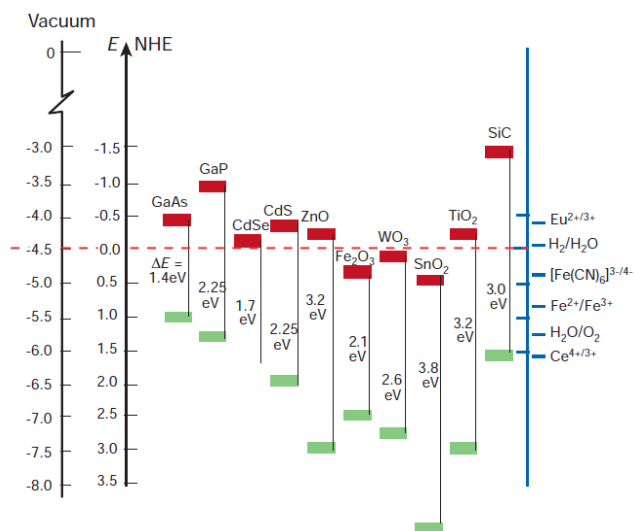


Figure 1.6 Energy gaps of light absorbers (Obtained with permission from Ref. 29).

Considering these realistic losses, the upper limit of solar fuel conversion using the S2 approach has been estimated as 11.6%,<sup>31</sup> although achieving even 10% solar to hydrogen conversion efficiency (STH) appears to be difficult.<sup>32</sup> Hence, one of the best future directions would be on the use of effective bio-mimetic catalysts for S2 approaches and make progress in the development of tandem and multiple-absorber systems.

### 1.2.3.2 Multiple-Absorber Approaches for PEC Water Splitting

Water splitting can be considered as a four-electron process, which requires the absorption of four photons per molecule of oxygen. If each light absorber can absorb two photons, the use of two absorbers will provide needed four photons for water splitting. The strategy that involves the use of two light absorbing semiconductors stacked or arranged side by side is known as the dual-absorber four photon (D4) approach.<sup>32</sup> The use of multiple light absorbers would increase the efficiency of solar to hydrogen conversion by increasing light absorption range and providing higher photogenerated energy bias for overall water splitting. In a typical wired photoanode/photocathode based D4 tandem

approach (Figure 1.7), the n-type semiconductor photoanode (with band gap  $E_{g1}$ ) and p-type photocathode (with band gap  $E_{g2}$ ) are used in tandem.

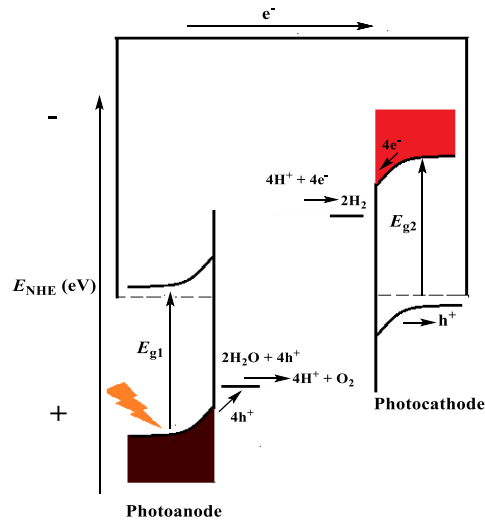


Figure 1.7 D4 water splitting scheme.

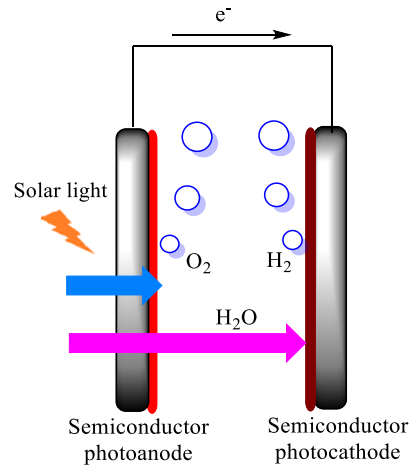


Figure 1.8 Photoanode/Photocathode tandem cell scheme.

The photoanode and photocathode can be adequately chosen so that their band edges cross the electrochemical potential for hydrogen or oxygen evolution. That is, the valance band of the photoanode must be below water oxidation potential (more positive) and conduction band of the photocathode must be above the potential (more negative) for

water reduction (Figure 1.7). As shown in Figures 1.7 and 1.8 with a top photoanode configuration, solar photons with energy greater than  $E_{g1}$  are absorbed to evolve oxygen, and the rest are utilized by the bottom cell with band gap  $E_{g2}$  for hydrogen evolution. A total of four electrons and holes are produced through simultaneous absorption of two photons from each light absorber. The  $\text{Cu}_2\text{O}/\text{BiVO}_4$  tandem cell reported recently by Gratzel et al. is a classic example of the photoanode/photocathode type D4 water splitting cell.<sup>33</sup>

### **1.3 Cocatalysts for Solar Water Splitting**

#### **1.3.1 Role of Catalysts in PEC Water Splitting**

Catalysts play a vital role in enhancing the efficiency of solar to hydrogen conversion by PEC water splitting.<sup>3, 34-35</sup>

Following are some of the advantages of using oxygen evolution reaction (OER) and hydrogen evolution reaction (HER) compounds:

1. Reduction of kinetic activation overpotential for water oxidation and reduction. This increases onset voltage range and reduces onset potential, improving the probability of short circuit water splitting by a wide range of photocatalysts.
2. Enhanced charge separation and prevention of electron-hole recombination through capture and utilization of charges by the catalyst for water oxidation and reduction. This, in turn leads to increased photocurrent in the presence of catalyst.
3. Protection of semiconductor photoelectrodes against photocorrosion, improving their durability and lifetime.



In a PEC water splitting reaction, majority of required electrochemical potential bias for water splitting is provided by light absorption and charge separation on the semiconductor electrode surface. HER/OER reduces the electrochemical potential required for photocurrent onset and water splitting by the semiconductor by means of reducing the kinetic activation overpotential for the reaction. Due to reduced activation overpotential, the bias required for water splitting becomes closer to its theoretical value (~1.23 V), increasing the possibility for the semiconductor electrode to split water and generate photocurrent by itself without any externally applied potential. Since HER/OER catalysts reduce activation overpotential as a result of their reaction pathways, they are termed “electrocatalysts” in the fundamental sense. However, the semiconductor electrode itself may be basically considered as a photocatalyst in an ideal unassisted water splitting case, since it provides the complete activation energy/potential bias for water splitting. Considering this argument, the HER/OER catalyst has been referred to by the term “photoelectrocatalyst” or simply “catalyst” in certain reports, since it is a secondary catalyst and utilizes photogenerated electron-hole pairs from the photocatalyst for its water oxidation/reduction pathways. Due to its contribution to photocatalysis and also electrocatalysis, the OER/HER compound is alternatively quoted as “catalyst” or “electrocatalyst” in this dissertation. Both terms have been used in peer reviewed scientific literature on PEC water splitting systems.<sup>12, 36-39</sup>

Pt has been the most studied and efficient industrial electrocatalysts for hydrogen evolution reaction, with its activity arising from near zero free energy of hydrogen atom adsorption.<sup>40-41,42</sup> Similarly, IrO<sub>2</sub><sup>43-45</sup> and RuO<sub>2</sub><sup>44, 46-48</sup> have been the highest performing electrocatalysts for water oxidation reaction. However, the prohibitive cost of these noble

metal based catalysts necessitates the need for the development of alternate earth abundant non-noble metal based catalysts for water splitting.

Present research on earth abundant catalysts for PEC water splitting focuses primary on the use of Ni, Mn, and Co based mono-metal oxides and hydroxides.<sup>3</sup> This is due to their redox properties and stability comparable to noble metals. However, current reports on the use of these catalysts for PEC cells do not focus on mixed metal oxides or encapsulation in molecular architectures, strategies which could increase number of active sites in addition to reducing loading and improving stability. The photosystem II (PS II) mimic cobalt phosphate oxygen evolving compound (Co-OEC) has been used as an efficient self-healing catalyst or in conjunction with photoanodes for wireless or regular water splitting.<sup>39, 49</sup>

This dissertation focuses on the use of transition metal chalcogenide based heterogeneous co-catalysts, and solution based water redox catalysts immobilized in polyoxometalate ensembles for water splitting, there are limited studies on their application in tandem water splitting cells. Sections below discuss the fundamentals and rationale behind each of these classes of materials.

### **1.3.2 Polyoxometalates (POMs)**

Polyoxometalates (POMs) are transition metal oxoanion cluster frameworks linked by common oxygen atoms. They are generally composed of transition metal atoms (M) in their highest oxidation states, with heteroatoms (X = Si, P) that increase hydrolytic stability. These basic structures (Figure 1.9)<sup>50</sup> can be modified by addition or removal of atoms for formation of defect sites (lacunary structure).

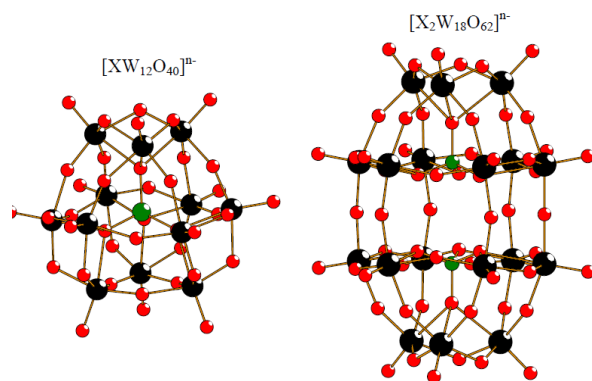


Figure 1.9 Keggin and Dawson heteropolytungstates. Black: tungsten, Red: oxygen, Green: heteroatom (Obtained with permission from Ref. 50).

Previous research has been focused on the catalytic applications of POMs.<sup>51-55</sup>

POMs can be efficient water splitting catalysts due to (1) facile reversible multi-electron transport kinetics within the POM architecture, (2) stabilization of active transition metal catalysts in their highest oxidation states within the POM architecture, which is an essential requirement for efficient water oxidation and reduction,<sup>55-59</sup> (3) coordination of multi-metal cores, which effectively increases the number of active sites, and (4) absence of organic moieties in POMs employed, increasing their stability.

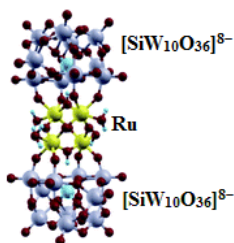


Figure 1.10 Structure of Ru<sub>4</sub>POM (Obtained with permission from Ref. 60).

Figure 1.10 denotes the structure of Ru<sub>4</sub>POM,<sup>60</sup> with a PS(II) mimic Ru core. Ru,<sup>57, 61-63</sup> Co,<sup>64-67</sup> and Ni<sup>68</sup> based POMs have been employed for photochemical and electrocatalytic water oxidation, providing proof of concept to the prediction that they

could be effective electron and hole utilization agents for both water oxidation and water reduction catalysis. However, such systems are not practically feasible in the long run for solar water splitting due to oxidative quenching of the photosensitizer over time and necessity for gas separation due as a result of the non-localized process.

The use of POM based water redox catalysts as functional catalysts in PEC and tandem PEC water splitting has rarely been pursued, and immobilization of POM catalysts on semiconductor based photoanodes and photocathodes for study of PEC properties itself is extremely rare to the best of our knowledge. Hence, this dissertation aims to study the photoelectrochemistry tandem and stand-alone of photoanodes and photocathodes in conjunction with homogenous and photoelectrode immobilized transition metal substituted POMs for solar water splitting. Particular focus will be put upon earth abundant first row transition metal substituted POMs based on  $\text{Ni}^{2+}$  and  $\text{Co}^{2+}$  due to stability, higher oxidation states, and redox properties of these metals<sup>2</sup> for oxygen evolution similar to Ir and Ru based noble metal catalysts.

### **1.3.3 Metal chalcogenide based HER and OER catalyst**

In the recent years, there has been an increase in research on transition metal selenide,<sup>69-72</sup> sulfide,<sup>73</sup> and phosphide<sup>72,74-77</sup> based catalysts.<sup>78</sup> The effects on chalcogenide heteroatoms on enhancing hydrogen adsorption/desorption kinetics<sup>78-79</sup> has been reported in previous literature through theoretical calculations and DFT studies<sup>78-79</sup>. Hence, they can be seen as viable alternatives to Pt for HER catalysis. Moreover, selenides, sulfides and Phosphides can act as bases and trap protons<sup>78</sup>. Study of this part will focus more on the use of selenide based co-catalysts for HER because the bond strength can be considered as a factor enhancing hydrogen desorption from catalytic

sites<sup>78</sup>, and the Se-H bond (276 kJ/mol) has the least strength compared to P-H (322 kJ/mol) and S-H (363 kJ/mol).<sup>78</sup> Initial studies on Fe, Co,<sup>70</sup> and Ni<sup>69, 72</sup> selenide based materials<sup>73</sup> have indicated efficient catalytic performance for OER. The addition of electronegative Se<sup>2-</sup> ligands in the vicinity of catalytically active metal sites could result in accelerated delivery of dioxygen molecules due to 3d-2p repulsions and negative charge localized on Se sites.<sup>71-72, 78</sup>

A majority of metal phosphides<sup>74</sup> have properties comparable to metals and ceramics. They possess excellent heat and electrical conductivity, in addition to being thermally and chemically stable. Transition metal phosphides have been reported for electrocatalytic water oxidation<sup>72, 75</sup> and can play important roles as bifunctional catalysts.<sup>80</sup> They can be oxidized to higher valences and transformed into metal oxides/hydroxides in the OER environment. A few studies in literature have attributed the high oxidation ability of transition metal phosphides to the formation of a core-shell structure (oxide@metal phosphide).<sup>80-81</sup>

The use of metal selenides and phosphides as co-catalysts for PEC water splitting have been limited as of current research. Considering these factors, this dissertation presents data on metal phosphide based photoanodes for solar water oxidation.

#### **1.4 Overall Research Scope and Methodology**

The overall research is divided into three parts. The first part of the study will focus upon the individual PEC studies on photoanodes and photocathodes in conjunction with Co an Ni polyoxometalate based molecular catalysts in solution (Chapters II and III).

The second part of this project is the study of heterogeneous transition metal chalcogenide based co-catalysts for water splitting. The best performing systems for HER and OER will be described in Chapters IV and V respectively.

Best suitable photoanode/photocathode combinations and tandem photocathode combinations with a-Si triple junction photovoltaic based photoanodes have been tested towards multiple absorber water splitting in Chapter VI.

#### **1.4.1 Preparation of Photoelectrode Films**

##### **1.4.1.1 Electrodeposition**

Electrodeposition is an effective strategy for the preparation of photocatalysts and heterogeneous electrocatalyst precursors by potential or current controlled electrochemical techniques. Stable thin films can be grown by optimization of a variety of parameters such as electrolyte composition, pH, potential, and current ranges.<sup>82</sup>

In this dissertation, under-potential co-deposition technique is used for the deposition of metal chalcogenide thin films. Under-potential electrodeposition is a phenomenon in which the transition metal of choice is able to deposit at a potential less negative than its normal deposition potential. For example, a number transition metals can co-deposit on Se at a potential less negative than their usual deposition potential, with the mechanism given in equations 1.3 and 1.4, which proceeds through the four electron reduction of H<sub>2</sub>SeO<sub>3</sub> to Se followed by the under-potential reduction of transition metal (M) ions on Se.



The deposition can also occur by a six electron route, wherein  $\text{H}_2\text{SeO}_3$  is reduced to  $\text{H}_2\text{Se}$ , which then reacts with metal ions to form metal selenide.



#### **1.4.1.2 Solution deposition/Spin coating**

Chemical solution deposition (also known as sol-gel technique) refers to a host of procedures that involving the following steps: (1) deposition of monomeric metal organic precursor solution dissolved in a predominantly organic solvent (the sol) on substrate of choice by spin coating, spray deposition or dip coating,<sup>83</sup> (2) solvent evaporation resulting in interactions and cross linking among precursor species to form an aggregated or polymerized network (the gel), and (3) formation of desired phase post thermal annealing as a result of structural rearrangements. In a typical procedure, anatase  $\text{TiO}_2$  thin films may be prepared by spin coating of a titanium (IV) butoxide sol dissolved in a water-ethanol mixture followed by thermal annealing.

#### **1.4.2 Physico-Chemical Characterization Techniques**

FT-IR spectroscopy and mass spectrometry (MS) will be used for the chemical characterization of molecular catalysts. Analysis of peaks in the IR finger print region will be carried out for identification of specific inorganic groups, and MS will be used for identification of POM ion fragments.

Scanning electron microscopy (SEM) will be used for the characterization of photoelectrode thin films and catalysts for their surface morphology and thickness/size distribution. Since morphological design of the photoelectrode-catalyst interface is crucial for facilitating balance between charge separation and recombination/light

absorption losses, SEM is expected to provide important data regarding structure property relationships and their effect on device performance. Energy dispersive X-ray diffraction (EDX) is coupled to SEM for elemental analysis.

UV Vis spectroscopy is a versatile technique for the determination of band gap energies of semiconductor materials.<sup>84</sup> In the most simplified approach, the band gap energy can be determined from wavelength at which a steep raise is initiated in absorbance. This is due to the fact that the measured wavelength of photon is the minimum required for electron excitation across the band gap.

### **1.4.3 Fundamentals of PEC Techniques**

#### **1.4.3.1 Illuminated Open Circuit Potential (OCP)**

Illuminated OCP plots are essential electrochemical techniques used to determine the conductivity type and approximate photovoltage and flat band potential of semiconductors.<sup>85</sup> Typically, experiments are conducted using a high impedance voltmeter or a potentiostat under zero current (open circuit conditions). N-type semiconductors exhibit cathodic OCP shifts upon light illumination due to downward band bending, whereas anodic shifts are observed in p-type semiconductors as a consequence of upward band bending. The difference between the dark and illuminated OCP can be used to estimate photovoltage  $V_{ph}$  (See Figure 1.2). OCP measurements in this dissertation will be primarily used for the determination of conductivity type of the semiconductor photoelectrode.

#### **1.4.3.2 PEC Impedance Spectroscopy**

Electrochemical impedance spectroscopy (EIS)<sup>86</sup> is a technique in which the electrochemical system is perturbed by a small amplitude AC signal of variable



frequencies ( $\omega$ ). It visualizes the electrode-electrolyte interface as an equivalent circuit (the Randles Sevcik circuit) for study of electrode kinetics and double layer architecture.

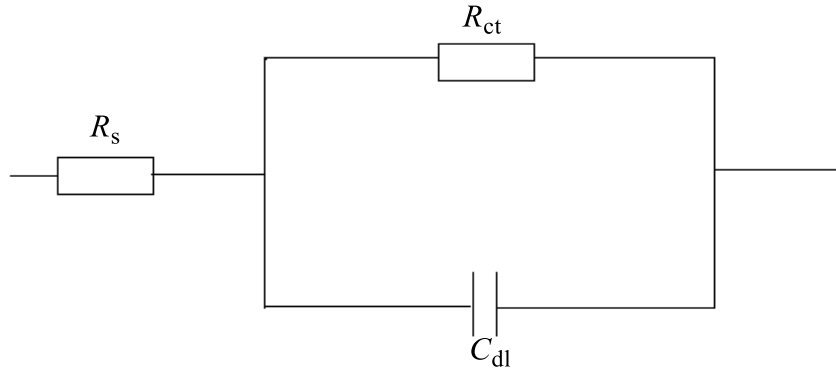


Figure 1.11 EIS equivalent circuit.

A representative equivalent circuit containing the double layer capacitance ( $C_{dl}$ ), solution resistance ( $R_s$ ) and charge transfer resistance ( $R_{ct}$ ) is shown in Figure 1.11, where  $C_{dl}$  denotes the capacitance build-up at the double layer, and  $R_{ct}$  and  $R_s$  are the resistances to interfacial charge transfer and resistance from the electrolyte solution. These parameters can be computed from impedance data, which is usually collected in the form of Nyquist (Figure 1.12) and Bode plots.

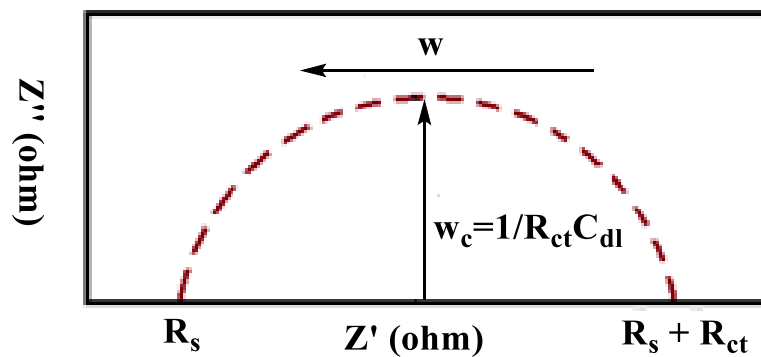


Figure 1.12 Nyquist Plot.

PEC impedance spectroscopy (PEIS) is a procedure in which impedance spectroscopic techniques are employed in the presence of light illumination. It can provide a host of vital information regarding the kinetics of charge carrier transfer, recombination, band pinning, and role of catalysts on the semiconductor-electrolyte interface.

#### **1.4.3.3 Mott Schottky analysis**

Band bending occurs at the semiconductor-electrolyte interface due to the difference in electrochemical potential (or Fermi level) between the semiconductor and the electrolyte. This results in the charge separation, and produces a layer of minority charge carriers on the semiconductor electrode surface, which is known as the space charge layer. The capacitance of the space charge layer ( $C_{sc}$ ) can be used as a vital data point for determination of flat band potential ( $V_{FB}$ ) of the semiconductor, at which band bending and potential drop associated with the space charge layer effectively vanishes. Measurement of  $V_{FB}$  helps in optimization of photoelectrodes for efficient charge carrier separation and photocurrent generation.

Mott Schottky analysis<sup>85</sup> is an EIS based technique which provides data on the relationship between applied potential and space charge capacitance at set frequencies. A representative Mott Schottky plot is provided in Figure 1.13.

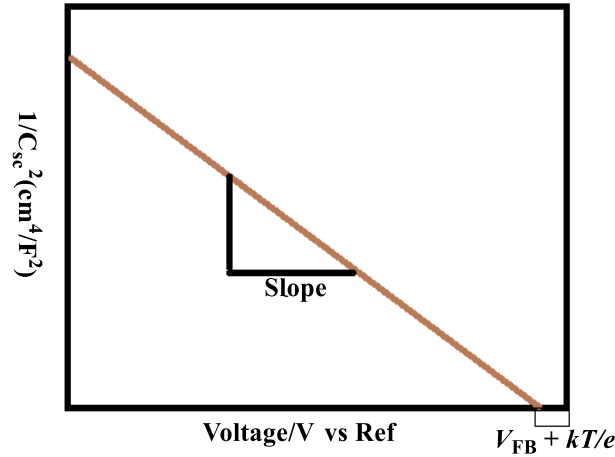


Figure 1.13 Mott Schottky Plot.

The x intercept of the Mott Schottky plot equals  $V_{FB} + kT/e$ ,<sup>87</sup> where  $V_{FB}$  is the flat band potential,  $k$  is Boltzmann constant,  $T$  is the temperature, and  $e$  is the charge of an electron. With known  $V_{FB}$  and applied AC bias, the charge carrier concentration ( $N_D$ ) across the semiconductor (with an area of  $A$ ) electrolyte interface can be computed from slope of the Mott Schottky plot, in accordance with the following formula:<sup>87</sup>

$$N_D = \frac{1.41 \times 10^{32} (\text{cm}^4 \text{F}^{-2} \times \text{V}^{-1})}{\xi_r \times A^2 (\text{cm}^4) \times \text{slope} (\text{F}^{-2} \times \text{V}^{-1})} \quad (1.7)$$

The relative permittivity of the semiconductor  $\xi_r$  is assumed to be 10 in most cases.<sup>87</sup>

#### 1.4.3.4 Three Electrode $j$ - $V$ and Photocurrent Onset Measurements

PEC water splitting makes the use of light driven charge carrier separation in semiconductor photoelectrodes for dissociation of water into hydrogen and oxygen.

Three electrode  $j$ - $V$ <sup>88</sup> and photocurrent onset measurements place focus upon fundamental PEC properties of the semiconductor materials tested for water photoelectrolysis. This technique tests a particular material's ability to produce

photogenerated current ( $j_{ph}$ ) at a given potential, and aid in the measurement of photocurrent onset potential ( $E_{onset}$ ).

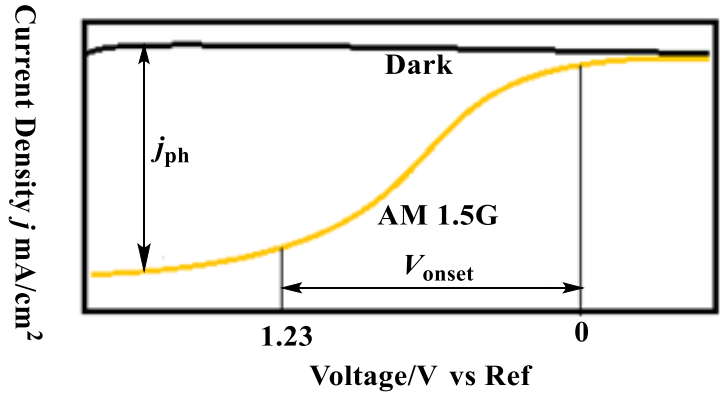


Figure 1.14 Representative photocurrent plot.

Figure 1.14 provides a representative three electrode photocurrent measurement for a semiconductor photoanode. The experiment is typically started at potentials in the range of measured flat band potential ( $V_{FB}$ ) where there is negligible photocurrent as a result of no band bending. As the potential is further swept in the anodic direction, the steep onset of photocurrent is noticed as a result of charge separation at the interface. The potential at which photocurrent begins to appear is referred to as the photocurrent onset potential ( $E_{onset}$ ). Onset voltage ( $V_{onset}$ ) is the difference between the photocurrent onset potential and thermodynamic potential for water oxidation or reduction. Materials providing greater onset voltage are best suitable to be optimized for unbiased water splitting, High values of photocurrent indicate effective charge carrier separation, and are directly related to the efficiency limits of the system. At definite values beyond the reversible potential for the reaction of choice, band bending becomes too large that the photocurrent saturates and remains steady.

### 1.4.3.5 Two Electrode Short Circuit and $j$ - $V$

Two electrode  $j$ - $V$  experiments<sup>88</sup> involve the time-dependant perturbation of DC voltage between the working and counter electrodes under light illumination and in dark conditions. These experiments are critical for the determination of applied bias to photocurrent efficiency (%ABPE) and solar to hydrogen conversion efficiency (%STH). Thus, they shed light on the water splitting capabilities and limits of materials used in a PEC system. Also, two electrode  $j$ - $V$  measurements is one of the primary PEC techniques to study overall water splitting.

If water splitting can be achieved under zero applied bias between the working and counter electrodes (short circuit conditions), the short circuit photocurrent density ( $j_{sc}$ ) or hydrogen evolution rate will be used for the determination of true solar to hydrogen conversion efficiency (%STH), as provided in Eqs. 1.8 and 1.9.<sup>89</sup>

$$\%STH = \left[ \frac{|j_{sc}(\text{mA}/\text{cm}^2)| \times 1.23 \text{ V} \times \eta_F}{P_{\text{total}} \left( \frac{\text{mW}}{\text{cm}^2} \right)} \right]_{\text{AM1.5G}} \times 100 \quad (1.8)$$

where  $\eta_F$  is the Faradaic efficiency of hydrogen evolution and  $P_{\text{total}}$  is the total solar power input.

$$\%STH = \left[ \frac{(\text{mmol H}_2/\text{s}) \times 237,00 \text{ J/mol}}{P_{\text{total}} \left( \frac{\text{mW}}{\text{cm}^2} \right) \times \text{Area} (\text{cm}^2)} \right]_{\text{AM1.5G}} \times 100 \quad (1.9)$$

The applied bias to photocurrent efficiency can be calculated from the formula provided below:<sup>89</sup>

$$\%ABPE = \left[ \frac{|j_{\text{ph}}(\text{mA}/\text{cm}^2)| \times (1.23 - |V_b|)(\text{V}) \times \eta_F}{P_{\text{total}} \left( \frac{\text{mW}}{\text{cm}^2} \right)} \right]_{\text{AM1.5G}} \times 100 \quad (1.10)$$

CHAPTER II – PHOTOELECTROCHEMICAL STUDIES ON EARTH ABUNDANT  
PENTANICKEL POLYOXOMETALATES AS CO-CATALYST FOR SOLAR  
WATER OXIDATION\*

\*This work has been published in *Sustainable Energy and Fuels* (DOI: 10.1039/C7SE00523G)

## 2.1 Introduction

The development of viable systems for harnessing energy from renewable sources has been an important scientific pursuit in recent years.<sup>12, 20</sup> Photoelectrochemical (PEC) water splitting offers a safe, localized, and low temperature approach for production of hydrogen and oxygen from water, and has an enormous potential for facile integration with hydrogen fuel cells in the near future.<sup>14, 20</sup>

A wide spectrum of research has been carried out in the development of semiconductor based photoelectrodes for PEC water splitting, as well documented in the literature.<sup>12, 20, 23, 26, 29, 90</sup> However, the high energy barrier required for water oxidation (1.23 V vs SHE under standard conditions<sup>29</sup>), in addition to losses from ineffective light absorption and separation of photogenerated electrons and holes pose severe limitations on the ability of single absorber based solar water splitting systems under unbiased or low biased conditions.<sup>34, 90</sup> The prohibitive cost of these noble metal based catalysts necessitates the need for the development of alternate earth abundant non-noble metal based catalysts for efficient solar to hydrogen conversion by water splitting.<sup>2, 34, 91</sup>

Catalysts developed for PEC water oxidation processes must be capable of effectively capturing photogenerated holes and facilitating low energy pathways for oxidation of water, so as to increase observed photocurrent while reducing the onset

potential.<sup>2, 34-35, 91</sup> In the last few years, there has been considerable research progress on transition metal based solution-phase<sup>51, 92-94</sup> and solid-state<sup>2, 14, 34, 91, 93</sup> water oxidation catalysts, most of which have been used in photocatalytic<sup>34, 54, 57, 59, 62-63, 65, 67, 95-96</sup> or electrocatalytic<sup>2, 92, 97-98</sup> water splitting devices. However, electrocatalytic water splitting still demands the application of significant external bias, and the use of photocatalytic methods for large scale device applications come with engineering constraints for O<sub>2</sub>/H<sub>2</sub> gas separation. PEC water splitting with the above-mentioned transition metal based catalysts could provide an efficient, localized system to split water and produce high purity O<sub>2</sub>/H<sub>2</sub> under unbiased or low applied bias conditions.

Research in this chapter focuses upon the catalytic applications of transition metal substituted polyoxometalates (POMs).<sup>51-55</sup> This is due to their ability for facile reversible multi-electron transport kinetics within the POM architecture. Moreover, POM anions are capable of stabilizing active catalytic sites in higher oxidation states, which is an essential requirement for efficient water oxidation and reduction.<sup>55-59</sup> POMs are also able to coordinate multi-metal cores, which effectively increases the number of active sites for water oxidation and reduction catalysis. Previously, Ru,<sup>57, 62-63, 96, 98</sup> Co,<sup>64-67, 95, 97, 99</sup> and Ni<sup>68</sup> based POMs have been employed for photochemical<sup>54, 57, 59, 62-63, 65, 68</sup> and electrocatalytic<sup>97-98</sup> water oxidation. Recently, Hill et al. reported the use of dye sensitized TiO<sub>2</sub> photoanodes treated with Ru based POMs for water oxidation, focusing on the effect of sensitizer design on performance.<sup>100</sup>

The use of water oxidation catalysts in solution offers a variety of advantages for PEC applications, including fast reaction kinetics, low electric resistance, and facile photoelectrode fabrication. In this study, we investigate the use of

$\text{K}_{10}\text{H}_2[\text{Ni}_5(\text{OH})_6(\text{OH}_2)_3(\text{Si}_2\text{W}_{18}\text{O}_{66})]\cdot 34\text{H}_2\text{O}$  ( $\text{Ni}_5\text{-POM}$ ) as an earth abundant water oxidation catalyst in solution for PEC water splitting using spin-coated  $\text{TiO}_2$  photoanodes.  $\text{Ni}_5\text{-POM}$  has been reported to be a stable and active homogenous water oxidation catalyst.<sup>68</sup> While the exact mechanism of water oxidation on POMs is still being studied, the complex environment could play a role in increasing water oxidation activity. The penta-nickel unit has multiple bridging oxo groups that act as acceptor bases for the water oxidation mechanism, and also stabilize the metal center in higher oxidation states. This cluster of oxo-bridged multiple d-electron resembles the structure of  $\text{Mn}_4\text{CaO}_4$ ,<sup>101</sup> the active oxygen evolution center in Photosystem II.<sup>102</sup> As it is carbon free, the complex is oxidatively stable within the applied operating potential range.<sup>68</sup> Additionally,  $\text{Ni}_5\text{-POM}$  is earth abundant, and has shown to be more active toward water oxidation than other Ni based polyoxometalates.<sup>103</sup> In this study, we report for the first time  $\text{Ni}_5\text{-POM}$  can be a suitable co-catalyst in PEC water oxidation with  $\text{TiO}_2$  photoanodes.

## **2.2 Materials and Methods**

### **2.2.1 Chemicals**

Unless otherwise stated, all chemicals were purchased from Aldrich and used as received. Titanium (IV) butoxide (97%) and hydrogen peroxide (50 wt% in  $\text{H}_2\text{O}$ ) were used in the preparation process for  $\text{TiO}_2$  films. Sodium metasilicate (> 99%), nickel chloride hexahydrate (> 99%), sodium tungstate dihydrate (> 99%), sodium carbonate (> 99%), and potassium chloride (Fischer, ACS grade) were the chief salts used for preparation of  $\text{Ni}_5\text{-POM}$  catalyst. De-ionized water (Millipore Advantage 5) was used



when performing all experiments, and all instruments were calibrated in accordance with accepted standards.

### **2.2.2 Preparation of FTO/TiO<sub>2</sub> and Ni<sub>5</sub>-POM**

FTO/TiO<sub>2</sub> photoanode and Ni<sub>5</sub>-POM catalyst were prepared according to the literature<sup>104</sup>. TiO<sub>2</sub> thin films were prepared by spin coating technique from a precursor solution consisting of titanium (IV) butoxide and H<sub>2</sub>O<sub>2</sub> in a 1:3 volume ratio, and water-ethanol mixture was the solvent. Typically, 100 μL of 97% titanium (IV) butoxide and 300 μL of 50% H<sub>2</sub>O<sub>2</sub> were added to 5.00 mL of solvent containing equal volumes of water and ethanol, followed by ultrasonic dispersion for 2 h. Cleaning of FTO substrates was done by sonication in deionized water, methanol, acetone, isopropanol, and deionized water, each for 15 min, respectively. Layers of dispersed precursor solution were spin coated onto a 1 cm<sup>2</sup> active area of the dry FTO substrate by spinning 50 μL of the freshly prepared solution at 2000 rpm for three times. This was followed by sintering at 773 K for 2 h and gradual cooling to produce the TiO<sub>2</sub> photoelectrode for study. Synthesis of Ni<sub>5</sub>-POM catalyst was done in accordance with procedures reported previously.<sup>68</sup> 27.5 mmol of Na<sub>2</sub>WO<sub>4</sub> and 2.6 mmol of Na<sub>2</sub>SiO<sub>3</sub> were dissolved in 15 mL of water (at 80°C) to obtain a clear solution. 9.5 mL of 6.0 M HCl was added slowly over a period of 30 min under vigorous stirring, and the solution was filtered over a frit to remove the unreacted silica. In a separate beaker, 2.5 mL of sodium carbonate was dissolved in 7.5 mL of deionized water. This sodium carbonate solution was then added slowly to the first solution under gentle stirring. A white precipitate formed after 1 h, which was isolated by gravity filtration. The obtained white precipitate was stirred in 50 mL of 4.0 M NaCl, filtered, and washed with diethyl ether and ethanol successively and

dried to produce  $\text{Na}_{10}[\alpha\text{-SiW}_9\text{O}_{34}]$  precursor. This was followed by the substitution of Ni ions.  $\text{Na}_{10}[\alpha\text{-SiW}_9\text{O}_{34}]$  (0.54 mmol) was added to 15 mL of deionized water, forming a turbid white suspension. Drop-wise addition of 1.0 M HCl adjusted the pH to 6.8, causing the suspension to dissolve into a solution. This was followed by the addition of  $\text{NiCl}_2 \cdot 6\text{H}_2\text{O}$  (1.35 mmol) under stirring. The solution was refluxed for two hours, cooled to room temperature, filtered, and then 20 mL of saturated KCl was added. The resulting solution was placed in an ice bath with stirring for an hour and the pale green precipitate that slowly formed over this time was collected via filtration. The crude product was recrystallized twice from hot water. Slow evaporation produced green,  $\text{Ni}_5\text{-POM}$  crystals.

The synthesized  $\text{Ni}_5\text{-POM}$  was first characterized by FT-IR spectroscopy. A majority of principle peaks in FT-IR spectrum, which was taken with a Nicolet Nexus 470 FT-IR spectrometer, matched closely with those shown in the previous report<sup>68</sup> (see Figure 2.1). Electrospray mass spectrometric analysis, which was carried out with a Thermo-Fischer LXQ ESI-ion trap mass spectrometer (Waltham, MA, USA), was used to further confirm the composition of the synthesized  $\text{Ni}_5\text{-POM}$ . As revealed in Figure 2.2 and Table 2.1, a number of observed mass/charge ( $m/z$ ) peaks, such as 194.75 (Figure 2.2a), 623.17 (Figure 2.2b), 718.00 (Figure 2.2c), 825.46 (Figure 2.2d), 1286.08 (Figure 2.2e), and 1664.67 (Figure 2.2f), are consistent with the POM related fragments,  $[\text{K}(\text{H}_2\text{O})_4\text{W}_{18}\text{O}_{66}]^{23-}$ ,  $[\text{K}_3\text{HX}]^{8-}$ ,  $[\text{K}_4\text{HX}]^{7-}$ ,  $[\text{K}_2\text{H}_4\text{X}]^6$ ,  $[\text{K}_7\text{HX}]^{4-}$ , and  $[\text{K}_3\text{H}_6\text{X}]^{3-}$ , respectively, where  $\text{X} = [\text{Ni}_5(\text{OH})_6(\text{OH}_2)_3(\text{Si}_2\text{W}_{18}\text{O}_{66})]$

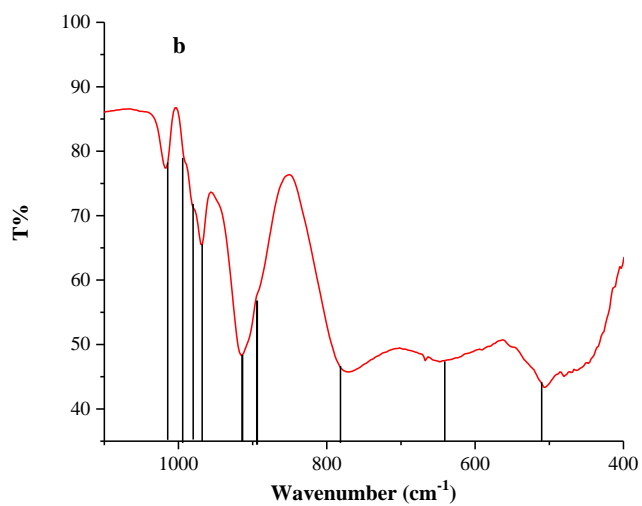
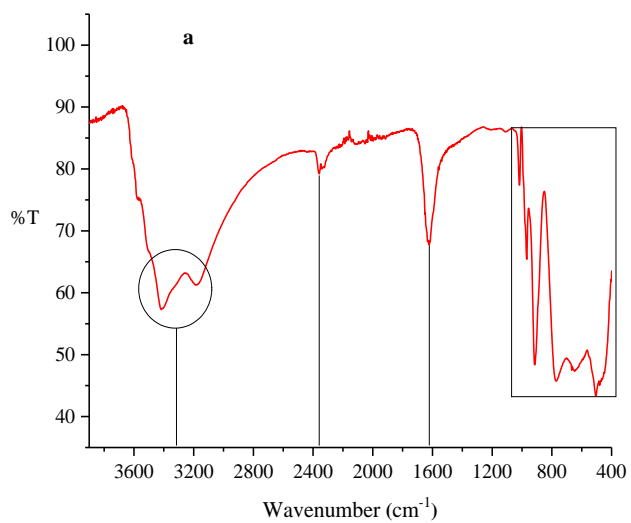


Figure 2.1 FT-IR spectra of Ni<sub>5</sub>-POM. (a) Entire spectral region from 400 to 4000 cm<sup>-1</sup> and (b) scaled in the fingerprint region of 400 to 1100 cm<sup>-1</sup>.

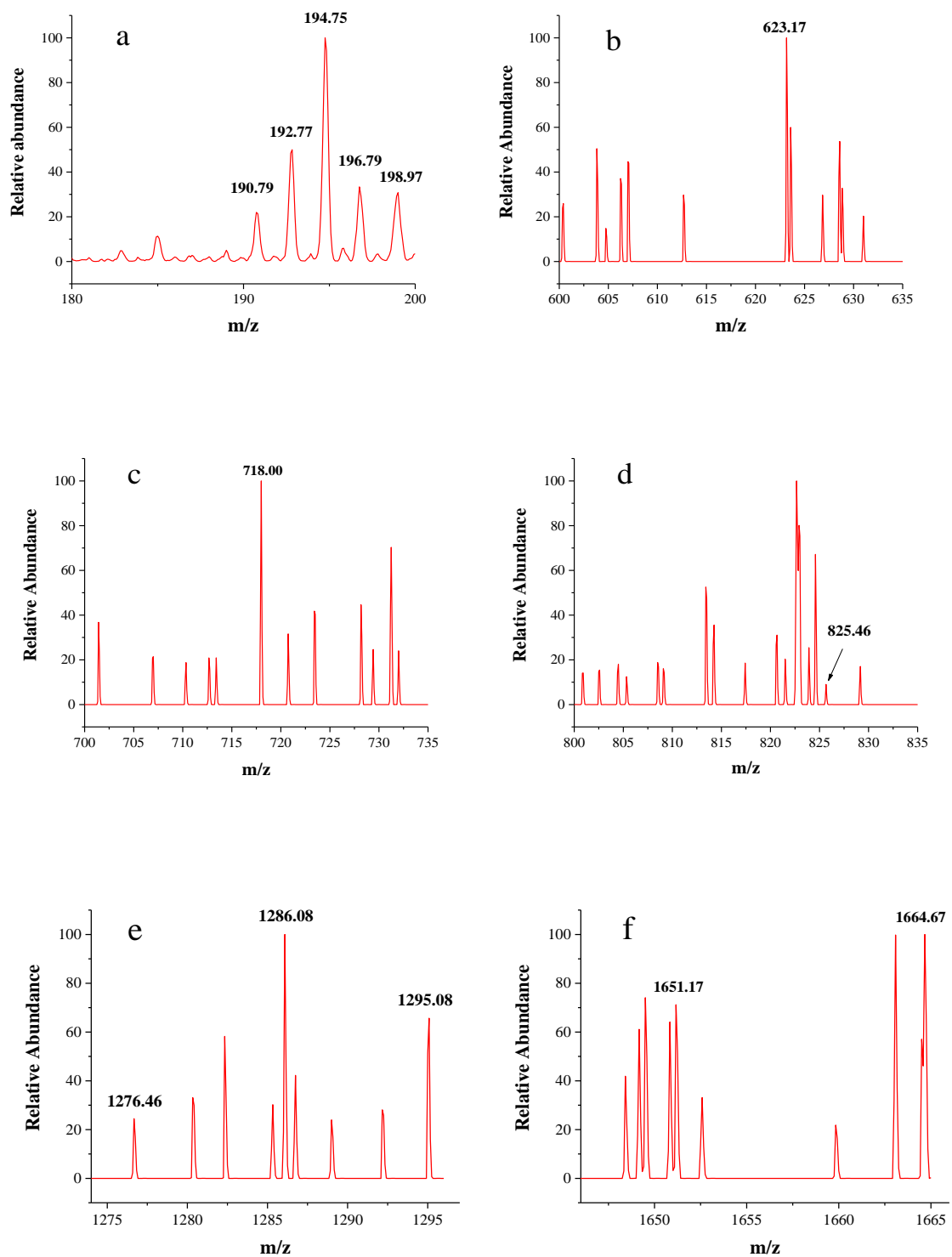


Figure 2.2 Mass spectra of Ni<sub>5</sub>-POM in different m/z regions.

Table 2.1 Peak assignments for mass spectra of Ni<sub>5</sub>-POM shown in Figure 2.2

Observed m/z	Predicted m/z	Formula
190.79	190.58	[H(H <sub>2</sub> O)W <sub>18</sub> O <sub>66</sub> ] <sup>23-</sup>
192.77	192.92	[H(H <sub>2</sub> O) <sub>4</sub> W <sub>18</sub> O <sub>66</sub> ] <sup>23-</sup>
194.75	194.63	[K(H <sub>2</sub> O) <sub>4</sub> W <sub>18</sub> O <sub>66</sub> ] <sup>23-</sup>
196.79	196.47	[K(H <sub>2</sub> O) <sub>6</sub> W <sub>18</sub> O <sub>66</sub> ] <sup>23-</sup>
198.97	198.66	[H <sub>2</sub> W <sub>18</sub> O <sub>66</sub> ] <sup>22-</sup>
623.17	623.38	[K <sub>3</sub> HX] <sup>8-</sup>
718.00	718.24	[K <sub>4</sub> HX] <sup>7-</sup>
825.46	825.45	[K <sub>2</sub> H <sub>4</sub> X] <sup>6-</sup>
1276.46	1276.67	[K <sub>6</sub> H <sub>2</sub> X] <sup>4-</sup>
1286.08	1286.17	[K <sub>7</sub> HX] <sup>4-</sup>
1295.08	1295.47	[K <sub>8</sub> X] <sup>4-</sup>
1651.17	1651.83	[K <sub>2</sub> H <sub>7</sub> X] <sup>3-</sup>
1664.67	1664.57	[K <sub>3</sub> H <sub>6</sub> X] <sup>3-</sup>
X = [Ni <sub>5</sub> (OH) <sub>6</sub> (OH <sub>2</sub> ) <sub>3</sub> (Si <sub>2</sub> W <sub>18</sub> O <sub>66</sub> )]		

### 2.2.3 Physico-Chemical Characterization of FTO/TiO<sub>2</sub> Photoanode

A Zeiss Sigma VP FEG scanning electron microscope (SEM) was used for the SEM images of TiO<sub>2</sub> photoelectrodes on FTO substrate. The UV-vis spectrum of TiO<sub>2</sub> photoelectrodes was recorded using an Evolution 300 Thermo-Scientific spectrophotometer.

### 2.2.4 Photoelectrochemical Studies

PEC measurements were carried out with a three-electrode electrochemical setup using a 50 mL quartz beaker as the cell, an Ag/AgCl (3.0 M KCl) as the reference electrode, a Pt wire as the counter electrodes, and the FTO/TiO<sub>2</sub> (1 cm<sup>2</sup>) as the working electrode, respectively. The 1 cm<sup>2</sup> exposed area of the working electrode was creating by

masking the remaining regions with non-conducting parafilm. Electrochemical impedance spectroscopic (EIS) measurements were carried out at open circuit DC potential with a 5 mV super-imposed AC signal. For unbiased potential studies, a two-electrode setup was used with a Pt wire as the reference/counter electrode. Experiments were performed in a 0.050 M pH 9.0 borate buffer solution at a scan rate of 0.020 V/s, with and without the presence of 20  $\mu\text{M}$  Ni<sub>5</sub>-POM catalyst. All electrochemical studies were performed using a CH instruments model 660 A electrochemical workstation. A 150 W Xe lamp solar simulator (ABET technologies) with an AM 1.5 G filter providing a light intensity of 1000 W/m<sup>2</sup> (1 sun) was used as the visible light source for PEC studies. Oxygen detection was carried out using dissolved oxygen measurements with an oxygen sensor (Hanna Instruments, Model HI9164).

## **2.3 Results and Discussion**

### **2.3.1 Physico-Chemical Characterization**

Surface morphology of TiO<sub>2</sub> film coated FTO is shown in Figure 2.3 at different magnifications, where even distribution of TiO<sub>2</sub> particles in the form of micro-sized flakes ( $\sim 20 \times 30 \mu\text{m}$ ) is evident (Figure 2.3a). The thickness of the cracked film can be estimated on the basis of SEM images at higher resolutions (Figures 2.3b and c), which show an approximate value of 2-3  $\mu\text{m}$ . These cracks are most likely formed during annealing process due to probably thermal expansion coefficients mismatch of the coating and FTO substrate, as observed previously for TiO<sub>2</sub> on ITO<sup>105</sup> and steel substrates.<sup>106</sup> This as-prepared TiO<sub>2</sub>/FTO photoanode could provide a large and uniform surface area for light absorption and charge generation, effective interaction between TiO<sub>2</sub> layer and solution-phase catalyst, as well as reducing the amount of recombination

hotspots that result in efficiency losses. The energy dispersive X-ray (EDX) spectrum of TiO<sub>2</sub> micro-flakes on FTO substrate shown in Figure 2.4 displays two major peaks from Ti and O, as well a few minor peaks from Sn. These data confirm the formation of TiO<sub>2</sub> on FTO (i.e., F:SnO<sub>2</sub>) substrate. Note also that no EDX peaks associated with impurities or dopants are observed. Figure. 2.5 shows the UV-vis spectra of TiO<sub>2</sub>/FTO (Figure 2.5 a), FTO substrate (Figure 2.5b), and TiO<sub>2</sub> (Figure 2.5c), respectively.

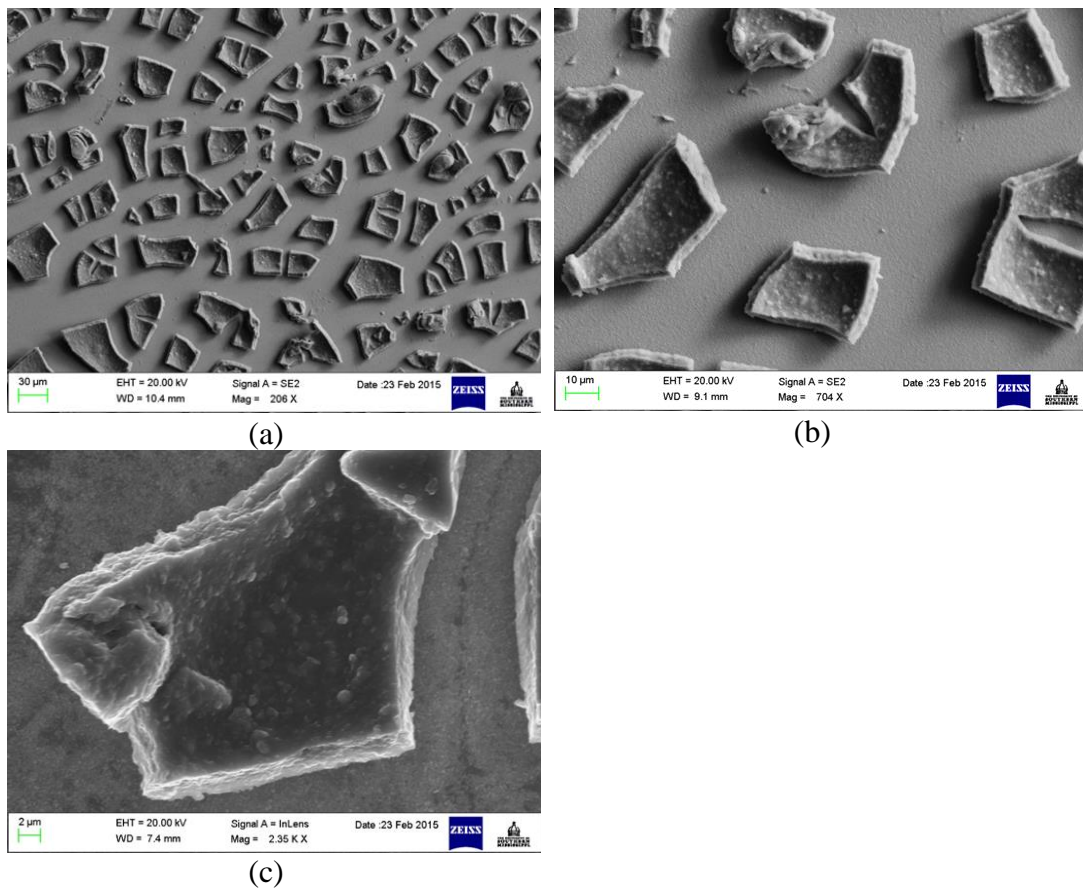


Figure 2.3 SEM images of spin coated TiO<sub>2</sub> films on FTO substrate at (a) 206 X, (b) 704 X, and (c) 2.35 kX magnification.

An onset wavelength ( $\lambda$ ) of  $\sim 385$  nm can be estimated from Figure 2.5 for TiO<sub>2</sub> absorption, which corresponds to a band gap energy ( $E$ ) of 3.22 eV as  $E$  (in eV) =  $1240/\lambda$  (in nm).<sup>20</sup> Additionally, TiO<sub>2</sub> shows a maximum absorption at  $\sim 308$  nm as seen

from previous reports.<sup>4, 107</sup> In other words, the synthesized TiO<sub>2</sub> nanoparticles are anatase type TiO<sub>2</sub>.<sup>104, 108</sup>

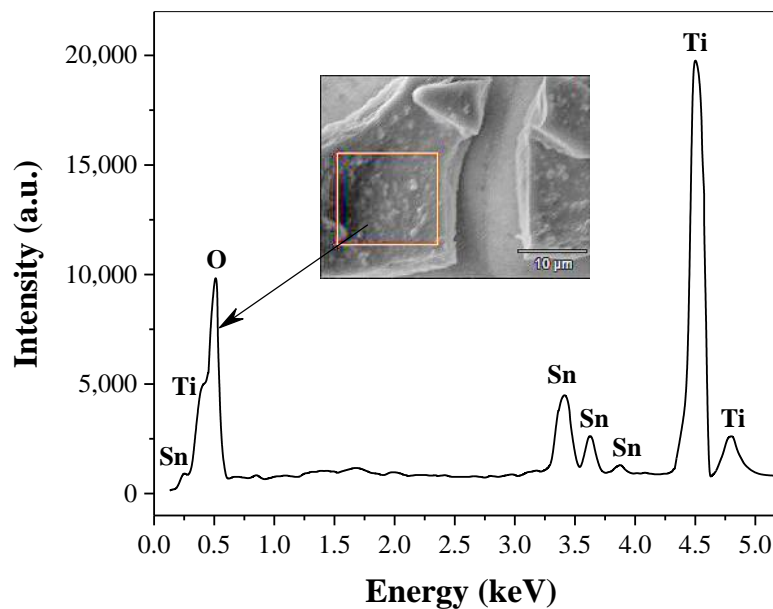


Figure 2.4 Energy dispersive X-ray (EDX) spectrum of spin coated TiO<sub>2</sub> films on FTO substrate. The analysis was spotted on the TiO<sub>2</sub> microflake shown in the inset.



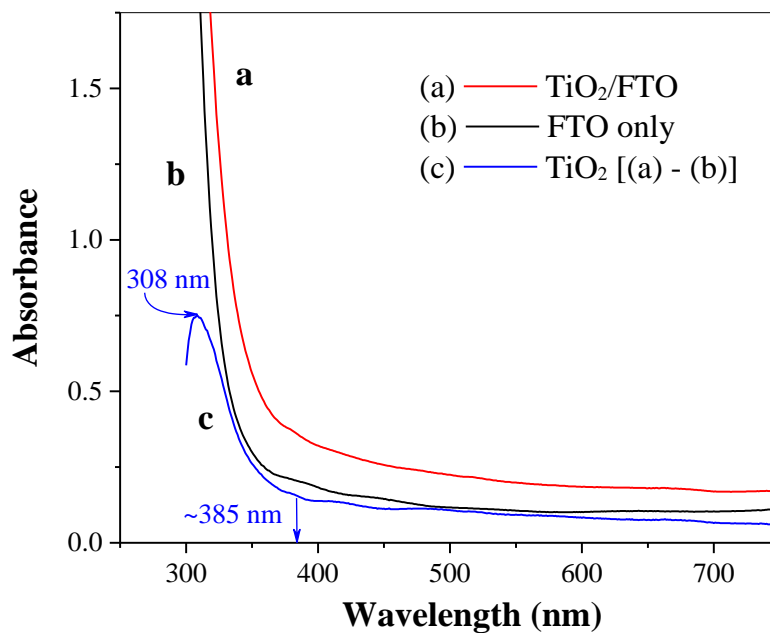


Figure 2.5 UV-vis spectra of (a) spin coated TiO<sub>2</sub> film on FTO substrate, (b) FTO substrate only, and (c) TiO<sub>2</sub> film obtained by subtracting (b) from (a).

### 2.3.2 Three-Electrode Photocurrent Measurements And Electrochemical Impedance Spectroscopy

The study of photoelectrochemical properties is important for understanding of photoelectrode-catalyst interactions and determining the overall effectiveness of the catalyst in facilitating solar water oxidation. Figure 2.6 shows the linear sweep voltammograms obtained from TiO<sub>2</sub>/FTO photoanodes in the absence (Figure 2.6a) and presence (Figure 2.6 b) of water oxidation catalyst Ni<sub>5</sub>-POM (20 μM in 0.050 M pH 9.0 borate buffer) under dark conditions and the photoanodes in the absence (Figure 2.6 c) and presence (Figure 2.6) of Ni<sub>5</sub>-POM catalyst (20 μM in 0.05 M pH 9.0 borate buffer) under simulated solar radiation, respectively. Clearly, under dark, negligible current is seen at TiO<sub>2</sub>/FTO electrode in the absence (Figure 2.6a) or presence (Figure 2.6b) of Ni<sub>5</sub>-

POM catalyst within the sweep potential window of -0.25 to +0.70 V vs Ag/AgCl. However, the overall current density in the presence of Ni<sub>5</sub>-POM is marginally higher than that in its absence due to its electrocatalytic activity. This is better evidenced by dark current measurements on control FTO electrodes (Figure 2.7), that indicate a significant increase in water oxidation current density and negative shift in onset potential in the presence of Ni<sub>5</sub>-POM catalyst in solution. Under light irradiation, a photocurrent density of -0.087 mA/cm<sup>2</sup> at 0.70 V vs Ag/AgCl at TiO<sub>2</sub>/FTO electrode is observed even in the absence of Ni<sub>5</sub>-POM in solution (Figure 2.6c). This photocurrent density is increased by 2.3 times (i.e., -0.20 mA/cm<sup>2</sup>) upon the addition of 20 μM Ni<sub>5</sub>-POM to the borate buffer electrolyte (Figure 2.6d). The use of Ni<sub>5</sub>-POM catalyst also significantly shifts the onset potential of water oxidation to a much negative potential value than -0.20 V vs Ag/AgCl (Figure 2.6d vs 2.6c). These above findings suggest that under the present experimental conditions, light irradiation is a prerequisite of water oxidation and Ni<sub>5</sub>-POM can effectively facilitate the oxidation process. The increase in observed photocurrent in the presence of the catalyst points its effectiveness in enhancing electron-hole separation by capturing holes from the conduction band of TiO<sub>2</sub> for its mechanistic pathway to oxidize water. Moreover, the negative shift in onset potential with added Ni<sub>5</sub>-POM points at its catalytic activity for water oxidation through probably facile charge transfer kinetics and hole utilization. The obtained photocurrent, i.e., -0.20 mA/cm<sup>2</sup> at 0.70 V vs Ag/AgCl, is significantly larger than that produced from Ag nanoparticle,<sup>109</sup> Co<sub>3</sub>O<sub>4</sub>,<sup>110</sup> CdS<sup>111</sup>, or glycerol<sup>112</sup> modified TiO<sub>2</sub> photoelectrode under similar experimental conditions (as shown in Table 2.2).

Table 2.2 Comparison of photocurrents obtained at different TiO<sub>2</sub> based photoelectrodes for water splitting under various experimental conditions

Photoelectrode	Photocurrent and Conditions	Reference
AgNP decorated TiO <sub>2</sub>	~0.016 mA/cm <sup>2</sup> at 0.70 V vs Ag/AgCl under UV, and ~0.1 mA/cm <sup>2</sup> under visible light, using 0.1 M Na <sub>2</sub> SO <sub>4</sub> electrolyte	<sup>109</sup>
Co <sub>3</sub> O <sub>4</sub> modified TiO <sub>2</sub>	0.045 mA/cm <sup>2</sup> at 0.8 V vs Ag/AgCl under AM 1.5G light of 100 mW/cm <sup>2</sup> , using 0.1 M Na <sub>2</sub> S electrolyte	<sup>110</sup>
Direct Z-scheme TiO <sub>2</sub> /CdS hierarchical photocatalyst	~0.13 mA/cm <sup>2</sup> at 0.60 V vs Ag/AgCl, 0.5 M Na <sub>2</sub> SO <sub>4</sub> electrolyte, 3 W UV LED light source	<sup>111</sup>
TiO <sub>2</sub> nanotubes with glycerol as hole scavenger	~90 μA/cm <sup>2</sup> at 0.70 V vs SCE, 0.1 M KOH electrolyte, 300 W Xenon lamp with 365 nm filter	<sup>112</sup>
TiO <sub>2</sub> modified with Ru(bpy) <sub>3</sub> <sup>2+</sup> derivative dye with Ru(II) polyoxometalate (POM)	54.8 μA/cm <sup>2</sup> at pH 5.80 (Na <sub>2</sub> SiF <sub>6</sub> /NaHCO <sub>3</sub> electrolyte) and 34.2 μA/cm <sup>2</sup> at pH 7.2 (lutidine/HClO <sub>4</sub> electrolyte), 0 V vs Ag/AgCl, 455 nm LED	<sup>100</sup>
TiO <sub>2</sub> in the presence of solution-phase Ni <sub>5</sub> -POM	0.20 mA/cm <sup>2</sup> at 0.70 V vs Ag/AgCl, 20 μM Ni <sub>5</sub> -POM in 50 mM borate buffer, pH 9.0	This work

The present system also shows a comparable photocurrent as compared to that from a photoelectrode of TiO<sub>2</sub> modified with Ru(bpy)<sub>3</sub><sup>2+</sup> derivative dye attached with Ru(II)-POM water oxidation catalyst at ~0 V vs Ag/AgCl.<sup>100</sup> Clearly, our system does not involve the use of any photosensitizers, noble metal based catalysts or sophisticated electrode processing techniques. Instead, it offers a straightforward path to water oxidation under simulated solar light in near-neutral pH conditions. Given the fact that reports on the use of POMs as co-catalysts are very limited, further research on POM based co-catalysts may offer a viable practical approach to single absorber and tandem solar water splitting.

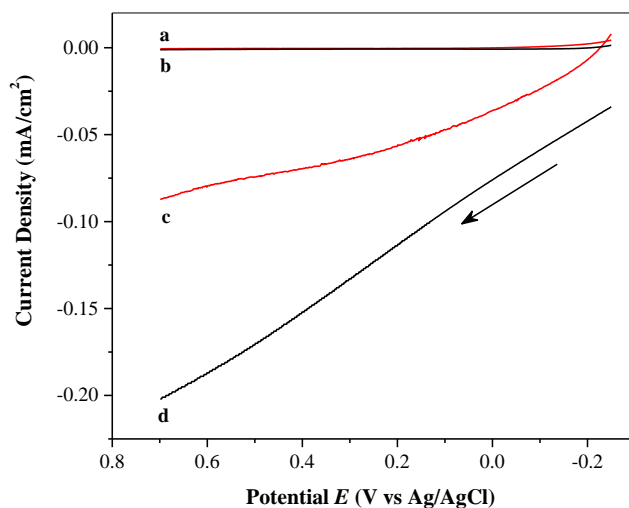


Figure 2.6 Linear sweep voltammograms of TiO<sub>2</sub>/FTO photoanodes in the (a) absence and (b) presence of water oxidation catalyst Ni<sub>5</sub>-POM (20 μM in 0.050 M pH 9.0 borate buffer) under dark conditions and TiO<sub>2</sub>/FTO photoanodes in the (c) absence and (d) presence of water oxidation catalyst Ni<sub>5</sub>-POM (20 μM in 0.050 M pH 9.0 borate buffer) under simulated solar radiation.

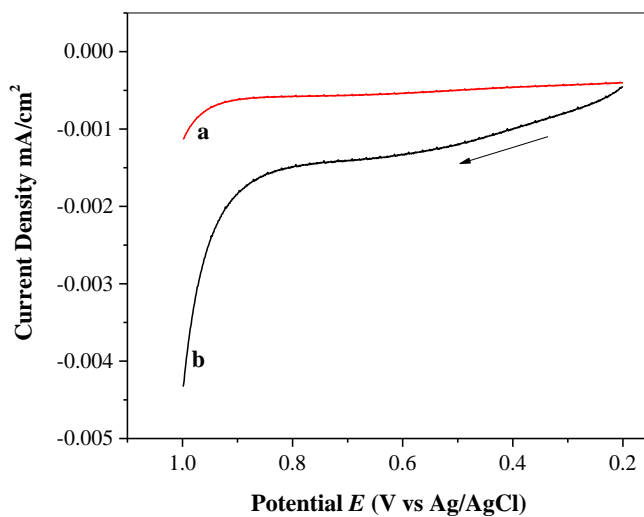


Figure 2.7 Linear sweep voltammograms of FTO anodes in the (a) absence and (b) presence of water oxidation catalyst Ni<sub>5</sub>-POM (20 μM in 0.050 M pH 9.0 borate buffer) under dark.

Electrochemical impedance spectroscopy (EIS) was used to verify the effect of catalyst on increasing electron-hole separation of TiO<sub>2</sub> and on increasing the rate of photoelectrochemical water oxidation. Figure 2.8A and B shows the EIS spectra (Nyquist plots) obtained from TiO<sub>2</sub>/FTO photoanodes under light (Figures 2.8A(a) and 2.8B(a)) and dark (Figure 2.8A(b) and 2.8B(b)) conditions in the absence (Figure 2.8A) and presence (Figure 2.8B) of water oxidation catalyst Ni<sub>5</sub>-POM, respectively. As compared to the data obtained under dark, with light irradiation, a much smaller semi-circle on EIS spectra (Figures 2.8A(a) vs 2.8A(b) as well as Figures 2.8B(a) vs 2.8B(b)) corresponding to a higher double layer capacitance and a lower charge transfer resistance<sup>113-115</sup> is observed, which confirms that the electron and hole are well separated on TiO<sub>2</sub>/FTO photoanode and that the charge transfer process at the electrode surface turns to be much faster in the presence of light illumination. Figure 2.8C compares the Nyquist plots of TiO<sub>2</sub>/FTO photoanodes in the presence (Figure 2.8C(a)) and absence (Figure 2.8C(b)) of water oxidation catalyst Ni<sub>5</sub>-POM under light radiation. In the former case, a considerably lower charge transfer resistance and a higher double layer capacitance are evident. This observation complements data from voltammetric studies (Figure 2.6), indicating increased electron-hole separation and capture of photogenerated holes for water oxidation by the catalyst. Hence, Ni<sub>5</sub>-POM acts as an efficient homogenous co-catalyst for photoelectrochemical water oxidation. On the basis of the above observations and previously reported literature,<sup>34-35, 53, 55</sup> a three-step mechanism associated with the photoelectrochemical water oxidation at TiO<sub>2</sub>/FTO electrode using Ni<sub>5</sub>-POM as solution-phase catalyst is proposed as follows:

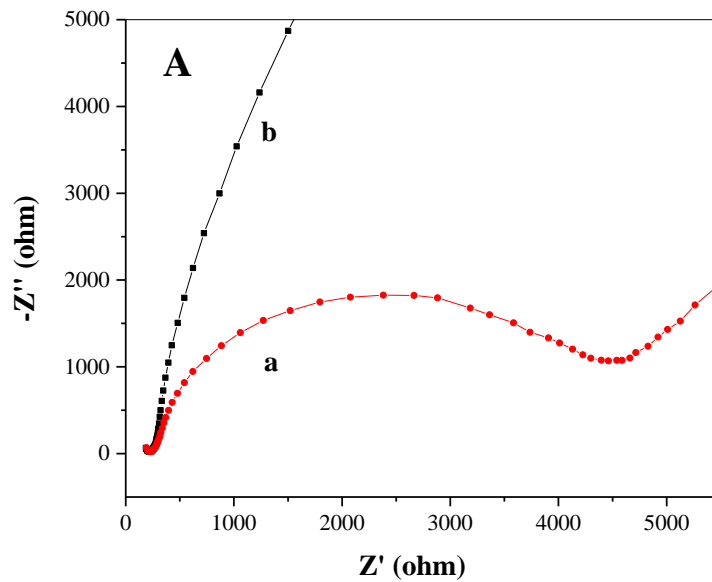
Step 1 – Absorption of light by TiO<sub>2</sub>/FTO photoelectrode and generation of electron-hole pairs:



Step 2 – Hole capture from TiO<sub>2</sub> by Ni<sub>5</sub>-POM water oxidation catalyst and redox levelling



Step 3 – Utilization of photogenerated holes for oxidation of water through catalytic pathways



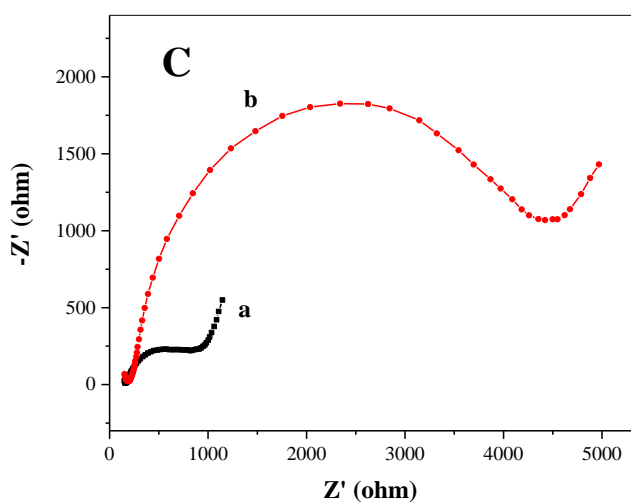
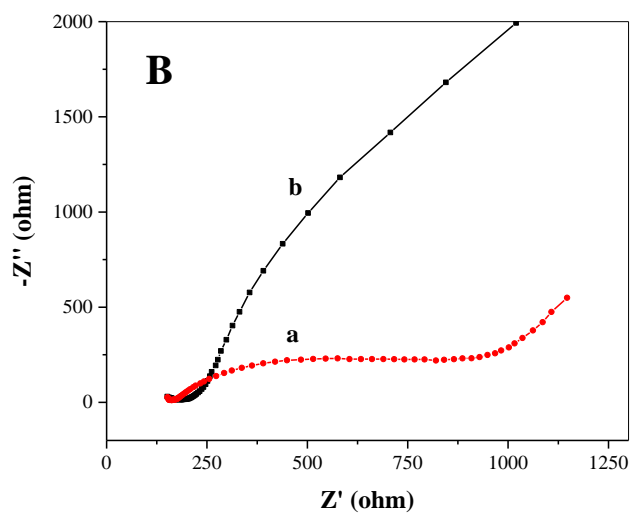


Figure 2.8 Nyquist plots of  $\text{TiO}_2/\text{FTO}$  photoanodes in the (A) absence and (B) presence of water oxidation catalyst  $\text{Ni}_5\text{-POM}$  ( $20 \mu\text{M}$  in  $0.050 \text{ M}$  pH 9.0 borate buffer) under (a) simulated solar irradiation and (b) dark. (C) Nyquist plots of  $\text{TiO}_2/\text{FTO}$  photoanodes in the (a) presence and (b) absence of water oxidation catalyst  $\text{Ni}_5\text{-POM}$  ( $20 \mu\text{M}$  in  $0.050 \text{ M}$  pH 9.0 borate buffer) under simulated solar irradiation.

### 2.3.3 Unbiased two-electrode photocurrent measurements

To study the effect of Ni<sub>5</sub>-POM catalyst on facilitating overall water splitting, photocurrents were measured at zero applied bias under intermittent light with a two-electrode configuration. As shown in Figure 2.9, after stabilization and decay of non-faradaic current, at TiO<sub>2</sub> photoelectrode a very small photocurrent of  $\sim -0.008$  mA/cm<sup>2</sup> is observed in the absence of the catalyst (Figure 2.9a), whereas an approximately 10 times increase in photocurrent (i.e.,  $\sim -0.08$  mA/cm<sup>2</sup>) is obtained in the presence of 20  $\mu$ M Ni<sub>5</sub>-POM water oxidation catalyst in solution (Figure 2.9b). Although this unbiased photocurrent is relatively low, the present finding is significant, given the fact that TiO<sub>2</sub> anatase only has weak solar absorption in the range of UV irradiation (see Figure 2.5c) and that studies of water splitting under unbiased potential using TiO<sub>2</sub> photoelectrode are very limited. Hence, investigation on the possibilities of incorporating POM based water oxidation catalysts for both single absorber and tandem photoelectrochemical water splitting processes could pave way for the development of efficient solar to hydrogen conversion under no applied external bias.



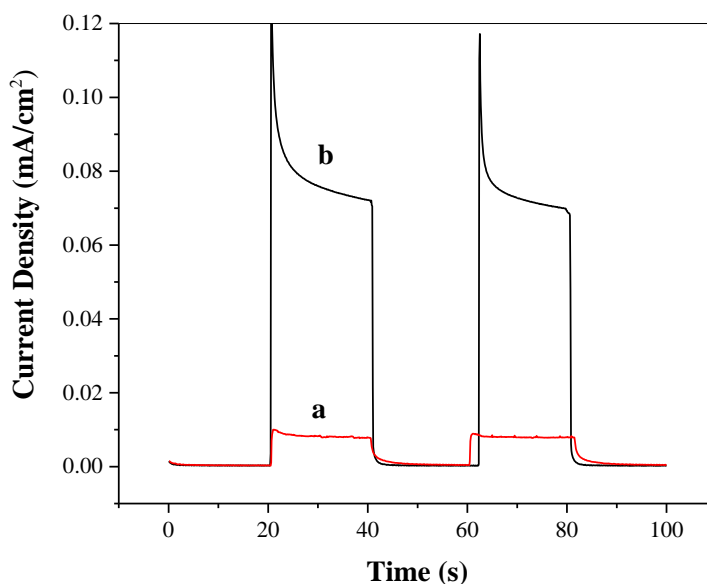


Figure 2.9 Unbiased two-electrode photocurrent plots of  $\text{TiO}_2/\text{FTO}$  photoanodes under intermittent simulated solar light in the (a) absence and (b) presence of water oxidation catalyst  $\text{Ni}_5\text{-POM}$  ( $20 \mu\text{M}$  in  $0.050 \text{ M}$  pH 9.0 borate buffer).

### 2.3.4 Stability studies

The stability of  $\text{TiO}_2/\text{FTO}$  electrodes for photoelectrochemical water oxidation in the presence of  $\text{Ni}_5\text{-POM}$  was evaluated by multiple-potential step and constant potential experiments using a typical three-electrode system. The stability measurements for  $\text{FTO}/\text{TiO}_2$  under constant potential conditions may not actually reflect the stability of the electrode toward water oxidation because the depletion of the electroactive species (i.e.,  $\text{OH}^-$ ) near the surface of the electrode expectedly leads to an inverse time<sup>1/2</sup> function as indicated by the Cottrell equation.<sup>116</sup> In the presence of co-catalyst, water oxidation becomes more effective, resulting in faster depletion of  $\text{OH}^-$  and hence quicker decay of the photocurrent vs time profile. Another issue of such an experiment is that extensive  $\text{O}_2$  gas produced under constant potential accumulated on the electrode surface and inhibited

further electro-oxidation of water. Consequently, the stability study of the photoelectrode was focused on the data generated from the multi-potential step experiment, in which the applied potential was regularly shifted from 0 to 1.10 V vs Ag/AgCl in 3 s intervals for a time period of 4000 s, and responses of photocurrent were recorded. The positive bias of 1.10 V was applied because photocurrent saturation and extensive gas evolution can be expected at this applied potential range. Hence, stability testing at 1.10 V could provide an adequate benchmark in terms of practical performance. Figures 2.10a, b and c are the plots of photocurrent density vs time from a TiO<sub>2</sub>/FTO electrode under multi-potential step excitations in three different time regions, namely 0-200 s, 1800-2000 s, and 3800-4000 s, respectively. Immediately after each potential switch, an initial quick decay in photocurrent due to charging current is displayed. The photocurrent density is then gradually decreased to a relatively stable value within the entire test time window. At the end of this stability experiment, the surface of the photoelectrode exhibited the presence of minor pits owing to extensive gas evolution from the electrode surface. There was no visible appearance of film formation. On the other hand, when a step potential greater than 1.10 V was applied, a washable, light dark film of possibly nickel borate was noticed. As a result, an oxidation potential positive than 1.10 V vs Ag/AgCl is not recommended when testing a system containing POM based solution-phase catalyst. The present TiO<sub>2</sub>/FTO-Ni<sub>5</sub>-POM system has a low onset potential ( $\leq -0.20$  V vs Ag/AgCl, Figure 2.6) and a high operating onset potential ( $\sim 1.10$  V vs Ag/AgCl) for water splitting, which provides a practical photoelectrolyser with a wide range of operating potential window of  $\sim 1.3$  V.

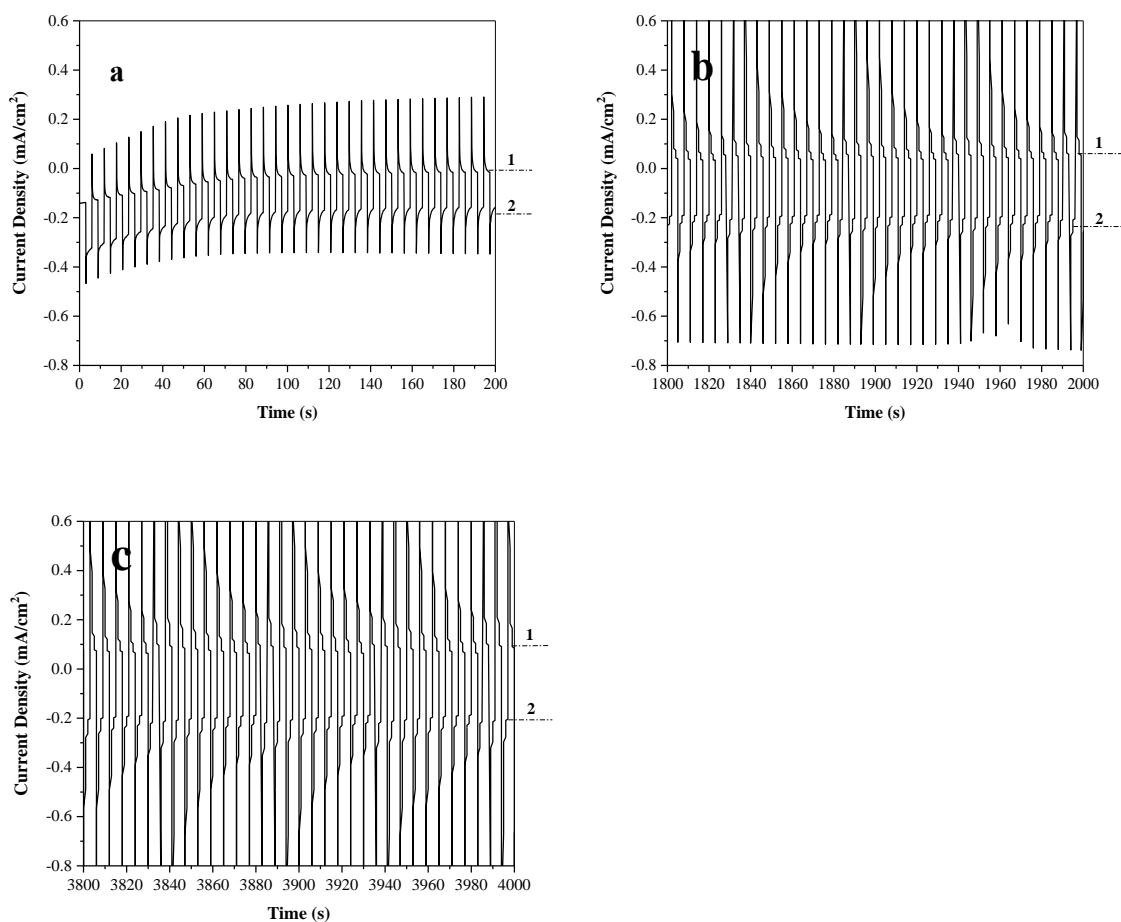


Figure 2.10 Stability studies of  $\text{TiO}_2/\text{FTO}$  photoanodes under simulated solar light in the presence of water oxidation catalyst  $\text{Ni}_5\text{-POM}$  ( $20 \mu\text{M}$  in  $0.050 \text{ M}$  pH 9.0 borate buffer) for the time region of (a) 0-200 s, (b) 1800-2000 s, and (c) 3800-4000 s. Potentials applied at step 1: 0 V vs Ag/AgCl and step 2: 1.10 V vs Ag/AgCl.

### 2.3.5 Detection of Oxygen

$\text{O}_2$  detection and its concentration evaluation were carried out using a dissolved oxygen (DO) sensor during multi-potential pulse experiments as discussed in Section 3.2.3. The cell was degassed with ultrapure  $\text{N}_2$  (Airgas, Hattiesburg, MS, USA) for 15 min prior to the start of the experiment, and was placed under a  $\text{N}_2$  blanket throughout the course of measurements. As the oxygen sensor was placed near the photoelectrode, the recorded DO levels should be a reflection of instant local oxygen concentrations. It can

be seen from Figure 2.11 that under AM 1.5G irradiation the DO concentration generated from the TiO<sub>2</sub>/FTO electrode in the presence of Ni<sub>5</sub>-POM (Figure 2.11e) is much higher than that in its absence (Figure 2.11d). As expected, the corresponding DO concentration produced in the dark is remarkably lower than its counterpart (Figure 2.11 (e) vs 2.11 (c) and Figure 2.11d vs 2.11b). Note that the oxygen produced from the present photoelectrochemical setup, for example, 0.18 ppm from the TiO<sub>2</sub>/FTO-Ni<sub>5</sub>-POM system after 200 s light irradiation (Figure 2.11e), is limited as compared with the amount of DO at 100% saturation in water (8.68 ppm at 1 atm at 21 °C).<sup>117</sup> Note also that precise quantification of O<sub>2</sub> and the faradaic efficiency are found to be difficult due to practical constrains in our current photoelectrochemical cell setup and the charging current produced during the photoelectrochemical oxidation. Table 2.3 presents the faradaic efficiencies estimated on the basis of oxygen measured at different time intervals on the FTO/TiO<sub>2</sub> electrode in the presence of Ni<sub>5</sub>-POM under simulated solar irradiation, where an average faradaic efficiency of ~294% is obtained.

Table 2.3 Oxygen Quantification and faradaic efficiency.

<b>Time (s)</b>	<b>DO (ppm)</b>	<b>Moles of O<sub>2</sub> (mol)</b>	<b>Experimental charge (C)</b>	<b>Theoretical charge (based on observed DO)</b>	<b>Faradaic efficiency %</b>
50	0.04	6.25E-08	8.45E-03	0.024125	285.6686126
100	0.07	1.09375E-07	1.66E-02	0.04221875	255.0981873
150	0.14	2.1875E-07	2.47E-02	0.0844375	342.2401913
200	0.16	2.5E-07	3.27E-02	0.0965	295.5408551
Average					294.6369616

Such a high faradaic efficiency probably results from the fact that the oxygen sensor was placed near the photoanode, leading to the reporting of a much higher local oxygen concentration rather than a well-spread average oxygen level. In other words, the measured oxygen concentration is approximately three times of the actual concentration of oxygen in a well-mixed solution. Nevertheless, the overall DO data trends presented in Figure 2.11 point at the fact that obtained photocurrent is indeed due to oxygen evolution, and correlate well with the results obtained from photocurrent and impedance measurements that point at the role of Ni<sub>5</sub>-POM with respect to increased water oxidation photocurrent and reduced onset potential by means of enhanced charge separation and catalytic activity (see Sections 2.3.2).

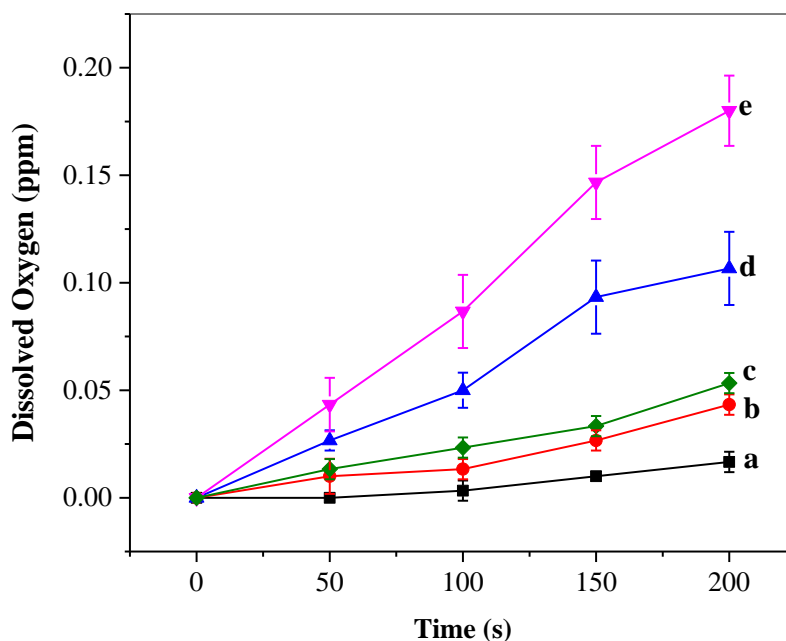


Figure 2.11 Dissolved oxygen (DO) for (a) borate buffer blank, (b) during multi-potential step experiments in the absence and (c) presence of water oxidation catalyst Ni<sub>5</sub>-POM (20 μM in 0.050 M pH 9.0 borate buffer) under dark conditions, (d) TiO<sub>2</sub>/FTO photoanodes in the absence and (e) presence of water oxidation catalyst Ni<sub>5</sub>-POM (20 μM in 0.050 M pH 9.0 borate buffer) under simulated solar irradiation.

The turnover number (TON) and turnover frequency (TOF) for this system were calculated to be 0.085 and 1.5 h<sup>-1</sup> based on the number of moles of oxygen evolved (250 nmole) within 200 s at the FTO/TiO<sub>2</sub> photoanode in the presence of Ni<sub>5</sub>-POM (20 μM in 50.0 mL or 1000 nmole) under simulated solar irradiation, with the assumption of 100% faradaic efficiency and Ni<sub>5</sub>-POM as the sole catalytic contributor. Clearly, TOF is a better expression of the catalytic activity than TON, as the latter will increase with the increase of the experimental time. A number of factors, including the rate of diffusion of the homogenous catalyst to and from the electrode surface, the deactivation of the catalyst during the course of electrolysis, as well as the overpotential, could significantly affect

the TON and TOF of a homogeneous electrocatalyst system.<sup>118</sup> Hence, the TON and TOF obtained from the above simplified calculations must be used and interpreted cautiously. On the other hand, from an industrial standpoint of view, the use of homogenous catalysts has unique advantages over heterogeneous co-catalysts, because stability of catalyst films in the face of prolonged gas evolution is not a factor, and it is more convenient to design flow systems that can replace inactivated homogenous catalysts.

## 2.4 Conclusion

Photoelectrochemical studies on water oxidation catalyst Ni<sub>5</sub>-POM for solar water splitting using spin coated TiO<sub>2</sub>/FTO photoanodes were reported. TiO<sub>2</sub> film was characterized with SEM, EDX, and UV-vis spectroscopy. The three-electrode photocurrent measurements revealed significant increase in photocurrent and negative shift in onset potential of water oxidation upon the addition of 20 μM Ni<sub>5</sub>-POM water oxidation catalyst. As verified by EIS data, these observations were attributed to increased electron-hole separation of TiO<sub>2</sub> and catalysis of water oxidation reaction resulting from capture and utilization of photo-generated holes by the catalyst. At zero biased potential, the TiO<sub>2</sub>/FTO-Ni<sub>5</sub>-POM system displayed a notable photocurrent, which is significant considering the unbiased photocurrent was produced from anatase TiO<sub>2</sub> photoelectrode under simulated solar light. Multi-potential step experiments revealed that the cracked TiO<sub>2</sub> film on FTO was stable even under a harsh experimental parameter of 1.10 V vs Ag/AgCl in the presence of Ni<sub>5</sub>-POM catalyst and simulated solar irradiation. Oxygen produced from the TiO<sub>2</sub>/FTO-Ni<sub>5</sub>-POM system was detected. Moving forward with the results of this investigation, future studies on the use of homogenous POM based catalysts are expected to focus on their integration with lower bandgap photoanodes and

possible application as co-catalysts in tandem water splitting, with the objective of designing high efficiency solar fuel conversion devices.



CHAPTER III - PHOTOELECTROCHEMICAL INVESTIGATIONS ON COBALT  
POLYOXOMETALATES AS CO-CATALYSTS FOR SOLAR WATER REDUCTION  
USING  $\text{Cu}_x\text{Se}$  PHOTOCATHODES

### 3.1 Introduction

In terms of global power generating capacity, solar energy ranks the highest amongst all sustainable energy sources with a potential to deliver over 20 TW.<sup>12</sup> Hydrogen has been considered as one of the primary energy sources of the future due to its high volumetric power density and potential for green combustion, and photoelectrochemical (PEC) water splitting makes direct use of solar energy incident on semiconductor photoelectrodes and is a convenient, economic option to produce high purity hydrogen at low temperatures.

A variety of photocathodes based on inorganic semiconductor materials such as p- $\text{Cu}_2\text{O}$ <sup>119-122</sup> and CdS have been developed and optimized over the years for use in solar water reduction. Copper selenide ( $\text{Cu}_x\text{Se}$ ) is a stable, low band gap chalcogenide based semiconductor material with a broad solar absorption range. It has been used primarily in thermoelectric devices,<sup>123-126</sup> ion selective sensors,<sup>127</sup> and in protective black coatings. Copper Indium Gallium Selenide (CIGS) is a well-studied hybrid I-III-VI material used in photovoltaics.<sup>128-130</sup> However, there have limited reports on the application of  $\text{Cu}_x\text{Se}$  for PEC water splitting. Studies in this chapter provide an insight on the PEC properties of  $\text{Cu}_x\text{Se}$  for solar water reduction.

Co-catalysts play a vital role in PEC water splitting process by reducing the overpotential for water reduction and oxidation, and also facilitating greater exciton density through rendering efficient charge separation.<sup>23, 34, 91, 94, 118</sup> Pt has been the most

efficient catalyst reported for hydrogen evolution reaction (HER), with its activity arising from near zero free energy of hydrogen atom adsorption.<sup>40-41</sup> However, the prohibitive cost of noble metal based catalysts necessitates the development of alternate earth abundant material based systems for solar water splitting.

Polyoxometalates (POMs) are transition metal oxo-anion cluster frameworks linked by common oxygen atoms. There has been a wide spectrum of current research focused on the catalytic applications of POMs.<sup>51-53, 55, 57-59, 62, 64, 67-68, 98, 100</sup> They can be efficient water splitting catalysts due to (1) facile reversible multi-electron transport kinetics within the POM architecture, (2) stabilization of active transition metals, (3) possibility for co-ordination of multi-metal cores, which effectively increases the number of active sites, and (4) absence of organic moieties in the POMs employed, increasing their stability. POMs based on Ru,<sup>57, 98</sup> Co<sup>65-67, 95, 97</sup> and Ni<sup>68</sup> have been previously studied for photochemical and electrocatalytic water splitting. However, a majority of these studies have focused more on the water oxidation compared to water reduction. Also, electrocatalytic water splitting still demands the application of significant external bias, and the use of photocatalytic methods for large scale device applications come with engineering constraints for O<sub>2</sub>/H<sub>2</sub> gas separation. PEC water splitting with the transition metal based catalysts could provide an efficient, localized system to split water and produce high purity O<sub>2</sub>/H<sub>2</sub> under unbiased or low applied bias (external potential) conditions.

The use of homogenous water splitting catalysts in solution offers a variety of advantages for PEC applications, including fast reaction kinetics, low electric resistance, and facile photoelectrode fabrication. Moreover, on an industrial standpoint they unique

advantages over heterogeneous co-catalysts, since stability of catalyst films in the face of prolonged gas evolution is not a factor, and it is more convenient to design flow systems that can replace inactivated homogeneous catalysts.

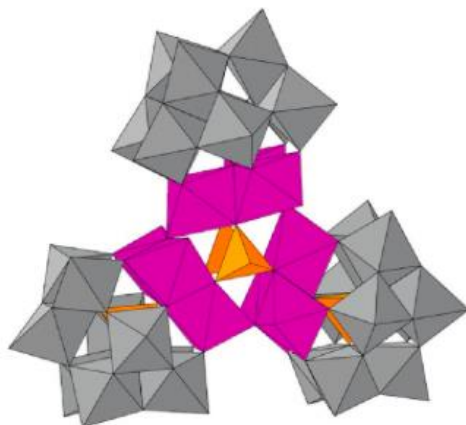


Figure 3.1 Molecular structure of Co<sub>9</sub>-POM (WO<sub>6</sub>: Grey Octahedra, CoO<sub>6</sub>: Pink Octahedra, PO<sub>4</sub>: Yellow Tetrahedra). Obtained with permission from Ref. 131.

$[\text{Co}_9(\text{OH})_3(\text{H}_2\text{O})_6(\text{HPO}_4)_2(\text{PW}_9\text{O}_{34})_3]^{16-}$  (Co<sub>9</sub>-POM) is a high nuclearity nonacobalt POM which consists of three trilacunary B- $\alpha$ -keggin units, with three Co<sup>2+</sup> ions occupying the octahedral vacant positions in each vacant fragment.<sup>131</sup> Three hydroxyl bridges and two HPO<sub>4</sub><sup>-</sup> anions connect the three keggin fragments, forming a triangle of triangles. It has been studied as an active catalyst for homogeneous and heterogeneous electrocatalytic water oxidation.<sup>131</sup> However, there are limited reports on its application for water reduction catalysis and PEC water splitting to the best of our knowledge. In this study, we report for the first time the application of Co<sub>9</sub>-POM as an earth abundant homogeneous co-catalyst for PEC water reduction with Cu<sub>x</sub>Se photocathodes.

## 3.2 Materials and Methods

### 3.2.1 Chemicals

Copper sulfate pentahydrate (ACS reagent), sulfuric acid (ACS reagent), sodium tungstate dehydrate (99%), disodium phosphate (99%), and cobalt acetate tetrahydrate (Reagent grade) were obtained from Aldrich. Sodium acetate (99%) and sodium selenite (99.75%) were obtained from Matheson Coleman and Bell and Alpha Aesar respectively. Deionized water produced from Millipore Advantage 5 was used for the preparation of all aqueous solutions.

### 3.2.2 Preparation of $\text{Cu}_x\text{Se}$ Photocathodes and $\text{Co}_9\text{-POM}$

The  $\text{Cu}_x\text{Se}$  thin films were prepared by potentiostatic electrodeposition method<sup>127</sup> on FTO substrates at -0.50 V vs Ag/AgCl (3.0 M KCl) in a bath containing 0.30 M  $\text{CuSO}_4$ , 0.0050 M  $\text{Na}_2\text{SeO}_3$  and 0.50 M  $\text{H}_2\text{SO}_4$  for 15 min without stirring. The deposition bath was purged with  $\text{N}_2$  (Airgas) for 15 min before the electrodeposition, and a nitrogen blanket was maintained on the headspace throughout the experiment. Prior to the deposition of  $\text{Cu}_x\text{Se}$ , the FTO substrates were cleaned by sonication in deionized water, methanol, acetone, isopropanol, and deionized water, each for 15 min, respectively. This was followed by sintering at 673 K for 2 h and gradual cooling to produce the greyish-black  $\text{Cu}_x\text{Se}$  photoelectrode for study. No color change was observed during the heating process. Synthesis of  $\text{Co}_9\text{-POM}$  catalyst was done adapting procedures reported previously.<sup>132</sup> Briefly, 0.10 mol (33.00 g) of  $\text{Na}_2\text{WO}_4$  and 0.023 mol (3.30 g) of  $\text{Na}_2\text{HPO}_4$  were dissolved in 95 mL of water and the pH was adjusted to 7.0 using glacial acetic acid (~25 mL). This solution was added slowly in solution containing 0.036 mol (9.00 g) of  $\text{Co}(\text{Ac})_2$  in 30 mL of water. The resulting violet mixture was refluxed for 2 h

and filtered. An aqueous solution of sodium acetate (0.020 mol (1.60 g) in 5 mL) was added to the filtrate, and it was slowly cooled resulting in the precipitation of a pink solid. The crude product was recrystallized in hot water and slowly evaporated to produce dark pink crystals of Co<sub>9</sub>-POM for the study.

### **3.2.3 Physico-Chemical Characterization**

Scanning electron microscopic (SEM) images of Cu<sub>x</sub>Se electrodes on FTO substrate were obtained with a Zeiss Sigma VP FEG SEM. An Evolution 300 Thermo-Scientific spectrophotometer was used to obtain the UV-vis spectrum of Cu<sub>x</sub>Se photoelectrodes. Mass spectrometric (MS) analysis of Co<sub>9</sub>-POM was conducted using a Thermo-Fischer LXQ ESI-ion trap mass spectrometer (Waltham, MA, USA). The MS spectrum was obtained using a 0.50 mg/mL sample concentration with water as the solvent, at a flow rate of 100 μL/min in negative ion mode.

### **3.2.4 Photoelectrochemical Measurements**

PEC measurements were carried out in a three-electrode electrochemical setup using a 50 mL quartz beaker as the cell, with an Ag/AgCl (3.0 M KCl), Pt wire, and the FTO/Cu<sub>x</sub>Se (1 cm<sup>2</sup>) as the reference, counter and working electrodes, respectively. A 0.050 M pH 9.0 borate buffer solution was used as the electrolyte for all experiments with and without the presence of 20 μM Co<sub>9</sub>-POM catalyst. Electrochemical impedance spectroscopic (EIS) measurements were carried out under open circuit potential with a 5 mV AC signal super-imposed. Mott Schottky plots were collected at a frequency of 962 Hz. An electrochemical workstation (CH instruments model 660 A) was used for conducting electrochemical experiments. Simulated solar light for PEC studies was

provided by a 150 W Xe lamp solar simulator (ABET technologies) with an AM 1.5 G filter providing a light intensity of  $1000 \text{ W/m}^2$  (1 sun).

### 3.3 Results and Discussion

#### 3.3.1 Physico-Chemical Characterization

The surface morphology of FTO/ $\text{Cu}_x\text{Se}$  films obtained by electrodeposition at -0.5 V vs Ag/AgCl was characterized by scanning electron microscopy (SEM). Figures 3.2a and 3.2b elucidate the SEM images recorded at 1.50 KX and 2.60 KX magnification respectively. A rough, densely covered, and spongy  $\text{Cu}_x\text{Se}$  photocatalyst film is observed. Apart from occasional agglomerations, the  $\text{Cu}_x\text{Se}$  film on FTO was evenly deposited with complete coverage. The spongy nature of the film and roughness renders a high surface area and presents more active spots for photocatalysis. This could result in high charge carrier mobility and photo-activity.<sup>12</sup>

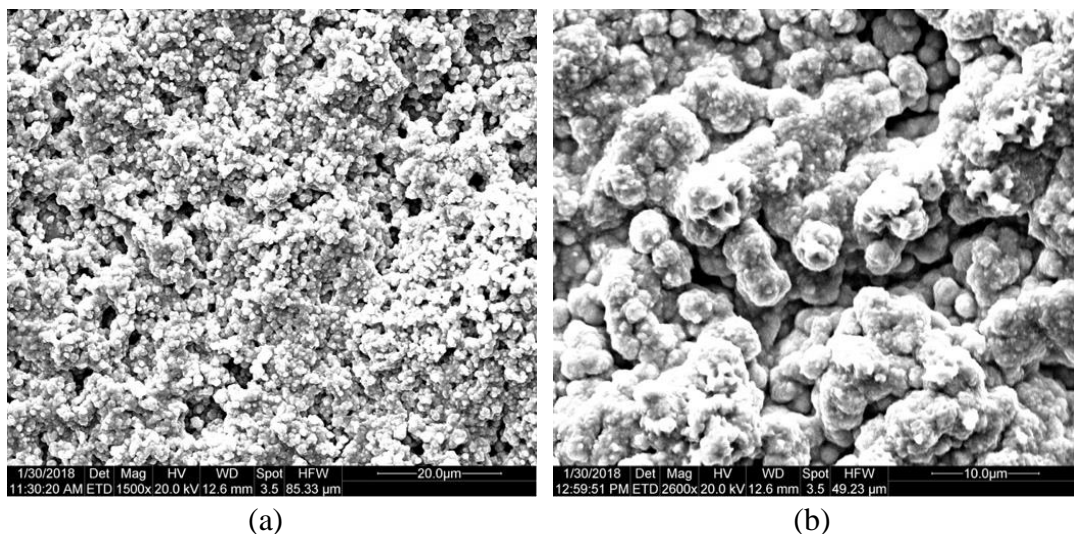
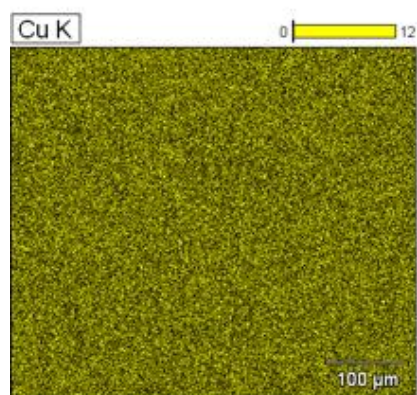
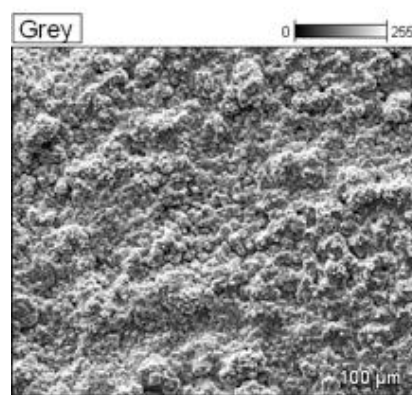


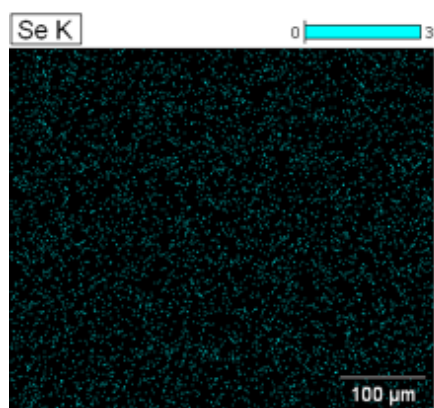
Figure 3.2 SEM images of electrodeposited  $\text{Cu}_x\text{Se}$  films with a deposition potential of -0.5 V vs Ag/AgCl on FTO substrate at (a) 1.50 KX, and (b) 2.60 KX.



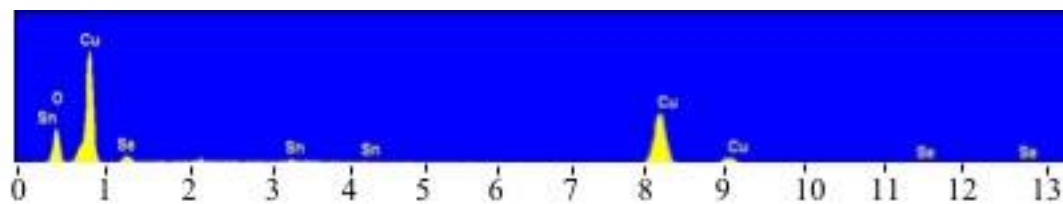
(a)



(c)



(b)



(d)

Figure 3.3 EDX maps of electrodeposited FTO/Cu<sub>x</sub>Se films on FTO substrate at (a) Cu and (b) Se, using (c) the sample area. (d) EDX spectrum of FTO/Cu<sub>x</sub>Se.

Figures 3.3a and 3.3b are the energy dispersive X ray (EDX) maps of an FTO/Cu<sub>x</sub>Se sample area (Figure 3.3c), indicating the distribution of Cu and Se respectively. It can be seen from the map that Cu and Se are evenly dispersed across the measured area. Figure 3.3d is the EDX spectrum of FTO/Cu<sub>x</sub>Se, showing the peaks for Cu, Se, Sn and O. Approximate weight percentages of Cu and Se were 72.42% and 0.81% respectively, and corresponded to a Cu:Se mole ratio of 110:1. However, this estimation is based on the ability of the EDX detector to sense Se locally, and the relative distribution of local elements may cause under-estimation of obtained values. Figure 3.4 provides the UV-vis spectrum of FTO/Cu<sub>x</sub>Se, with FTO used as a blank during the measurement. A broad absorption range is observed across the visible part of the spectrum, and an approximate band gap of 1.48 eV was calculated (from the absorption edge at 840 nm), which is consistent with the range of values reported in the literature<sup>133-134</sup> for copper selenide films. Hence, Cu<sub>x</sub>Se can effectively absorb light across a broad range of the solar spectrum. Mass spectrometry was used for the characterization of Co<sub>9</sub>-POM (Figure 3.5). As revealed in Figure 3.5 and Table 3.1, a number of observed mass/charge (m/z) peaks, such as those at 969.26, 963.74, 958.25, 955.55, 952.25, 950.00, 1957.15, 1934.00, 1923.00 and 1917.50, are consistent with the POM related fragments, [Na<sub>8</sub>X]<sup>8-</sup>, [Na<sub>6</sub>H<sub>2</sub>X]<sup>8-</sup>, [Na<sub>4</sub>H<sub>4</sub>X]<sup>8-</sup>, [Na<sub>3</sub>H<sub>5</sub>X]<sup>8-</sup>, [Na<sub>2</sub>H<sub>6</sub>X]<sup>8-</sup>, [NaH<sub>7</sub>X]<sup>8-</sup>, [Na<sub>11</sub>HX]<sup>4-</sup>, [Na<sub>7</sub>H<sub>5</sub>X]<sup>4-</sup>, [Na<sub>5</sub>H<sub>7</sub>X]<sup>4-</sup>, and [Na<sub>4</sub>H<sub>8</sub>X]<sup>4-</sup> respectively, where X = Co<sub>9</sub>(H<sub>2</sub>O)<sub>6</sub>(OH)<sub>3</sub>(HPO<sub>4</sub>)<sub>2</sub>(PW<sub>9</sub>O<sub>34</sub>)<sub>3</sub>.



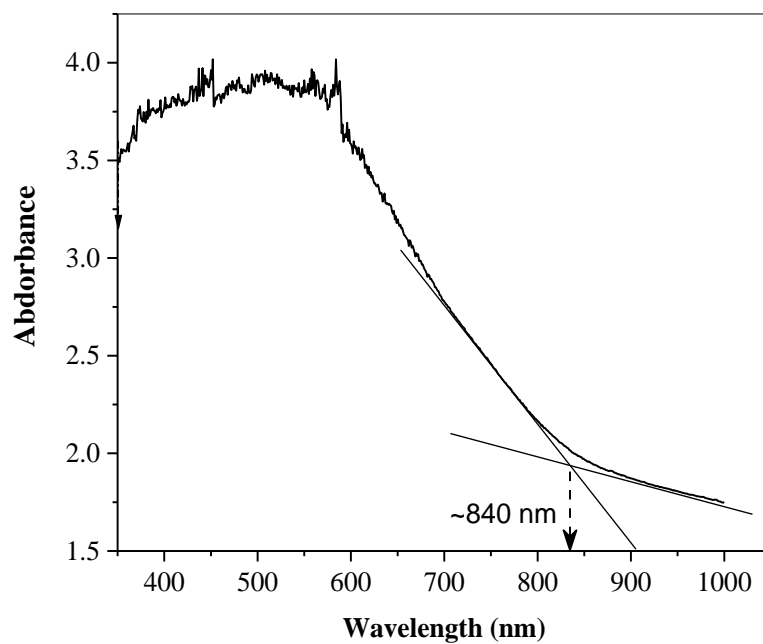


Figure 3.4 UV-vis spectra of  $\text{Cu}_x\text{Se}$  film on FTO substrate.

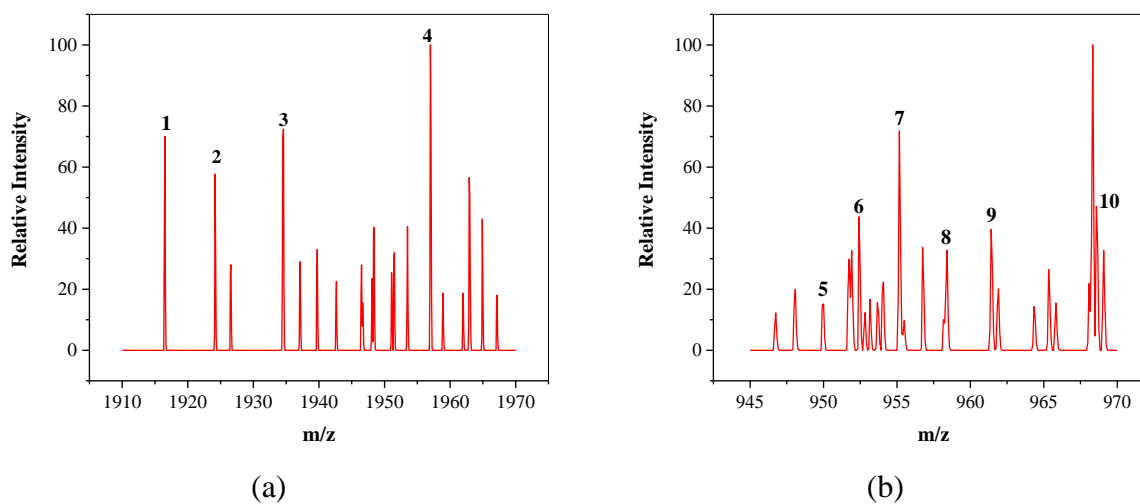


Figure 3.5 Mass spectra of  $\text{Co}_9\text{-POM}$  catalyst in (a) 1900-1800 and (b) 940-980  $m/z$  range.

Table 3.1 Mass spectral peak assignments for Co<sub>9</sub>-POM catalyst.

Peak <sup>a</sup>	m/z		Formula <sup>b</sup>
	Experimental	Predicted	
1	1917.50	1917.5	[Na <sub>4</sub> H <sub>8</sub> X] <sup>4-</sup>
2	1923.00	1923.00	[Na <sub>5</sub> H <sub>7</sub> X] <sup>4-</sup>
3	1934.00	1934.00	[Na <sub>7</sub> H <sub>5</sub> X] <sup>4-</sup>
4	1957.15	1956.5	[Na <sub>11</sub> HX] <sup>4-</sup>
5	950.00	950.00	[NaH <sub>7</sub> X] <sup>8-</sup>
6	952.25	952.75	[Na <sub>2</sub> H <sub>6</sub> X] <sup>8-</sup>
7	955.55	955.50	[Na <sub>3</sub> H <sub>5</sub> X] <sup>8-</sup>
8	958.25	958.25	[Na <sub>4</sub> H <sub>4</sub> X] <sup>8-</sup>
9	963.74	963.80	[Na <sub>6</sub> H <sub>2</sub> X] <sup>8-</sup>
10	969.26	969.25	[Na <sub>8</sub> X] <sup>8-</sup>
<sup>a</sup> from Figure 3.4, <sup>b</sup> X = Co <sub>9</sub> (H <sub>2</sub> O) <sub>6</sub> (OH) <sub>3</sub> (HPO <sub>4</sub> ) <sub>2</sub> (PW <sub>9</sub> O <sub>34</sub> ) <sub>3</sub> .			

### 3.3.2 Photocurrent Measurements

Photoelectrochemical studies were conducted for the understanding of photoelectrode-catalyst interactions and determining the overall effectiveness of Co<sub>9</sub>-POM catalyst in rendering solar hydrogen production.

As discussed in the Chapter I (Section 1.4.1.1), metal selenide films can be deposited by under-potential co-deposition technique. When the deposition potential is shifted further along the negative direction after initial reduction of Se<sup>4+</sup> to Se<sup>0</sup>, the amount of metal increases (i.e. Cu in the present case) and the amount of Se decreases. This observation has been discussed in previous studies on the electrodeposition of metal selenides,<sup>135-136</sup> and could have an effect on the photoelectrochemical behavior of Cu<sub>x</sub>Se. Figure 3.6 depicts the effect of electrodeposition potential on photocurrent density of

FTO/Cu<sub>x</sub>Se photocathodes at -0.40 V vs Ag/AgCl under simulated solar light irradiation. The maximum overall photocurrent density is obtained for photoelectrode deposited at -0.50 V vs Ag/AgCl. Hence, the FTO/Cu<sub>x</sub>Se photocathodes deposited at -0.50 V were used for all further experiments.

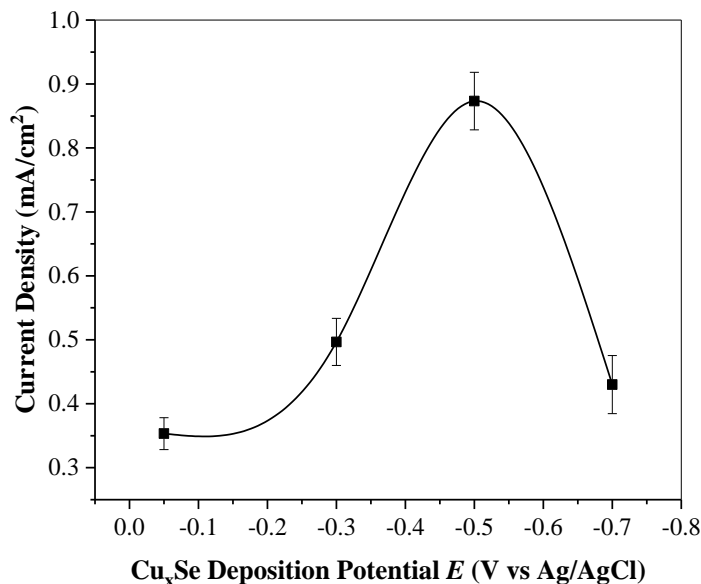


Figure 3.6 Dependence of HER current density at -0.40 V vs Ag/AgCl on Cu<sub>x</sub>Se electrodeposition potential.

Figure 3.7 shows the linear sweep voltammograms obtained from FTO/Cu<sub>x</sub>Se photocathodes in the absence (Figure 3.7a) and presence (Figure 3.7b) of water reduction catalyst Co<sub>9</sub>-POM (20 μM in 0.050 M pH 9.0 borate buffer) under dark conditions and the photocathodes in the absence (Figure 3.7c) and presence (Figure 3.7d) of Co<sub>9</sub>-POM catalyst (20 μM in 0.050 M pH 9.0 borate buffer) under simulated solar radiation, respectively. This catalyst concentration was chosen since higher amounts of catalyst lead to a loss in solubility and formation of mild pink coloured solutions/light absorption. In the absence of light illumination, it can be seen that negligible to small current is

produced both in the absence and presence of catalyst. Although, the overall current density in the presence of the catalyst (Figure 3.7b) is marginally higher than in its absence (Figure 3.7a). On the other hand, under simulated solar irradiation, a photocurrent density of  $\sim 0.8 \text{ mA/cm}^2$  at  $-0.40 \text{ V}$  vs Ag/AgCl on the FTO/Cu<sub>x</sub>Se photocathode in the absence of Co<sub>9</sub>-POM water reduction catalyst in solution. This photocurrent is increased to  $\sim 1.3 \text{ mA/cm}^2$  after addition of catalyst. In other words, the photocurrent is 1.65 times that in Figure 3.7c. A  $\sim 0.1 \text{ V}$  positive shift in the onset potential can also be observed in the presence of Co<sub>9</sub>-POM under dark, pointing at the electrocatalytic activity of Co<sub>9</sub>-POM. The photocurrents obtained at  $0 \text{ V}$  vs Ag/AgCl under illumination could be attributed to photo-induced charge carrier generation and polarization of the semiconductor electrode, resulting in electron transfer for water reduction. This has been explained in further detail in Chapter I (Section 1.1.2). These above findings suggest that under the present experimental conditions, light irradiation is a prerequisite of water reduction and Co<sub>9</sub>-POM can effectively facilitate the reduction process. The increase in observed photocurrent in the presence of the catalyst points its effectiveness in enhancing electron-hole separation by electron capture from Cu<sub>x</sub>Se to reduce water (as will be discussed in Section 3.3.3). Moreover, the positive shift in onset potential with added Co<sub>9</sub>-POM points at its catalytic activity for HER. The obtained results are comparable and higher compared to recent literature, as shown in Table 3.2.

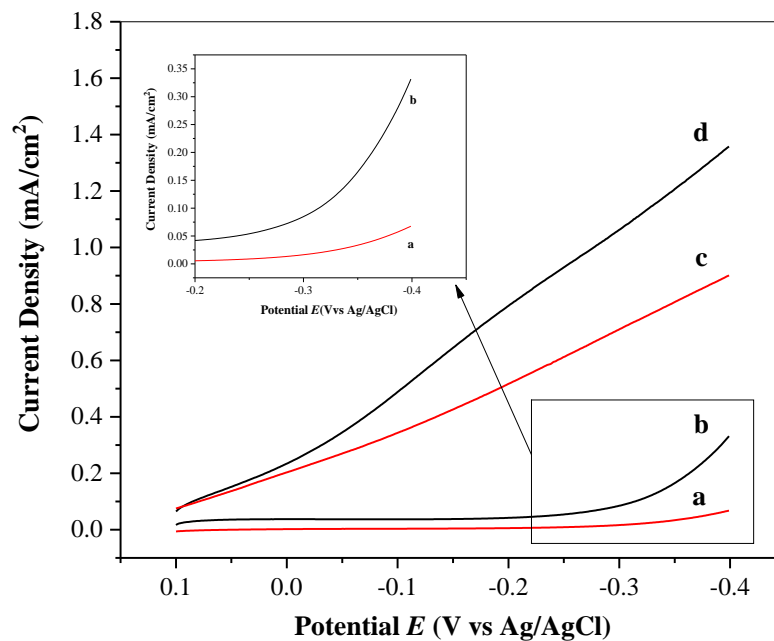


Figure 3.7 Linear sweep voltammograms of FTO/Cu<sub>x</sub>Se photocathodes in the (a) absence and (b) presence of water reduction catalyst Co<sub>9</sub>-POM (20 μM in 0.050 M pH 9.0 borate buffer) under dark conditions and FTO/Cu<sub>x</sub>Se photocathodes in the (c) absence and (d) presence of water reduction catalyst Co<sub>9</sub>-POM (20 μM in 0.050 M pH 9.0 borate buffer) under simulated solar radiation at a scan rate 0.020 V/s.

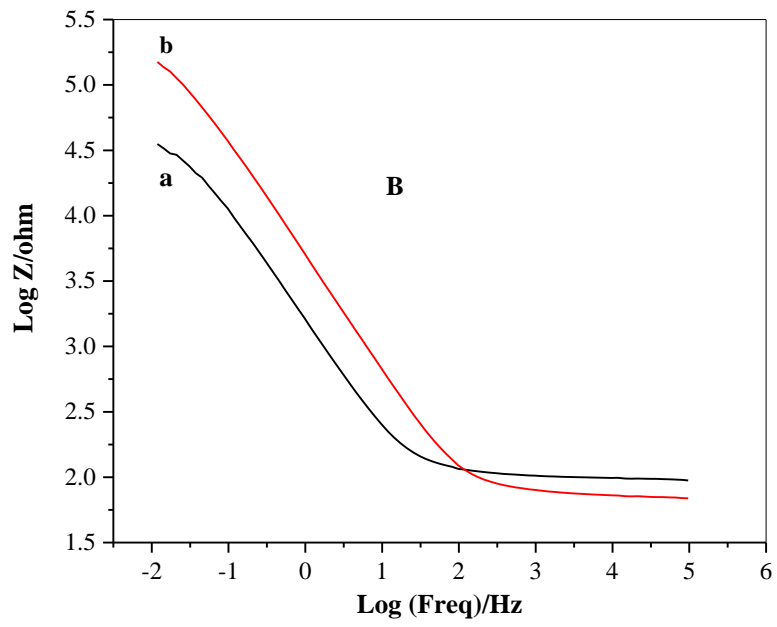
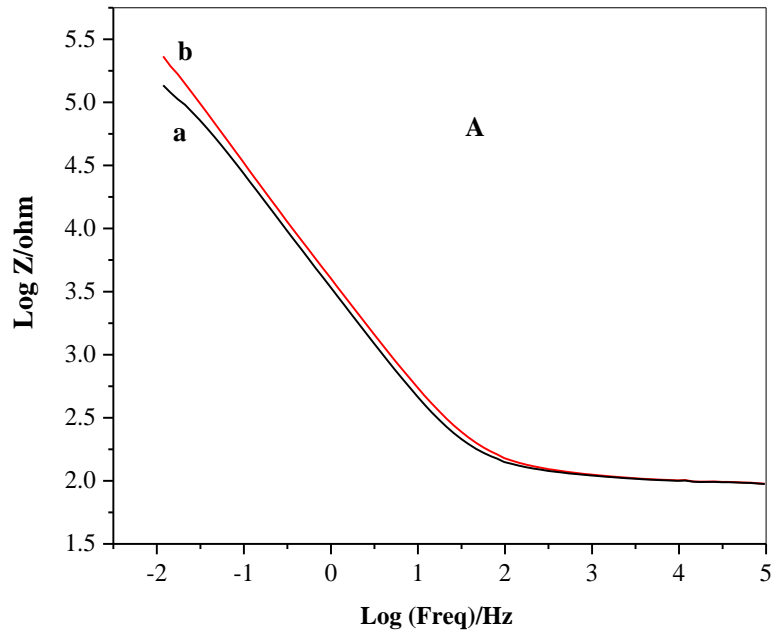
Table 3.2 Comparison of photocurrents obtained at different reported photocathodes for water splitting under various experimental conditions.

Photoelectrode	Electrolyte	Current Density <sup>a</sup> (mA/cm <sup>2</sup> )	Potential $E^b$		Ref.
			Reported	vs Ag/AgCl	
Cu <sub>2</sub> O decorated with cocatalyst MoS <sub>2</sub>	25% (v/v) methanol (scavenger) mixed with Na <sub>2</sub> SO <sub>4</sub> (0.10 mol L <sup>-1</sup> , pH = 7.0) aqueous solution	~0.15	-0.10 V vs SCE	-0.060	137
Cu <sub>2</sub> O with NiFe-layered double hydroxide co-catalyst	0.50 M Na <sub>2</sub> SO <sub>4</sub> solution	~0.49	-0.20 V vs Ag/AgCl	-0.20	138
Cu <sub>2</sub> O photocathode with gold underlayer	0.50 M Na <sub>2</sub> SO <sub>4</sub>	~0.75	0.090 V vs RHE	-0.40	139
Cu <sub>2</sub> O/CuO heterojunction photoelectrode	1 mM Na <sub>2</sub> SO <sub>4</sub>	~1.05	-0.60 V vs. Hg/HgCl <sub>2</sub>	-0.56	140
Hierarchical Cu <sub>2</sub> O foam/g-C <sub>3</sub> N <sub>4</sub> photocathode	0.1 M Na <sub>2</sub> SO <sub>4</sub> at pH 7.0	~1.2	0.21 V vs RHE	-0.40	141
Cu <sub>x</sub> Se in the presence of solution-phase Co <sub>9</sub> -POM	20 μM Co <sub>9</sub> -POM in 50 mM borate buffer, pH 9.0	~1.3 <sup>c,d</sup> mA/cm <sup>2</sup>	-0.40 V vs Ag/AgCl (~0.328 V vs RHE <sup>c</sup> )	-0.40	This work

<sup>a</sup>Positive water reduction current densities have been reported as per ACS convention, <sup>b</sup> $E_{\text{RHE}} = E_{\text{Ag/AgCl}} + 0.059\text{pH} + 0.197$ , <sup>c</sup>~-0.30 mA/cm<sup>2</sup> at -0.060 V vs Ag/AgCl, <sup>d</sup>~-0.80 mA/cm<sup>2</sup> at -0.20 V vs Ag/AgCl.

### 3.3.3 Electrochemical Impedance Spectroscopy

Electrochemical impedance spectroscopic (EIS) measurements were conducted to further co-relate the results from photocurrent studies which point at the effect of Co<sub>9</sub>-POM in increasing electron hole separation through electron collection and catalytic activity. The EIS spectra (Bode plots) obtained from FTO/Cu<sub>x</sub>Se photocathodes under light (Figures 3.8A(a) and 3.8B(a)) and dark (Figures 3.8A(b) and 3.8B(b)) conditions in the absence (Figure 3.8A) and presence (Figure 3.8B) of water reduction catalyst Co<sub>9</sub>-POM have been provided, in which the capacitive impedance values within low frequency regions under dark is much higher than those obtained under similar solar irradiation. This is expected because there is limited photo-induced electron-hole separation under dark conditions as compared with that under light. Figure 3.8C compares the bode plots of FTO/Cu<sub>x</sub>Se photocathodes in the in the presence (Figure 3.8C(a)) and absence (Figure 3.8C(b)) of homogenous water reduction catalyst Co<sub>9</sub>-POM in solution under simulated solar irradiation. It is clear that the low frequency capacitive impedance in the presence of catalyst is significantly lower than in its absence, indicating a higher double layer capacitance with Co<sub>9</sub>-POM in solution. This observation indicates the role of Co<sub>9</sub>-POM in rendering increased electron-hole separation through electron capture and catalytic activity, and complements the photocurrent data (shown in Figure 3.7) which clearly elucidates the increased photocurrent density in the presence of Co<sub>9</sub>-POM.





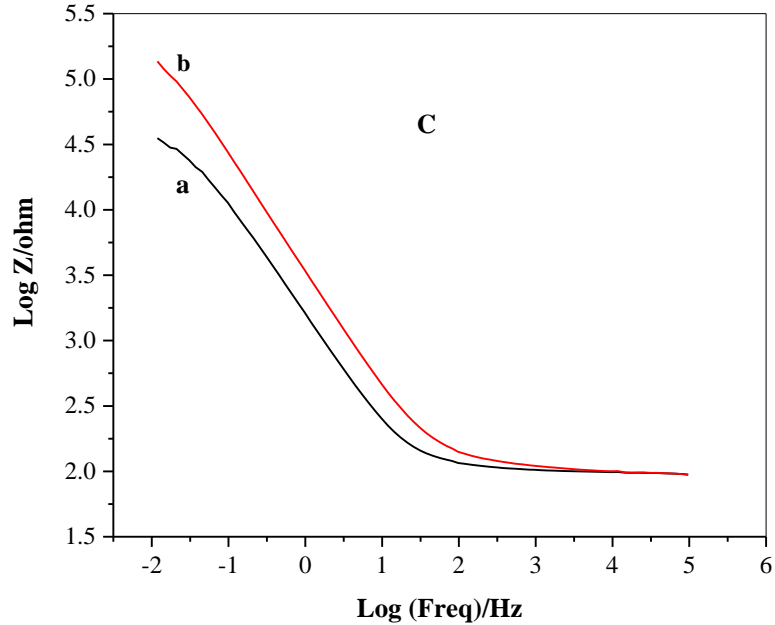


Figure 3.8 Bode plots of FTO/Cu<sub>x</sub>Se photocathodes in the (A) absence and (B) presence of water reduction catalyst Co<sub>9</sub>-POM (20 μM in 0.050 M pH 9 borate buffer) under (a) simulated solar irradiation and (b) dark. (C) Bode plots of FTO/Cu<sub>x</sub>Se photocathodes in the (a) presence and (b) absence of water reduction catalyst Co<sub>9</sub>-POM (20 μM in 0.050 M pH 9.0 borate buffer) under simulated solar irradiation.

### 3.3.4 Mott Schottky Plots

Mott Schottky analysis<sup>85</sup> (Figure 3.9) is an EIS based technique which provides data on the relationship between applied potential and space charge frequencies. The x intercept of the Mott Schottky plot equals  $V_{FB} + kT/e$ , where  $V_{FB}$  is the flat band potential,  $k$  is Boltzmann constant,  $T$  is the temperature, and  $e$  is the charge of an electron. The charge carrier concentration ( $N_D$ ) across the semiconductor (with an area  $A$  and relative permittivity  $\xi_r$ ) electrolyte interface can be computed from the slope of the Mott Schottky plot, in accordance with the following formula:<sup>85</sup>

$$N_D = \frac{1.41 \times 10^{32}(\text{cm} \times \text{F}^{-2} \times \text{V}^{-1})}{\xi_r \times A^2(\text{cm}^4) \times \text{slope I}(\text{F}^{-2} \times \text{V}^{-1})} \quad (3.1)$$

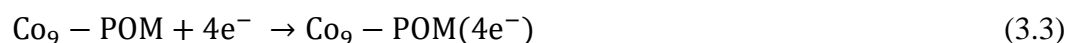
The Mott Schottky measurements were conducted at a frequency of 962 Hz since a significant difference in capacitive impedance and space charge capacitance in the presence of catalyst under light illumination became more observable under the 1000 Hz frequency range (Figure 3.8 (C)). Moreover, this frequency has been used in other reports for studies on semiconductor electrodes and water splitting.<sup>142-144</sup> It can be seen from the Figure 3.8 that the slope of the Mott Schottky plot in the presence (Figure 3.9a) of Co<sub>9</sub>-POM catalyst ( $-6.32 \times 10^9$ ) is lower than that in its absence ( $-2.72 \times 10^{10}$ , Figure 3.9b). Using the obtained Mott Schottky slopes, 1 cm<sup>2</sup> electrode area, and  $\xi_r = 10$ ,<sup>85</sup> the values of  $N_D$  in the absence and presence of catalyst were calculated to be  $2.23 \times 10^{21}$  and  $5.18 \times 10^{20}$  respectively. The negative slope indicates p-type semi-conductivity, which is suitable for HER. The higher value of charge-carrier concentration in the presence of catalyst (~4.3 times) can be attributed to the increased electron-hole separation resulting from electron capture in the presence of the catalyst, and this observation complements data obtained from EIS (Figure 3.8) and photocurrent measurements (Figure 3.7). Hence, it is clear that Co<sub>9</sub>-POM can be an efficient co-catalyst for photoelectrochemical water reduction. It can also be seen from the extrapolated x intercepts of the Mott Schottky plot that a more positive flat band potential can be expected in the presence of the catalyst due to increased electron-hole separation and band bending at the semiconductor electrolyte. Specifically, in presence of catalyst, the flat band potential is calculated to be ~0.43 V vs Ag/AgCl which is ~0.04 V positive as compared to that in the absence of catalyst (~0.39

V vs Ag/AgCl) On the basis of these observations and previous literature<sup>2, 12, 23, 34-35, 58, 91, 94, 118</sup> on co-catalysts for photoelectrochemical water reduction, the following three-step mechanism can be proposed for water reduction by FTO/Cu<sub>x</sub>Se photocathodes in the presence of Co<sub>9</sub>-POM:

Step 1 – Absorption of light by FTO/Cu<sub>x</sub>Se photoelectrode and generation of electron-hole pairs:



Step 2 – Electron capture from Cu<sub>x</sub>Se by Co<sub>9</sub>-POM water reduction catalyst:



Step 3 – Utilization of photogenerated electrons for reduction of water through catalytic pathways

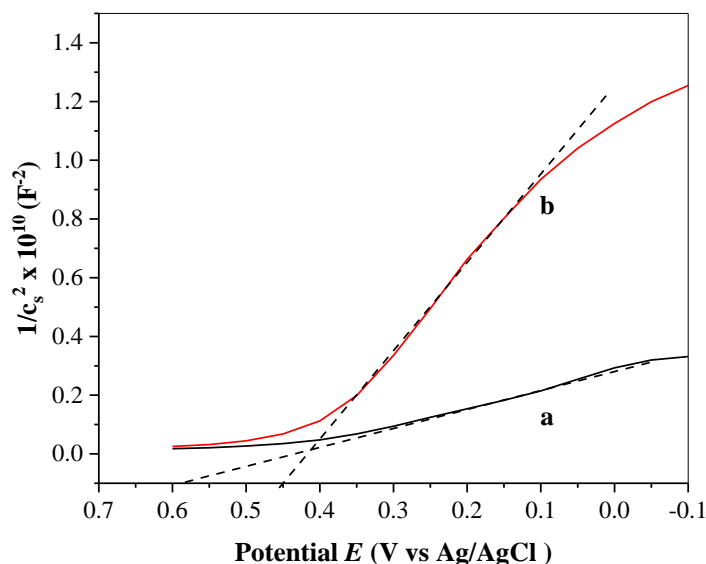
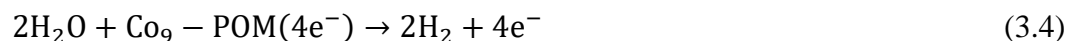
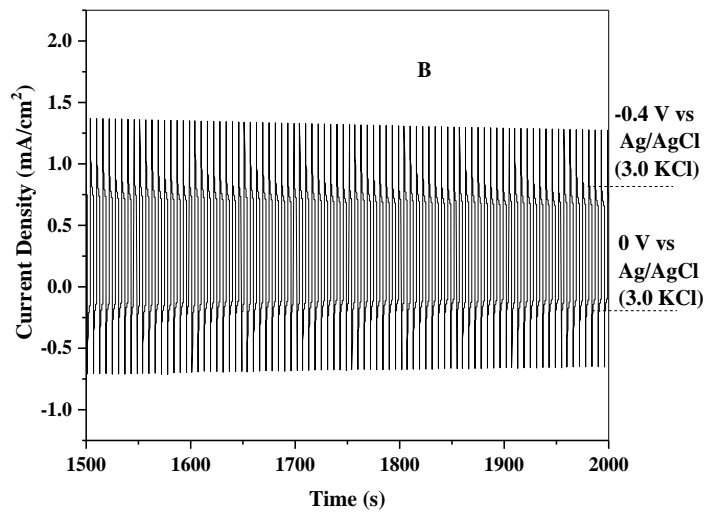
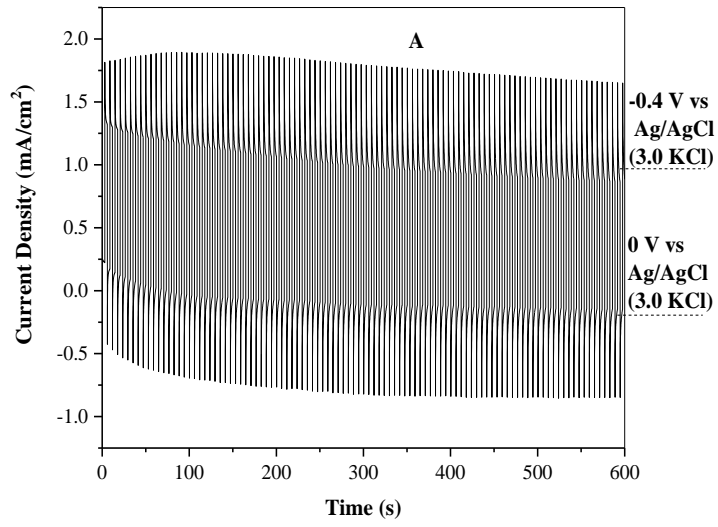


Figure 3.9 Mott Schottky plots of FTO/Cu<sub>x</sub>Se photocathodes in the (a) presence and (b) absence of water reduction catalyst Co<sub>9</sub>-POM (20 μM in 0.050 M pH 9.0 borate buffer) under simulated solar irradiation.

### 3.3.5 Stability Studies

The stability of FTO/Cu<sub>x</sub>Se electrodes for photoelectrochemical water reduction in the presence of Co<sub>9</sub>-POM was evaluated by multiple-potential step and constant potential experiments using a typical three-electrode system. The applied potential was regularly shifted from 0 to -0.40 V vs Ag/AgCl in 3 s intervals for a time period of 2000 s, and responses of photocurrent were recorded. Figures 3.10A and B provide the plots of photocurrent density vs time from a FTO/Cu<sub>x</sub>Se electrode under multi-potential step excitations from two different time regions, namely 0-600 s and 1500-2000 s respectively. Though a decline in photocurrent observed, it is not a true indication of loss in stability since the accumulation of evolved hydrogen gas blocks the electrode surface. This is evidenced by a pattern of current spikes in the observed data, which result from gas release. After the stability measurement, the surface of the photoelectrode exhibited the presence of minor pits owing to extensive gas evolution from the electrode surface. There was no visible formation of films or color change. Figure 3.10C is the linear sweep voltammogram of the FTO/Cu<sub>x</sub>Se photoelectrode after the stability measurement, and indicates a maximum photocurrent of ~1.15 mA/cm<sup>2</sup> at -0.40 V vs Ag/AgCl. This is a minor change from the original photocurrent value (Figure 3.7) prior to stability testing (~1.3 mA/cm<sup>2</sup>) considering the harsh potential step conditions.



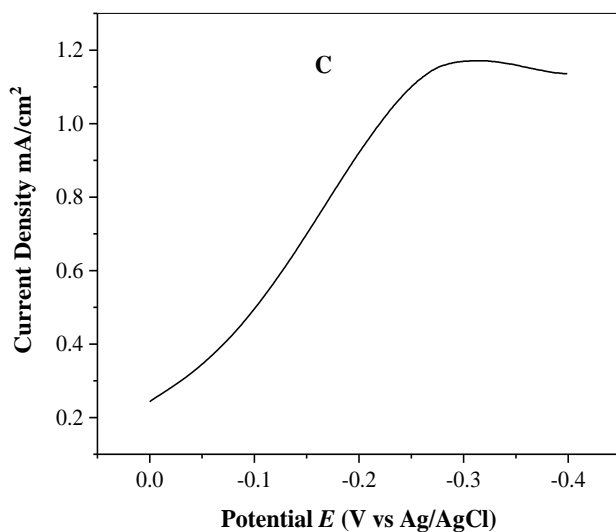


Figure 3.10 Stability studies of FTO/Cu<sub>x</sub>Se photocathodes under simulated solar light in the presence of reduction with catalyst Co<sub>9</sub>-POM (20 μM in 0.050 M pH 9.0 borate buffer) for the time region of (A) 0-600 s, (b) 1500-2000 s, Potentials applied at step 1: 0 V vs Ag/AgCl and step 2: -0.4 V vs Ag/AgCl. (c) Linear sweep voltammogram recorded after stability study.

### 3.4 Conclusion

Photoelectrochemical studies were conducted on electrodeposited FTO/Cu<sub>x</sub>Se photocathodes in the presence of HER catalyst Co<sub>9</sub>-POM. The Cu<sub>x</sub>Se films were characterized with SEM, EDX and UV-vis spectroscopy. The three-electrode photocurrent measurements revealed a significant increase in photocurrent and positive shift in onset potential of water reduction upon the addition of 20 μM Co<sub>9</sub>-POM HER catalyst. These observations were attributed to the increased electron-hole separation of Cu<sub>x</sub>Se and catalysis of water reduction reaction resulting from capture and utilization of photo-generated electrons by the catalyst, as indicated by EIS and Mott Schottky plots. Moving forward with the results of this investigation, future studies on the use of homogenous POM based catalysts are expected to focus on their integration with higher

bandgap photoanodes and possible application as co-catalysts in tandem water splitting, with the objective of designing high efficiency solar fuel conversion devices.

## CHAPTER IV – PHOTOELECTROCHEMICAL STUDIES ON TRANSITION METAL SELENIDE BASED CO-CATALYSTS FOR SOLAR WATER REDUCTION

### 4.1 Introduction

Hydrogen has the highest volumetric energy density amongst conventional fuels, and does not leave a carbon footprint.<sup>12, 14, 145</sup> Photoelectrochemical (PEC) water splitting is an efficient strategy to produce high purity hydrogen under room temperature, and can be used in tandem with fuel cells to design innovative solar energy conversion devices.

p-Cu<sub>2</sub>O<sup>119-122</sup> is a low cost, stable, p-type semiconductor which is being continuously optimized as a photocathode for solar water reduction. It has a band gap of about 2-2.5 eV<sup>145-147</sup> which covers most of the visible region, and has its conduction band edge effectively matching the HER potential.

Co-catalysts play a role in decreasing the hydrogen evolution overpotential and increasing electron-hole separation<sup>23, 34, 91, 94, 118</sup> and photocurrent. Noble metals like Pt and Ru have shown the maximum activity for hydrogen evolution,<sup>40-41</sup> but the prohibitive cost of these materials necessitates the development of low cost alternatives.

In recent years, non-noble transition metal based selenides,<sup>148-149</sup> phosphides<sup>76-77</sup> and sulfides<sup>150-151</sup> have been studied as potential replacements to Pt as HER catalysts.<sup>78, 94</sup> This has been related to enhancements in H-absorption/desorption kinetics upon addition of S, P or Se heteroatoms, as observed by theoretical studies.<sup>78-79, 151</sup> They are stable under electrochemical conditions and a wide operating pH range. In addition, catalysts of tuned composition, thickness and morphology can be produced by simple, inexpensive deposition techniques such as electrodeposition. Studies on using these materials as co-catalysts for photoelectrochemical water splitting have been relatively limited.



In this chapter, the use of electrodeposited transition metal selenide based co-catalysts for solar water reduction with FTO/Cu<sub>2</sub>O photocathodes is presented. Transition metal selenides are ahead of sulfides and phosphides for HER catalysis since bond strength can be considered a factor in enhancing hydrogen desorption from catalytic sites, and the strength of Se-H bonds (276 kJ/mol)<sup>78</sup> is lower than S-H (363 kJ/mol)<sup>78</sup> and P-H (322 kJ/mol).<sup>78</sup> Three electrodeposited HER photocathodes viz. FTO/Cu<sub>2</sub>O-Co<sub>x</sub>Se-Ni<sub>y</sub>Se, FTO/WSe<sub>x</sub>, and FTO/MnSe will be comparatively analyzed for solar water reduction. Among these three, FTO/Cu<sub>2</sub>O-MnSe is shown to have the maximum photocurrent performance. Studies on impedance measurements and dependence of catalyst deposition time on film morphology and composition have been revealed. To our best knowledge, this is the first report on the use of MnSe as a co-catalyst for solar water splitting using Cu<sub>2</sub>O photocathodes.

## **4.2 Materials and Methods**

### **4.2.1 Materials**

Copper sulphate pentahydrate (ACS reagent), lactic acid (85%), sodium hydroxide (98%), cobalt acetate tetrahydrate (Reagent grade), nickel chloride hexahydrate (99%), manganese chloride tetrahydrate (ACS Reagent), sodium tungstate dihydrate (>99%) and lithium chloride (99%) were obtained from Aldrich. Sodium selenite (99.75%) was obtained from Alfa Aesar. Deionized water produced from Millipore Advantage 5 was used for preparing all aqueous solutions.

### **4.2.2 Physico-Chemical Characterization**

Scanning electron microscopic (SEM) images of FTO/Cu<sub>2</sub>O-MnSe electrodes on FTO substrate was obtained with a Zeiss Sigma VP FEG scanning electron microscope.

An Evolution 300 Thermo-Scientific spectrophotometer was used to obtain the UV-vis spectrum of Cu<sub>2</sub>O photoelectrodes.

#### **4.2.3 Preparation of Photocathodes**

FTO/Cu<sub>2</sub>O electrodes were prepared by potentiostatic electrodeposition technique in a lactic acid bath, which has been commonly adapted in number of current reports.<sup>147,</sup>  
<sup>152</sup> The deposition bath consists of 0.40 M CuSO<sub>4</sub>, 3.0 M lactic acid and 4.0 M NaOH at pH 12.0.<sup>152</sup> The FTO substrates were cleaned by sonication in deionized water, methanol, acetone, isopropanol, and deionized water, each for 15 min, respectively, and the electrodeposition was carried out at -0.45 V vs Ag/AgCl for 15 min without stirring. The electrolyte was purged with N<sub>2</sub> (Airgas) for 15 min prior to electrodeposition, and a nitrogen gas blanket was maintained throughout the electrodeposition process. This was followed by annealing at 373 K for 2 h in air to produce the yellowish-orange FTO/Cu<sub>2</sub>O electrode for study. Figure 4.1 is the UV-Vis spectrum of FTO/Cu<sub>2</sub>O, which shows a prominent absorption edge at 510 nm corresponding to a band gap of 2.4 eV. This value is consistent with previous literature on Cu<sub>2</sub>O thin films.<sup>145</sup>

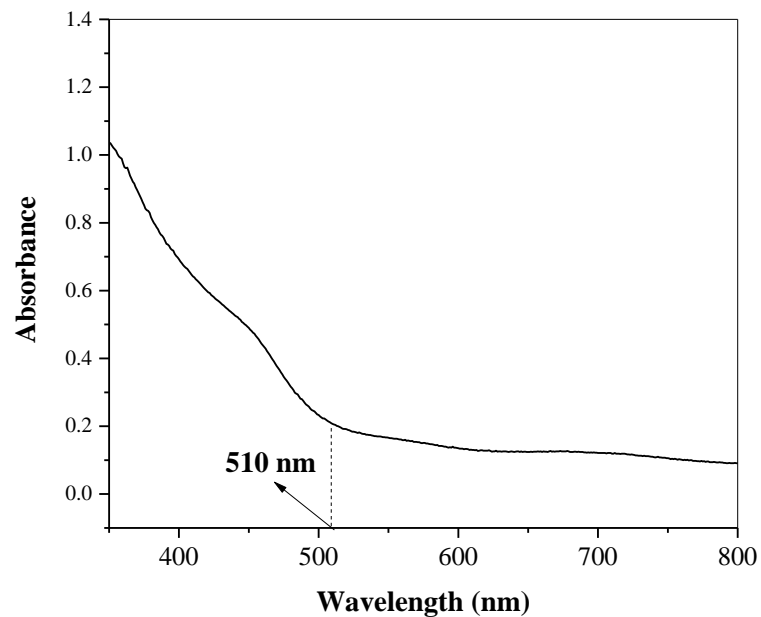


Figure 4.1 UV-Vis spectroscopic plot of FTO/Cu<sub>2</sub>O (Blanked with FTO substrate).

Underpotential electrodeposition was used for the deposition of transition metal chalcogenide based catalysts on FTO/Cu<sub>2</sub>O electrodes at a controlled thickness. The general mechanism of under potential electrodeposition has been provided in Section 1.4.1.1 of the introduction (Chapter I). Electro-deposition baths and deposition voltages for the various catalysts prepared are provided in Table 4.1.

Table 4.1 Electrodeposition conditions for HER catalysts

<b>Photocathode</b>	<b>Catalyst Deposition Bath</b>	<b>Catalyst Deposition Potential vs Ag/AgCl</b>	<b>Ref.</b>
FTO/Cu <sub>2</sub> O-Co <sub>x</sub> Se-Ni <sub>y</sub> Se	10.0 mM NiCl <sub>2</sub> , 10.0 mM Co(Ac) <sub>2</sub> , 100 mM Na <sub>2</sub> SeO <sub>3</sub> , pH 3.5	-0.8 V	153
FTO/Cu <sub>2</sub> O-WSe <sub>x</sub>	0.10 M Na <sub>2</sub> SeO <sub>3</sub> , 0.20 M Na <sub>2</sub> WO <sub>4</sub> , pH 9.6	-0.45 V	154
FTO/Cu <sub>2</sub> O-MnSe	10.0 mM MnCl <sub>2</sub> , 2.0 mM Na <sub>2</sub> SeO <sub>3</sub>	-0.7 V	155

#### 4.2.4 Photoelectrochemical Studies

PEC measurements were carried out in a three-electrode electrochemical setup using a 50 mL quartz beaker as the cell, with Ag/AgCl (3.0 M KCl), a Pt wire, and 1 cm<sup>2</sup> FTO/Cu<sub>2</sub>O/M (where M=MnSe, Co<sub>x</sub>Se-Ni<sub>y</sub>Se, WSe<sub>x</sub>) as the reference, counter, and working electrodes, respectively. Non-conducting parafilm was used to mask the electrode to attain the 1 cm<sup>2</sup> working area. A 0.050 M pH 9.0 borate buffer solution was used as the electrolyte for all experiments with or without the presence of co-catalyst M of different thicknesses, and a scan rate of 0.020 V/s was used for photocurrent measurements. Electrochemical impedance spectroscopic (EIS) measurements were carried out under open circuit potential with a 5 mV AC signal super-imposed. An electrochemical workstation (CH instruments model 660 A) was used for used to conduct electrochemical experiments. Simulated solar light for PEC studies was provided by a 150 W Xe lamp solar simulator (ABET technologies) with an AM 1.5 G filter providing a light intensity of 1000 W/m<sup>2</sup> (1 sun). Figure 4.2 provides a representative cell scheme for photoelectrochemical water splitting using FTO/Cu<sub>2</sub>O-MnSe photocathodes.

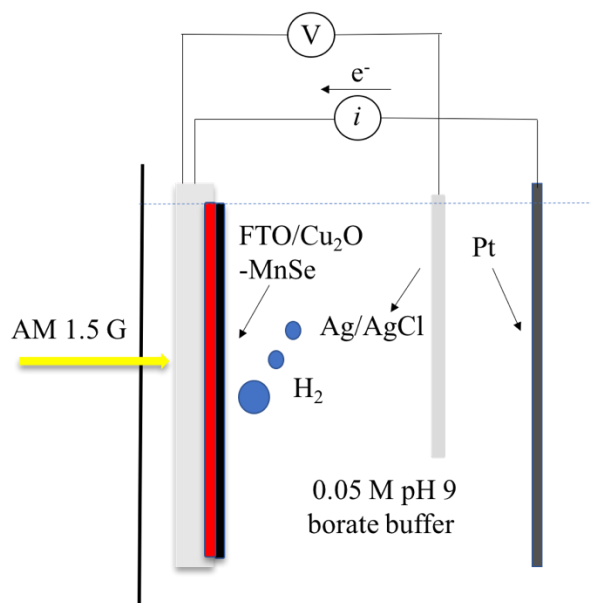


Figure 4.2 PEC cell representation for water splitting using FTO/Cu<sub>2</sub>O-MnSe photocathodes.

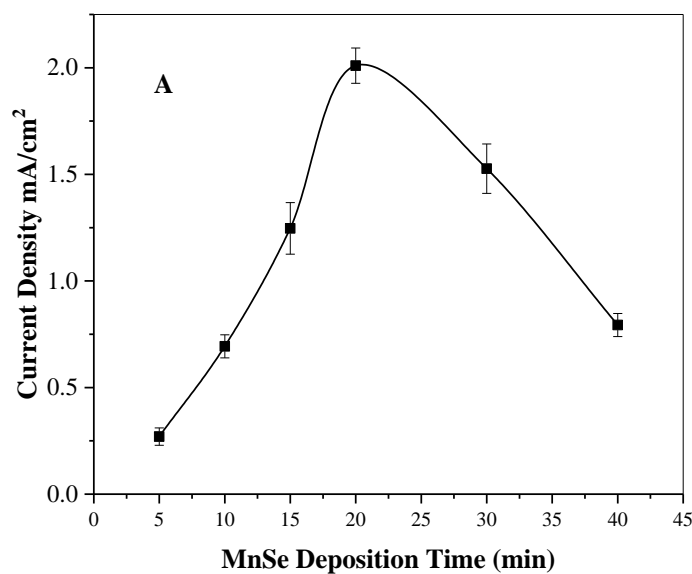
## 4.3 Results and Discussion

### 4.3.1 Photocurrent Measurements and Effect of Catalyst Thickness

Photoelectrochemical studies were conducted for the understanding of photoelectrode-catalyst interactions and determining the overall effectiveness of transition metal chalcogenide based catalysts in rendering solar hydrogen production.

In the case of heterogeneous solid state HER catalysts, it is important to control the electrodeposition time so as to produce a catalyst film of optimal thickness and coverage. A higher catalyst film thickness could lead to increased distance for charge transfer and result in recombination, in addition to increasing resistance and lowering overall conductivity. Figures 4.3 elucidates the relationship between photocurrent and electrodeposition time for FTO/Cu<sub>2</sub>O-MnSe (Figure 4.3A), FTO/Cu<sub>2</sub>O-WSe<sub>x</sub> (Figure 4.3B) and FTO/Cu<sub>2</sub>O-Co<sub>x</sub>Se-Ni<sub>y</sub>Se (Figure 4.3C) at -0.45 V, -0.40 V, and -0.45 V vs Ag/AgCl respectively. It can be seen that the maximum photocurrent increases with

increasing thickness up to a maximum optimal point, after which it starts decreasing. The decrease in maximum photocurrent could be attributed to increased resistance and increased electron-hole recombination due to a higher distance of charge transfer. It can be seen that the FTO/Cu<sub>2</sub>O-MnSe photocathodes deposited for 20 min produce a maximum current density of ~2 mA/cm<sup>2</sup> at -0.45 mA/cm<sup>2</sup> under simulated solar irradiation (Figure 4.3A), while the FTO/Cu<sub>2</sub>O-Co<sub>x</sub>Se-Ni<sub>y</sub>Se (Figure 4.3C) and FTO/Cu<sub>2</sub>O-WSe<sub>x</sub> (Figure 4.3B) electrodes produce a maximum photocurrents of 0.65 and 0.95 mA/cm<sup>2</sup> at -0.45 and -0.40 V vs Ag/AgCl respectively.



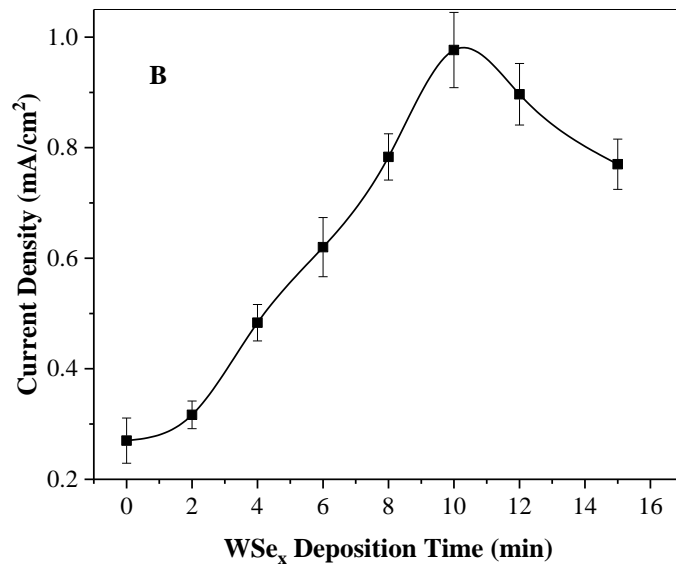
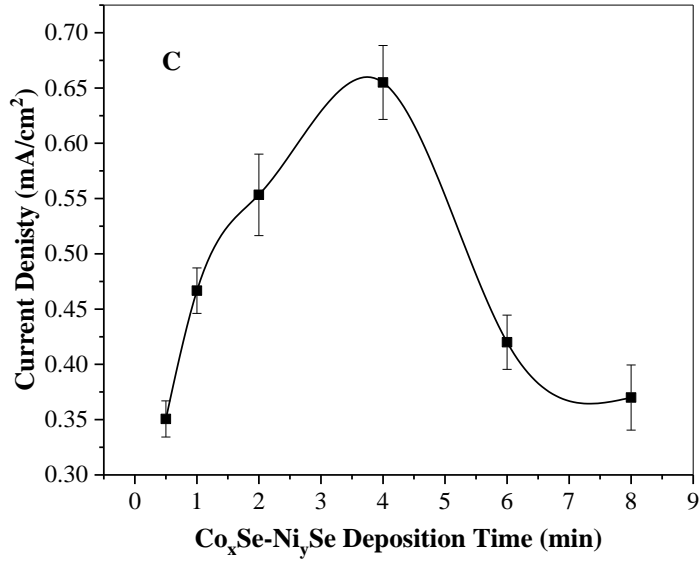
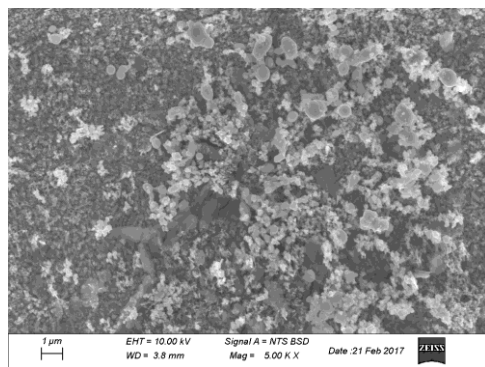


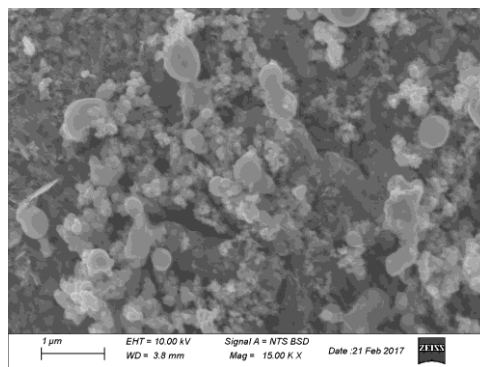
Figure 4.3 Relationship between HER current density at -0.45 V (A,C) or -0.40 V (B) vs Ag/AgCl and catalyst electrodeposition time for (A) FTO/Cu<sub>2</sub>O-MnSe, (B) FTO/Cu<sub>2</sub>O-Co<sub>x</sub>Se-Ni<sub>y</sub>Se and (C) FTO/Cu<sub>2</sub>O-WSe<sub>x</sub>

Figures 4.4 and 4.5 are the SEM images of FTO/Cu<sub>2</sub>O-MnSe photocathodes, depicting the comparison between MnSe catalysts electrodeposited for 20 min (Figure 4.6) and 40 min (Figure 4.5). Figures 4.6a and 4.6b are the EDX spectra of FTO/Cu<sub>2</sub>O-MnSe films electrodeposited for 20 min and 40 min respectively, in which C signal is from the conductive tape and the rest of the elements are constant with the film composition. Table 4.2 provides the weight % and mass ratio and molar ratio of Mn to Se. A molar ratio of 1:1 was estimated for the MnSe catalyst deposited at 20 min. On the other hand, a deposition time of 40 min produced a 2:3 molar ratio of Mn to Se. In general, a porous, spongy catalyst morphology is seen from the SEM images recorded at 5.00 KX (Figure 4.4a and 4.5a) and 15.00 KX (Figure 4.4b and 4.5b) magnification. However, catalyst films deposited for 20 min are less tightly packed and appear as islands compared to the thick, tightly packed films that were formed after a 40 min deposition duration. In addition to decreasing electron-hole recombination, the less packed morphology of the film deposited for 20 min leads could provide more active edge spots for HER catalysis. This is evidenced by the greater current density observed at 20 min (Figure 4.3).



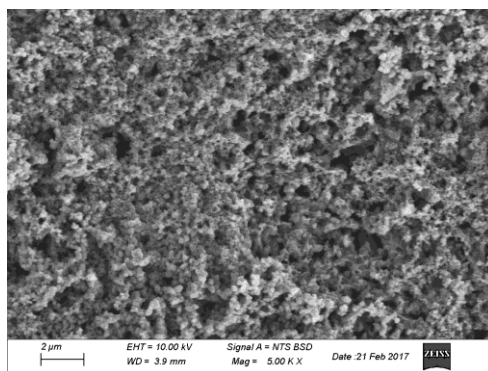


(a)

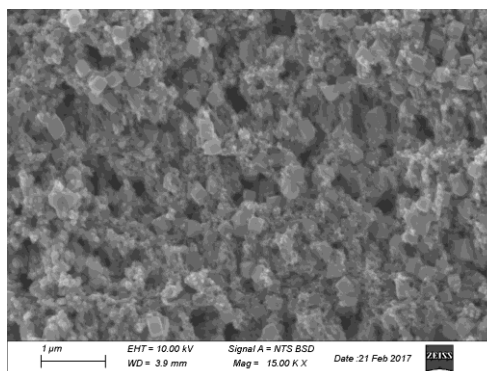


(b)

Figure 4.4 SEM images of MnSe films electrodeposited for 20 min on FTO/Cu<sub>2</sub>O substrate at (a) 5.00 KX and (b) 15.00 KX.



(a)



(b)

Figure 4.5 SEM images of MnSe films electrodeposited for 40 min on FTO/Cu<sub>2</sub>O substrate at (a) 5.00 KX and (b) 15.00 KX.

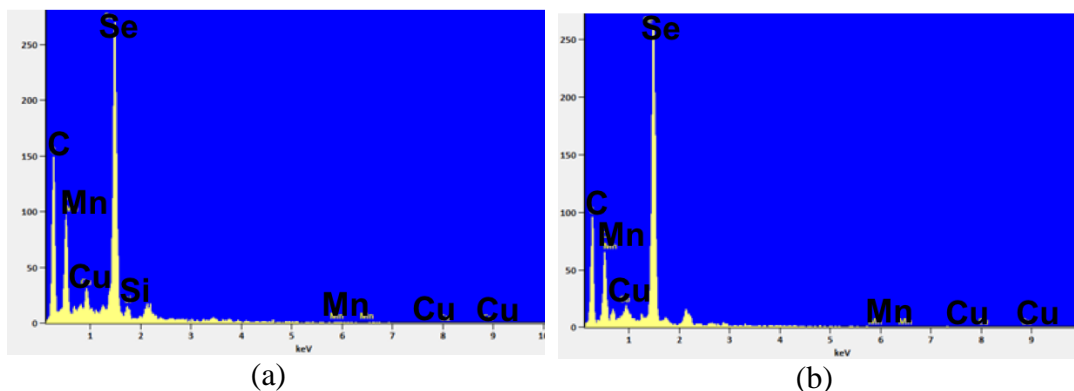


Figure 4.6 Energy dispersive X ray spectra of MnSe films electrodeposited on FTO/Cu<sub>2</sub>O for (a) 20 min and (b) 40 min.

Table 4.2 Se to Mn ratios in electrodeposited MnSe films.

Parameter	Time			
	20 min		40 min	
Element	Se	Mn	Se	Mn
Weight %	35.37	21.4	25.54	44.6
Mass Ratio	1.4	1	1	2.1
Molar Ratio	1	2	1	3

Figures 4.7 and 4.8 provide the linear sweep voltammograms of FTO/Cu<sub>2</sub>O under dark (Figure 4.7a) and under simulated solar light illumination (Figure 4.7b), as compared to that obtained from FTO/Cu<sub>2</sub>O-Co<sub>x</sub>Se-Ni<sub>y</sub>Se (Figure 4.7c), FTO/Cu<sub>2</sub>O-MnSe (Fig 4.8d) and FTO/Cu<sub>2</sub>O/WSe<sub>x</sub> (Figure 4.7d), and under simulated solar irradiation. In addition to a significant positive shift in the onset potential, FTO/Cu<sub>2</sub>O-MnSe produces hydrogen evolution current density at -0.45 V vs Ag/AgCl (3.0 M KCl) that is ~7 time of from FTO/Cu<sub>2</sub>O under simulated solar irradiation is ~10 times higher in the presence of electrodeposited MnSe catalyst when compared to its absence. It is also evident that the MnSe offers the best HER performance amongst the transition metal chalcogenide based

co-catalysts studied. Specifically, current density is  $\sim 3.1$  times of that from FTO/Cu<sub>2</sub>O-Co<sub>x</sub>Se-Ni<sub>y</sub>Se at -0.45 V, and  $\sim 1.4$  times of that from FTO/Cu<sub>2</sub>O-WSe<sub>x</sub> at -0.40 V vs Ag/AgCl (3.0 M KCl). This increase in current density is attributed to increased electron-hole separation by electron capture and catalytic activity for HER (as discussed further in Section 4.3.2). There have been no reports on the use of MnSe as a co-catalyst for solar water reduction as of the date, and the obtained current densities are seen to be higher than or comparable to those reported in a variety of recent literature on the use of Cu<sub>2</sub>O photocathodes for solar water splitting.<sup>137-141</sup> A comparison table (Table 2.2) has been provided in Chapter II. Moreover, this study has been carried out under aqueous conditions in near-neutral pH, which facilitates better practical application as compared with acidic electrolytes used in other reports.

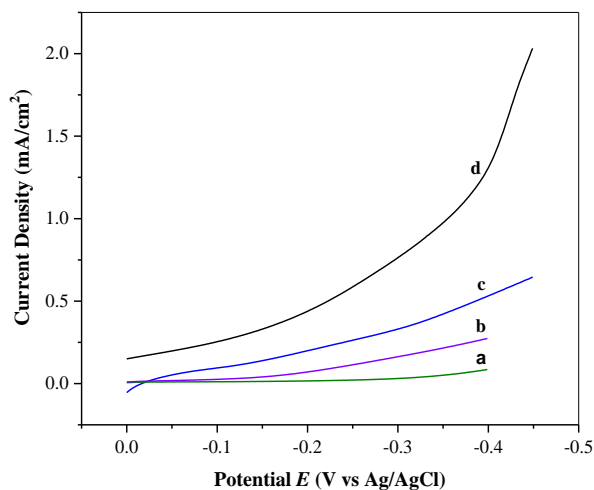


Figure 4.7 Linear sweep voltammogram of (a) FTO/Cu<sub>2</sub>O under dark compared to (b) FTO/Cu<sub>2</sub>O, (c) FTO/Cu<sub>2</sub>O-Co<sub>x</sub>Se-Ni<sub>y</sub>Se, (d) FTO/Cu<sub>2</sub>O-MnSe under simulated solar irradiation.

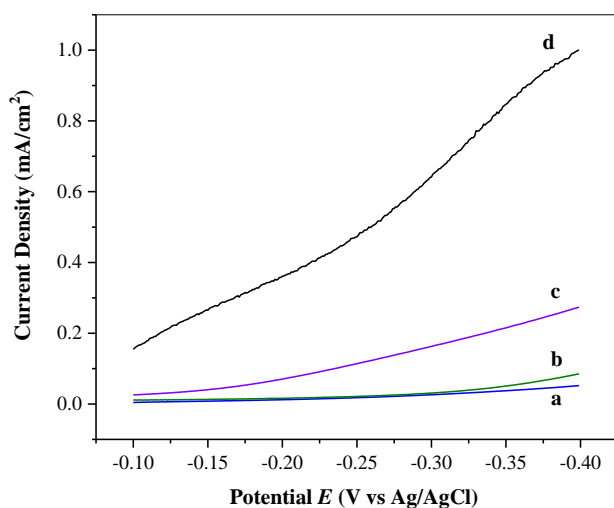


Figure 4.8 Linear sweep voltammogram of (a) FTO/Cu<sub>2</sub>O and (b) FTO/Cu<sub>2</sub>O-WSe<sub>x</sub> under dark, compared to (c) FTO/Cu<sub>2</sub>O and (d) FTO/Cu<sub>2</sub>O-WSe<sub>x</sub> under simulated solar irradiation.

#### 4.3.2 Electrochemical Impedance Spectroscopic (EIS) Studies

As discussed in Section 4.3.1 about photocurrent measurements on transition metal chalcogenide- based photocathodes, it can be clearly seen that FTO-Cu<sub>2</sub>O/MnSe produced the maximum photocurrent of  $\sim 2$  mA/cm<sup>2</sup> at -0.45 V vs Ag/AgCl (Figure 4.7d). Electrochemical impedance spectroscopic (EIS) measurements provide further information on the effect of catalysts in increasing electron-hole separation. Figure 4.9 compares the EIS spectra of FTO/Cu<sub>2</sub>O electrode (Figure 4.9a) and FTO/Cu<sub>2</sub>O-MnSe (Figure 4.9b) under simulated solar irradiation. It can be seen from the figures that the low frequency capacitive impedance in the presence of MnSe is significantly lower in the presence of catalyst than that in its absence. Since the capacitive impedance is inversely proportional to double layer capacitance,<sup>86</sup> it can be deduced that the double layer capacitance is higher with the presence of MnSe catalyst. The increase in double layer capacitance is attributed to increased electron-hole separation at the semiconductor-

electrolyte interface due to electron capture by MnSe for water reduction catalysis. This observation complements measurements from photocurrent measurements, which provided evidence of an increase in photocurrent by a factor of  $\sim 7$  at  $-0.40$  V vs Ag/AgCl upon addition of catalyst as a result of increased electron-hole separation and catalytic activity (Figure 4.7).

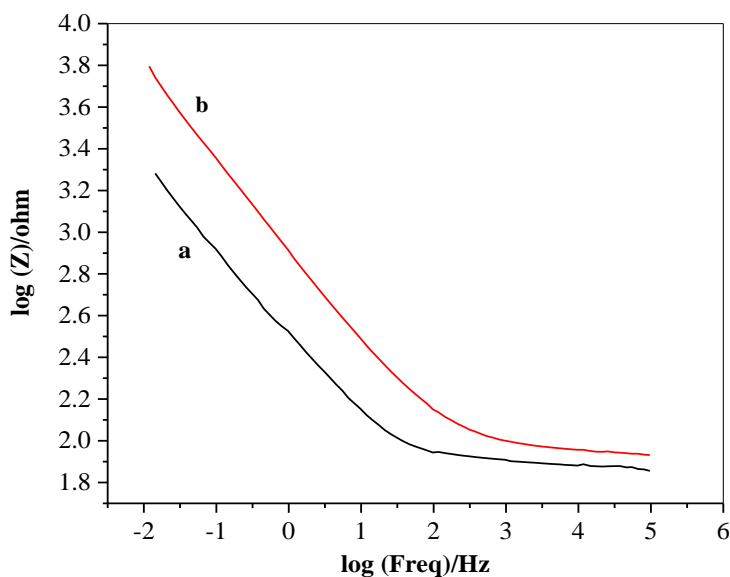


Figure 4.9 Electrochemical impedance spectroscopic plots of (a) FTO/Cu<sub>2</sub>O-MnSe compared to (b) FTO/Cu<sub>2</sub>O under simulated solar irradiation.

#### 4.4 Conclusion

In this chapter, the use of metal chalcogenide based co-catalysts for solar water reduction using electrodeposited Cu<sub>2</sub>O photocathodes has been demonstrated. It was seen from photocurrent measurements and SEM that catalyst deposition time influenced thickness and morphology, and played a role in the overall HER performance. A maximum photocurrent of  $\sim 2$  mA/cm<sup>2</sup> at  $-0.45$  V vs Ag/AgCl was observed from FTO/Cu<sub>2</sub>O-MnSe photocathode of optimized thickness. EIS measurements showed an

increase in space charge capacitance in the presence of the catalyst, as opposed to its absence. This was contributed to the effect of MnSe catalyst in increasing electron-hole separation through electron capture for catalytic activity. Considering there have been no previous studies on the use of MnSe as a co-catalyst for solar water reduction using Cu<sub>2</sub>O photocathodes, this study provides insight the photoelectrochemical behaviour of this system. Due to its excellent activity for HER, FTO/Cu<sub>2</sub>O-MnSe photocathodes can be used in multiple absorber solar water splitting. This will be elaborated further in Chapter VI.

# CHAPTER V - PHOTOELECTROCHEMICAL STUDIES ON TRANSITION METAL PHOSPHIDE AND SELENIDE BASED PHOTOANODES FOR SOLAR WATER OXIDATION

## 5.1 Introduction

The intermittent nature of solar energy and area requirements for grid storage necessitates the development of efficient conversion and storage technologies. Solar to fuel conversion is an effective strategy to convert solar energy directly to chemical fuel.<sup>12, 14, 20, 29</sup> Photoelectrochemical (PEC) water splitting is a safe, localized and room temperature method to utilize solar energy to produce high purity hydrogen and oxygen.<sup>12, 14, 20, 29</sup>

A wide spectrum of research has been carried out in the development of semiconductor based photoelectrodes for PEC water splitting, as well documented in the literature.<sup>12, 20, 23, 26, 29, 90</sup> However, the high energy barrier required for water oxidation (1.23 V vs SHE under standard conditions<sup>29</sup>), in addition to losses from ineffective light absorption and separation of photogenerated electrons and holes pose severe limitations on the ability of single absorber based solar water splitting systems under unbiased or low biased conditions.<sup>34, 90</sup> The prohibitive cost of these noble metal based catalysts necessitates the need for the development of alternate earth abundant non-noble metal based catalysts for efficient solar to hydrogen conversion by water splitting.<sup>2, 34, 91</sup>

In recent years, heterogeneous catalysts based on transition metal phosphides,<sup>72, 74-77</sup> selenide,<sup>69-72</sup> and sulphides have been considered as bifunctional catalysts for water splitting. Initial studies on Fe,<sup>71</sup> Co,<sup>70</sup> and Ni<sup>69, 72</sup> selenide based materials have indicated efficient catalytic performance for OER. The addition of electronegative Se<sup>2-</sup> ligands in

the vicinity of catalytically active metal sites could result in accelerated delivery of dioxygen molecules due to *3d-2p* repulsions and negative charge localized on Se sites.<sup>71-</sup>

72, 78

A majority of metal phosphides<sup>74</sup> have properties comparable to metals and ceramics. They possess excellent heat and electrical conductivity, in addition to being thermally and chemically stable. Transition metal phosphides have been reported to have activity for electrocatalytic water oxidation.<sup>72, 75</sup> They can be oxidized to higher valences and transformed into metal oxides/hydroxides in the OER environment. A few studies in literature have attributed the high oxidation ability of transition metal phosphides to the formation of a core-shell structure (oxide@metal phosphide).<sup>80-81</sup>

The use of transition metal selenides and phosphides as co-catalysts for photoelectrochemical water oxidation are limited in literature as of current writing. In this chapter, two of the best performing photoanodes based on transition metal phosphide and selenide based co-catalysts viz. FTO/Fe<sub>2</sub>O<sub>3</sub>-FeSe and FTO/BiVO<sub>4</sub>-Co<sub>x</sub>P will be discussed in detail with emphasis on photoelectrochemical studies to determine the role of catalyst in increasing the activity of solar water oxidation.

## **5.2 Materials and Methods**

### **5.2.1 Materials**

Bismuth nitrate pentahydrate (analytical reagent) and sodium acetate (99%) were obtained from Mallinckrodt and Matheson Coleman and Bell, respectively. Vanadyl sulphate hydrate (99.9%) and sodium selenite (99.75%) were obtained from Alfa Aesar. Iron (II) sulphate heptahydrate (99%), cobalt chloride hexahydrate (ACS reagent) and sodium hypophosphite (99%) were obtained from Aldrich. Deionized water produced



using a Millipore Advantage 5 system was used as a solvent for preparing all aqueous solutions.

### 5.2.2 Preparation of Photoanodes

Fe<sub>2</sub>O<sub>3</sub> photoanodes were prepared by potentiostatic electrodeposition.<sup>156</sup> The working electrode consisted of 1 cm<sup>2</sup> FTO, which was cleaned by sonication in deionized water, acetone, isopropanol and deionized water, each for 15 min, respectively. Ag/AgCl (3.0 M KCl) and a Pt wire were used as the reference and counter electrodes. The solution was purged with nitrogen gas for 15 min to prevent competitive oxygen reduction, and the deposition was carried out at -1.0 V vs Ag/AgCl (3.0 M KCl) for 10 min in a bath consisting of 10.0 mM FeSO<sub>4</sub> at pH 10.5 (adjusted with NaOH). The orange colored as-deposited films were annealed in air at 773 K for 2 h to produce the yellow-orange FTO/Fe<sub>2</sub>O<sub>3</sub> electrode for study. The FeSe catalyst was deposited<sup>157</sup> on FTO/Fe<sub>2</sub>O<sub>3</sub> by electrodes by electrodeposition at -0.90 V vs Ag/AgCl in a bath consisting of 10.0 mM FeSO<sub>4</sub> and 10.0 mM Na<sub>2</sub>SeO<sub>3</sub> to produce the FTO/Fe<sub>2</sub>O<sub>3</sub>-FeSe photoanode. Catalyst thickness was controlled by altering the deposition time.

BiVO<sub>4</sub> films were electrodeposited<sup>99</sup> on clean 1 cm<sup>2</sup> FTO electrodes at 1.90 V vs Ag/AgCl in a bath consisting of 35.0 mM Bi(NO<sub>3</sub>)<sub>3</sub> and 10.0 mM VOSO<sub>4</sub> (pH adjusted to 5.0 with HNO<sub>3</sub>) for 10 min without stirring. Pt and Ag/AgCl (3.0 M KCl) were used as the counter and reference electrodes during the deposition. The electrodeposited films were then annealed at 673 K for 2 h to prepare the light-yellow FTO/BiVO<sub>4</sub> photoanode. Co<sub>x</sub>P water oxidation catalyst films<sup>158</sup> of controlled thicknesses were coated on the BiVO<sub>4</sub> photoanode by consecutive linear scans between -0.30 and -0.90 V vs Ag/AgCl

(3.0 M KCl) at 0.005 V/s in a deposition bath containing 50.0 mM CoCl<sub>2</sub>, 0.50 M NaH<sub>2</sub>PO<sub>2</sub> and 0.10 M CH<sub>3</sub>COONa.

Figures 5.1a and 5.1b are the UV-vis spectra plots of FTO/Fe<sub>2</sub>O<sub>3</sub> and FTO/BiVO<sub>4</sub> photoanodes, respectively. It can be seen that both the photoanodes absorb light in the visible region. An absorption edge at 575 nm (Figure 5.1a) corresponds to an approximate band gap of 2.15 eV in FTO/Fe<sub>2</sub>O<sub>3</sub>, whereas FTO/BiVO<sub>4</sub> had an adsorption band at 545 nm (Figure 5.1b) corresponding to a band gap of 2.27 eV.

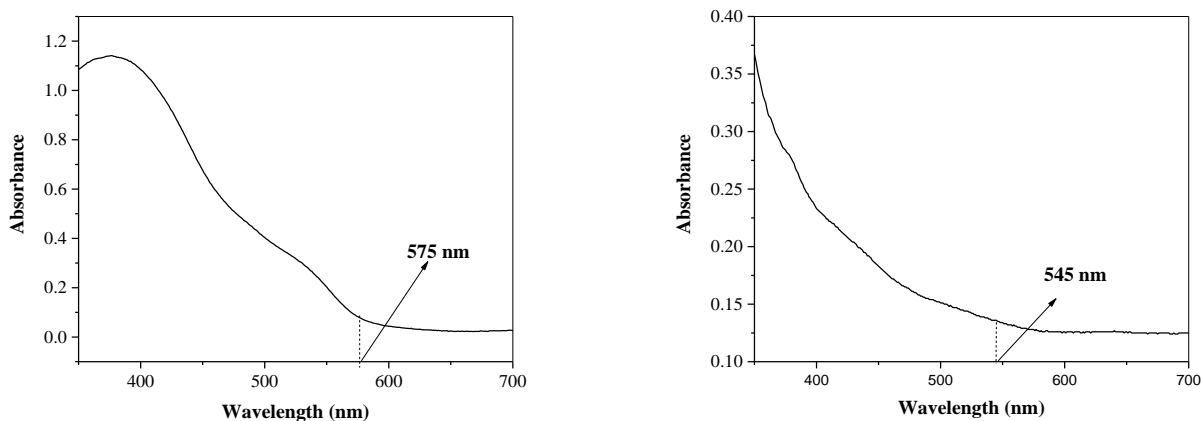


Figure 5.1 UV-vis spectra of (a) FTO/Fe<sub>2</sub>O<sub>3</sub> and (b) FTO/BiVO<sub>4</sub> photoanodes (Blanked with FTO).

### 5.2.3 Physico-chemical Characterization

Scanning electron microscopic (SEM) images of FTO/BiVO<sub>4</sub>-Co<sub>x</sub>P electrodes on FTO substrate were obtained with a Zeiss Sigma VP FEG SEM. An Evolution 300 Thermo-Scientific spectrophotometer was used to obtain the UV-vis spectrum of photoelectrodes, with FTO substrate used as blank.

## 5.2.4 Photoelectrochemical Studies

PEC measurements were carried out in a three-electrode electrochemical setup using a 50 mL quartz beaker as the cell, an Ag/AgCl (3.0 M KCl) as the reference electrode, a Pt wire as the counter electrode, and 1 cm<sup>2</sup> FTO/M (where M=Fe<sub>2</sub>O<sub>3</sub>-FeSe and BiVO<sub>4</sub>-Co<sub>x</sub>P) as the working electrode, respectively. A 0.050 M pH 9.0 borate buffer solution was used as the electrolyte for all experiments with or without the presence of catalyst M of different thicknesses. Electrochemical impedance spectroscopic (EIS) measurements were carried out under open circuit potential with a 5.0 mV AC signal super-imposed. Mott Schottky plots were obtained at a frequency of 962 Hz. An electrochemical workstation (CH instruments, Model 660 A) was used to conduct electrochemical experiments. Simulated solar light for PEC studies was provided by a 150 W Xe lamp solar simulator (ABET technologies) with an AM 1.5 G filter providing a light intensity of 1000 W/m<sup>2</sup> (1 sun). Figure 5.2 provides a representative cell scheme for photoelectrochemical water splitting using FTO/BiVO<sub>4</sub>-Co<sub>x</sub>P photoanodes.

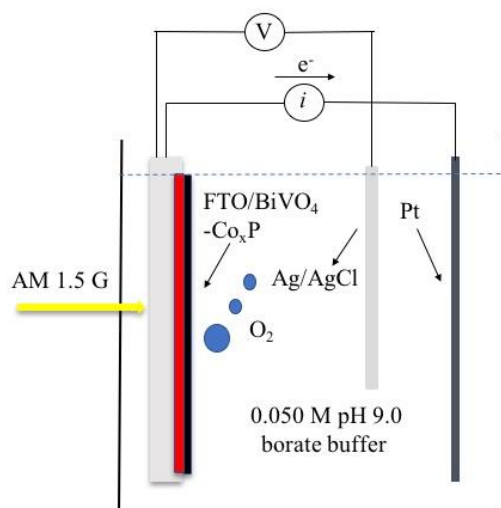


Figure 5.2 Representative cell scheme for photoelectrochemical water splitting using FTO/BiVO<sub>4</sub>-Co<sub>x</sub>P photoanodes.

## 5.3 Results and Discussion

### 5.3.1 Photocurrent Measurements

Photocurrent measurements were carried out for the purpose of evaluating overall photoanode and catalyst performance. They also provide an understanding of the role of catalyst in increasing electron-hole separation by hole capture for catalytic activity.

Figures 5.3 and 5.4 are the plots of catalyst deposition time vs maximum photocurrent for FTO/Fe<sub>2</sub>O<sub>3</sub>-FeSe and FTO/BiVO<sub>4</sub>-Co<sub>x</sub>P respectively.

It can be seen that the photocurrent increases with deposition time up to certain maximum values, which is -0.27 mA/cm<sup>2</sup> and -0.67 mA/cm<sup>2</sup> for FTO/Fe<sub>2</sub>O<sub>3</sub>-FeSe (Figure 5.3) and FTO/BiVO<sub>4</sub>-Co<sub>x</sub>P (Figure 5.4) photoanodes respectively. Beyond this point, the photocurrent decreases. The decrease in photocurrent could be attributed to increase in overall resistance caused by increase in film thickness, as well as increased distance for charge transport which could result in electron-hole recombination.

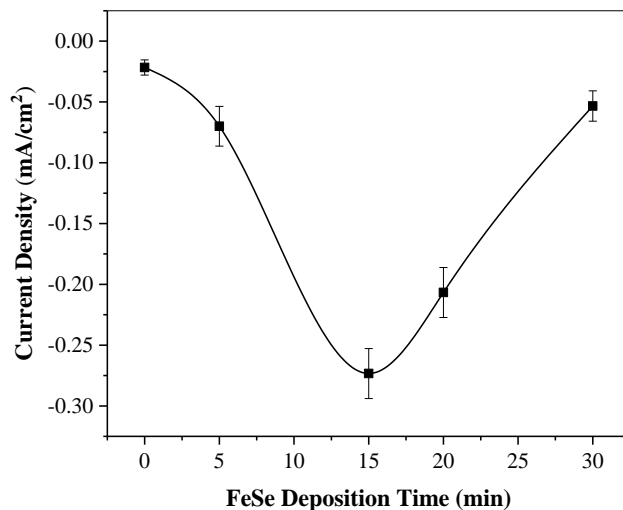


Figure 5.3 Catalyst deposition time (thickness) vs current density for FTO/Fe<sub>2</sub>O<sub>3</sub>-FeSe photoanodes at 0.70 V vs Ag/AgCl.

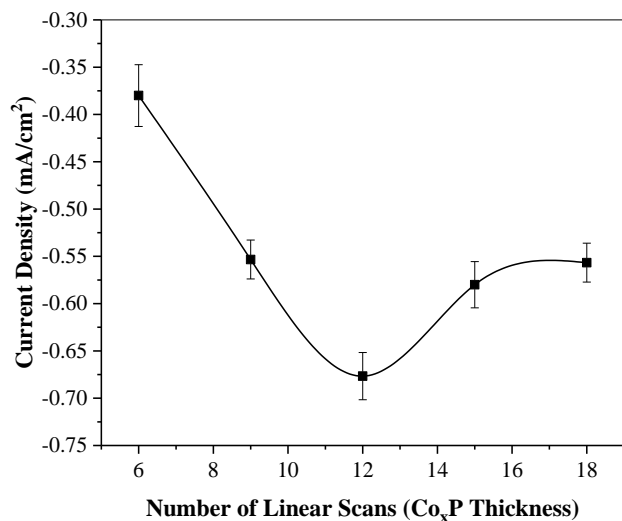


Figure 5.4 Catalyst deposition linear scans (thickness) vs current density for FTO/BiVO<sub>4</sub>-Co<sub>x</sub>P photoanodes at 0.70 V vs Ag/AgCl.

The linear sweep voltammogram for FTO/Fe<sub>2</sub>O<sub>3</sub> photoanodes in the presence and absence of electrodeposited FeSe catalyst is given in the Figure 5.5. Under simulated solar light illumination (Figures 5.5a and b), a maximum photocurrent density of -0.27 mA/cm<sup>2</sup> was observed at 0.70 V vs Ag/AgCl in the presence of FeSe catalyst (Figure 5.5a), which is significantly larger than that obtained from FTO/Fe<sub>2</sub>O<sub>3</sub> photoanodes (Figure 5.5b). Under dark conditions (Figures 5.5c and d), the overall current density is negligible, although the dark current in the presence of FeSe is marginally higher than its absence due to electrocatalytic activity for OER.

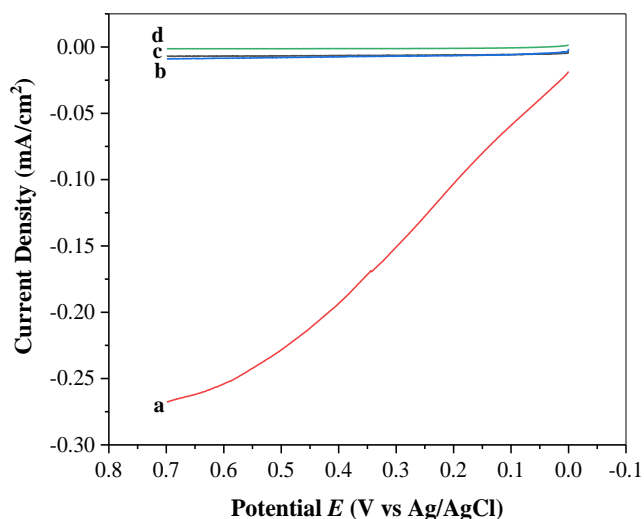


Figure 5.5 Linear sweep voltammograms of FTO/Fe<sub>2</sub>O<sub>3</sub> photoanodes in the (a) presence and (b) absence of FeSe under simulated solar radiation, as compared to those in the (c) presence (d) absence of FeSe under dark conditions. See Section 5.2.4 for experimental conditions

In the case of FTO/BiVO<sub>4</sub>-Co<sub>x</sub>P photoanodes, the comparative linear sweep voltammograms are provided in Figures 5.6A (under dark) and 5.6B (under simulated solar illumination). The electrocatalytic activity of Co<sub>x</sub>P is clearly evident in Figure 5.6A, which compares the OER performance of BiVO<sub>4</sub> photoanodes in the presence (Figure 5.6A(a)) and absence (Figure 5.6A(b)) of catalyst under dark. It can be seen that the OER onset potential under dark conditions shifts by ~0.15 V vs Ag/AgCl in the negative direction in the presence of electrodeposited Co<sub>x</sub>P. Under simulated solar irradiation, a maximum current density of -0.67 mA/cm<sup>2</sup> can be observed in the presence of Co<sub>x</sub>P at 0.70 V vs Ag/AgCl (Figure 5.6B(a)), which is ~3.5 times greater than that in its absence (Figure 5.6B(b)).

The increase in photocurrents in the presence of catalyst can be attributed to increased electron-hole separation through hole capture by the catalyst for catalytic

activity. This is explained further in terms of space charge capacitance and overall charge carrier concentration in the next Section.

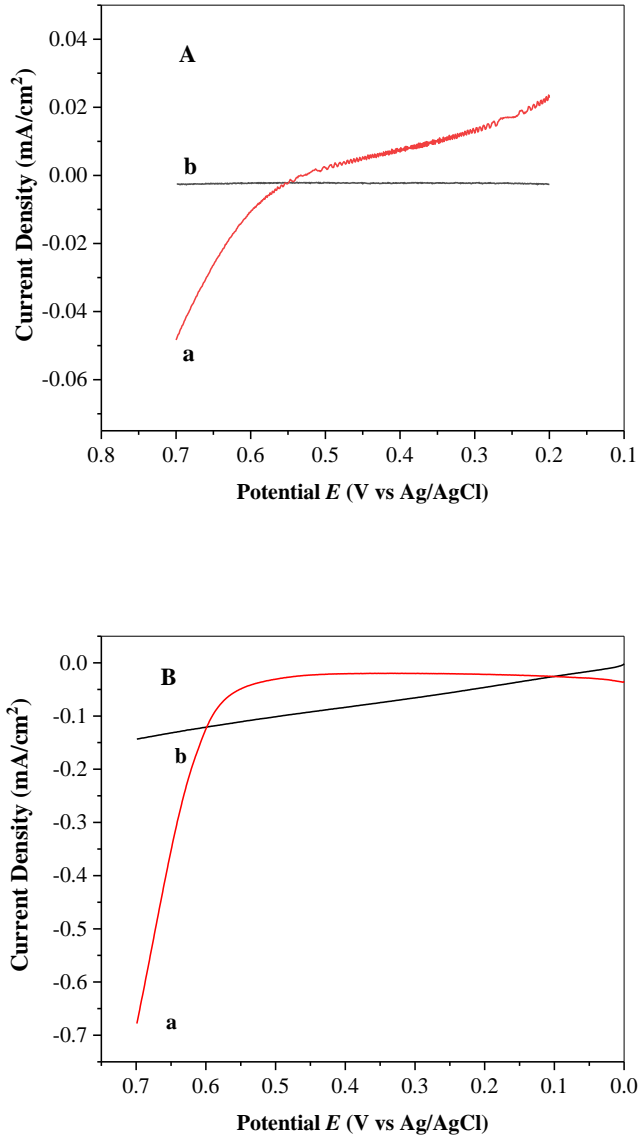


Figure 5.6 (A) Linear sweep voltammograms of FTO/BiVO<sub>4</sub> photoanodes in the(a) presence of and (b) absence of Co<sub>x</sub>P under dark conditions. (B) Linear sweep voltammograms of FTO/BiVO<sub>4</sub> photoanodes in the (a) presence and (b) absence of Co<sub>x</sub>P under simulated solar irradiation.

### 5.3.2 Electrochemical Impedance Spectroscopy and Mott Schottky Plots

Electrochemical impedance spectroscopic (EIS) measurements were conducted to further correlate the results from photocurrent studies which point at the effect of catalyst in increasing electron hole separation through hole capture and catalytic activity. Figures 5.7a and 5.7b are the EIS spectra (Bode plots) obtained from FTO/Fe<sub>2</sub>O<sub>3</sub> photoanodes under simulated solar irradiation conditions in the presence and absence of electrodeposited solid-state water oxidation catalyst FeSe. It can be seen from the figure that the low frequency capacitive impedance in the presence of catalyst is significantly lower than in its absence, indicating a higher double layer capacitance with electrodeposited FeSe catalyst. This observation indicates the role of FeSe in rendering increased electron-hole separation through hole capture and catalytic activity, and complements data from photocurrent measurements which clearly elucidate the increased photocurrent density in the presence of FeSe.

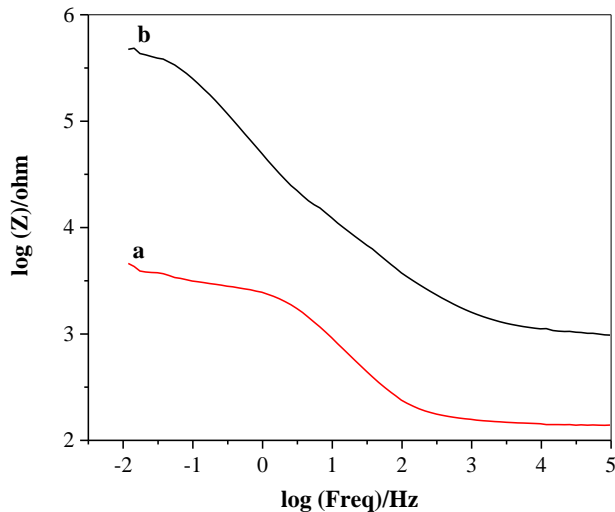


Figure 5.7 Electrochemical Impedance spectra of FTO/FeSe photoanodes in the (a) presence and (b) absence of FeSe under simulated solar irradiation.



As noted in Section 5.3.1, it can be seen that FTO/BiVO<sub>4</sub>-Co<sub>x</sub>P photoanodes produced a maximum photocurrent density of -0.67 mA/cm<sup>2</sup> at 0.70 V vs Ag/AgCl, which is higher than that from the FTO/Fe<sub>2</sub>O<sub>3</sub>-FeSe photoanode by a factor of 2.5. Mott Schottky analysis (Figure 5.8) is an EIS based technique which provides data on the relationship between applied potential and space charge frequencies to compare the overall charge carrier density in the presence and absence of catalyst.

It can be seen from the Figure 5.8 that the slope of the Mott Schottky plot in the presence of Co<sub>x</sub>P catalyst ( $1.66 \times 10^{10}$ ) is lower than that in its absence ( $5 \times 10^{10}$ ). The positive slope of the Mott Schottky plot indicates n-type semi-conductivity, which is suitable for photoanodes. Using the obtained Mott Schottky slopes, 1 cm<sup>2</sup> electrode area, and relative permittivity  $\xi_r = 10$ , the values of  $N_D$  (Eq. 3.1) in the absence and presence of catalyst were calculated to be  $2.82 \times 10^{20}$  and  $8.49 \times 10^{20}$  respectively. It can also be seen from the extrapolated x intercepts of the Mott Schottky plot that a more negative flat band potential can be expected in the presence of the catalyst due to increased electron-hole separation at the semiconductor electrolyte interface. The higher value of charge-carrier concentration in the presence of Co<sub>x</sub>P can be attributed to increased electron-hole separation resulting from hole capture in the presence of the catalyst, and this observation complements data obtained from photocurrent measurements on FTO/BiVO<sub>4</sub>-Co<sub>x</sub>P (Figure 5.8).

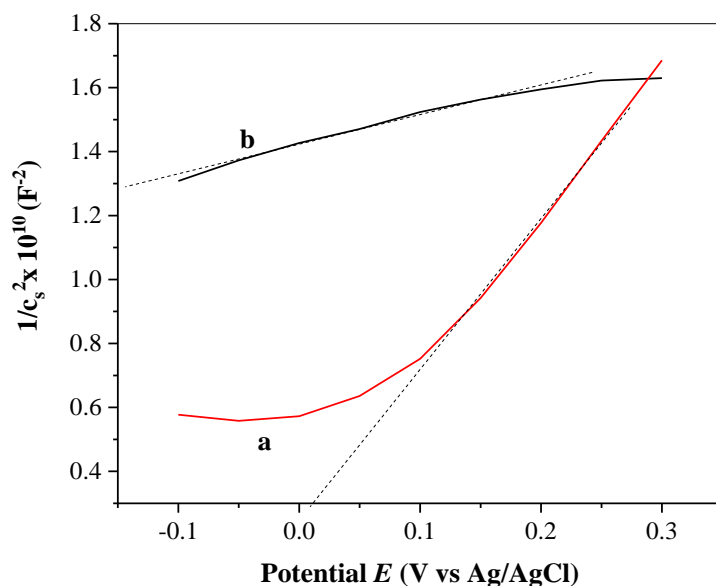


Figure 5.8 Mott Schottky plots of FTO/BiVO<sub>4</sub> photoanodes in the (a) absence of and (b) presence of Co<sub>x</sub>P under simulated solar irradiation.

It is evident from comparing the photocurrent measurements (Figure 5.5 vs 5.6) that the maximum water oxidation performance was observed from FTO/BiVO<sub>4</sub>-Co<sub>x</sub>P photoanodes. Hence, the surface morphology, dissolved oxygen measurements and stability measurements in this system are provided below to explain the OER performance and limits in further detail.

### 5.3.3 Surface Morphology of FTO/BiVO<sub>4</sub>-Co<sub>x</sub>P Photoanodes

Scanning electron microscopy (SEM) was used to study the surface morphology of FTO/BiVO<sub>4</sub>-Co<sub>x</sub>P photoanodes deposited with 12 linear scans (see Section 5.2.2). Figures 5.9a and 5.9b are the SEM images of FTO/BiVO<sub>4</sub>-Co<sub>x</sub>P photoanodes at 4 KX and 10X magnification respectively. An evenly distributed layer of microspheres is observed, with the catalyst particle size ranging from approximately 1 to 2 μm. Figure 5.10 is the EDX spectrum of FTO/BiVO<sub>4</sub>-Co<sub>x</sub>P, depicting the characteristic peaks for Bi, V, O, Sn,

Co, and P. Approximate weight percentages of Co and P were 8.50% and 0.78% respectively, corresponding to an estimate Co to P molar ratio of 6:1. This is based on the ability of the EDX detector to sense local elements and the relative distribution of  $\text{BiVO}_4$  and  $\text{SnO}_2$ , which provides an approximate estimation on the possible compositional nature of the catalyst.

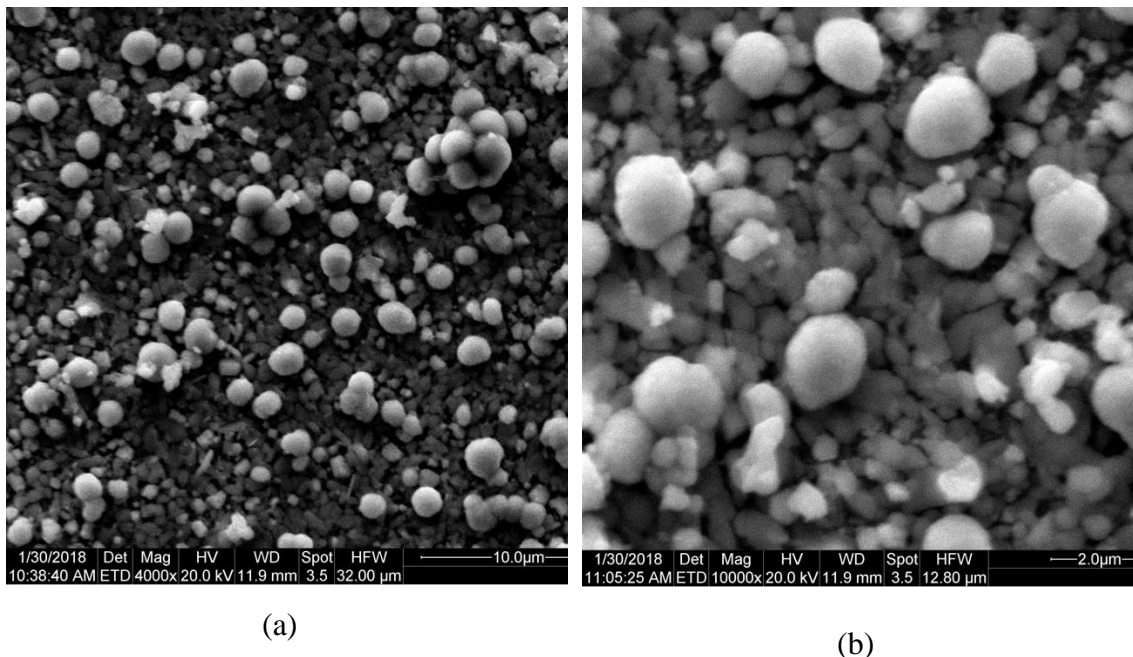


Figure 5.9 SEM images of FTO/ $\text{BiVO}_4$ - $\text{Co}_x\text{P}$  photoanodes at (a) 4KX and (b) 10 KX.

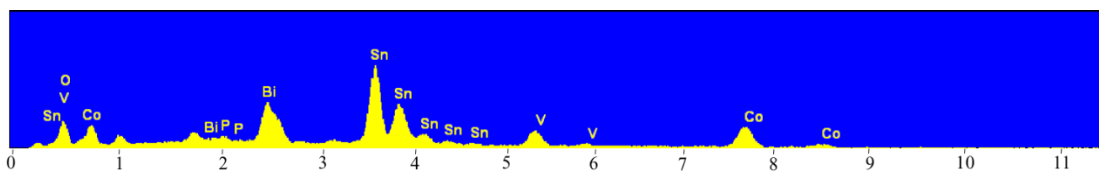


Figure 5.10 EDX spectrum of FTO/ $\text{BiVO}_4$ - $\text{Co}_x\text{P}$  photoanode.

### 5.3.4 Dissolved Oxygen Measurements

Dissolved oxygen (DO) measurements were performed using three-electrode multi-potential step voltammetric experiment. The applied bias was alternatively swept between 0 and 1.10 V over 3 second intervals. A Clark electrode type dissolved oxygen

sensor was used for the measurements, and the electrochemical cell was degassed with  $N_2$  gas for a period of 15 min prior to measurements. During the actual tests, a nitrogen gas blanket was placed in the cell headspace. Figures 5.11a and b are comparative DO measurements in ppm from FTO/ $BiVO_4$  and FTO/ $BiVO_4-Co_xP$  photoanodes under simulated solar irradiation. It can be clearly seen that the maximum oxygen produced in the presence of catalyst is  $\sim 2.75$  times higher than in its absence at 200 s. The average Faradaic efficiencies for  $BiVO_4$  photoelectrodes in the presence and absence of catalyst were estimated to be 210.5% and 190% respectively. Dispersion of local DO concentrations relative to the sensor could have led to potential over-estimation of obtained values and the Faradaic efficiencies calculated, but the overall trends in DO confirm results from photocurrent and Mott Schottky plots on the role of  $Co_xP$  in enhancing OER performance.

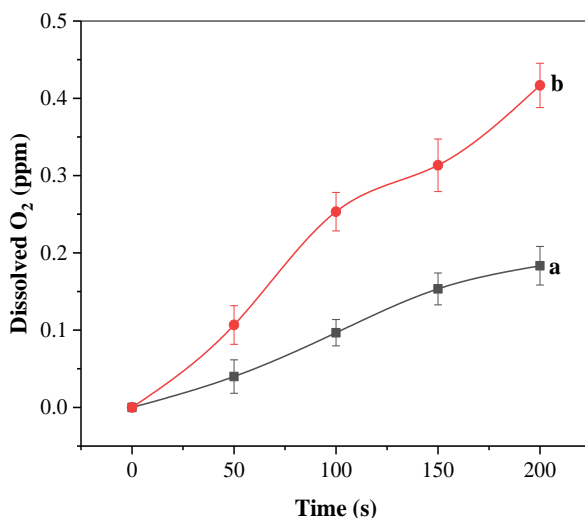
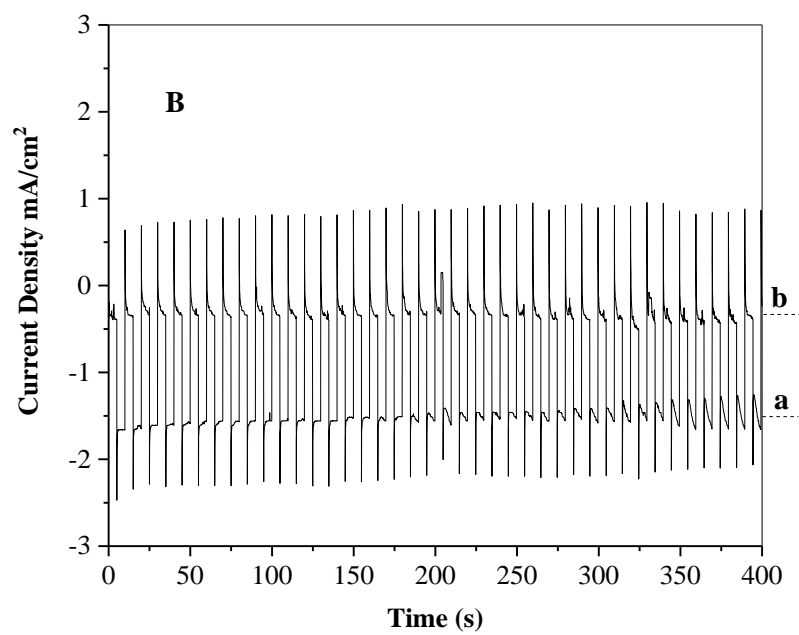
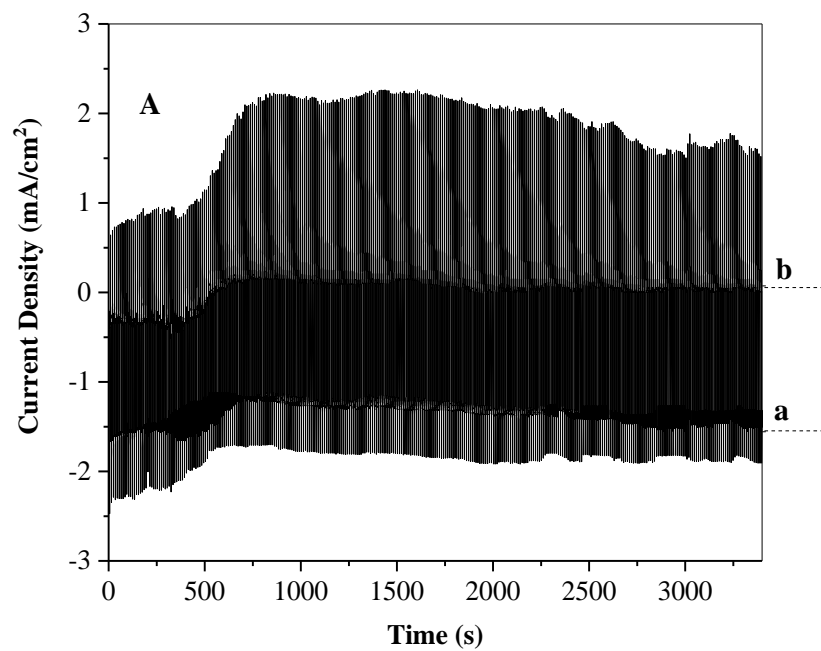


Figure 5.11 Dissolved oxygen measurements FTO/ $BiVO_4$  photoanodes in the (a) absence and (b) presence of  $Co_xP$  under simulated solar irradiation.

### 5.3.5 Stability Studies

The stability of FTO/BiVO<sub>4</sub> electrodes for photoelectrochemical water oxidation in the presence of Co<sub>x</sub>P was evaluated by multiple-potential step and constant potential experiments using a typical three-electrode system. The applied potential was regularly shifted from 0 to 1.10 V vs Ag/AgCl in 5 s intervals for a time period of 3400 s, and responses of photocurrent were recorded. Figures 5.12 (A), (B) and (C) are the plots of photocurrent density vs time from a FTO/BiVO<sub>4</sub> electrode under multi-potential step excitations in across the full range, 0-400 s, and 3000-3400 s, respectively. The pattern of spikes in the observed data is due to the blocking and release of oxygen gas on the electrode surface during the oxidation process. Comparing the data between Figure 5.12 (B) and 5.12 (C), the overall change in water oxidation current density at 1.10 V vs Ag/AgCl is relatively small (~0.1 mA/cm<sup>2</sup> or -6.2%). No loss of catalyst coating was visibly observed at the end of the experiment. Considering these observations and the operating potential range, FTO/BiVO<sub>4</sub>-Co<sub>x</sub>P can be used as a stable photoanode for water oxidation.



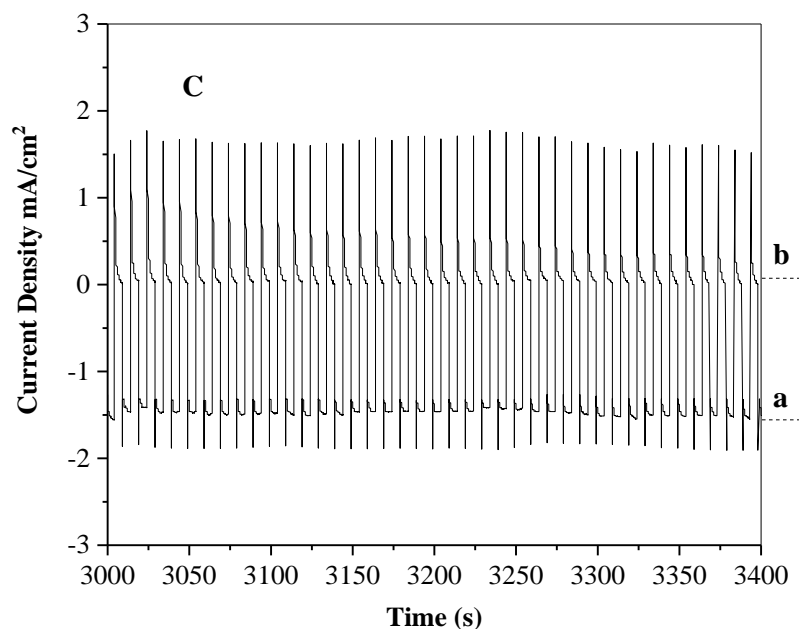


Figure 5.12 Stability studies of FTO/BiVO<sub>4</sub>-Co<sub>x</sub>P photoanodes under simulated solar light for the time region of (A) 0-3400 s, (b) 0-400 s, and (c) 3000-3400 s. Potentials applied at a: 1.10 V vs Ag/AgCl and b: 0 V vs Ag/AgCl.

## 5.4 Conclusion

In this chapter, two photoanodes viz FTO/Fe<sub>2</sub>O<sub>3</sub>-FeSe and FTO/BiVO<sub>4</sub>-Co<sub>x</sub>P based on metal chalcogenide co-catalysts have been reported for PEC water oxidation. Photocurrent measurements on optimized photoelectrodes showed increased OER current densities due to catalytic activity and increased charge separation<sup>123</sup>. Impedance spectroscopic studies and Mott Schottky plots indicated the effect of co-catalysts in increasing electron-hole separation and overall charge carrier density. This trend was reflected in dissolved oxygen measurements, which provided definitive evidence of increased oxygen evolution in the presence of Co<sub>x</sub>P co-catalyst. A few further

experiments have been performed on the use of these photoanodes towards tandem solar water splitting, and are depicted in the next chapter.



## CHAPTER VI – PHOTOELECTROCHEMICAL STUDIES ON TANDEM SOLAR WATER SPLITTING

### 6.1 Introduction

Photoelectrochemistry combines the abundance of solar energy with the low temperature, controlled and localized nature of electrochemical process design, offering an effective platform for the production of hydrogen from water, which is one of the earth's most abundant natural resources. Photoelectrochemical (PEC) water splitting is a versatile strategy for the direct solar to hydrogen conversion at room temperature.<sup>12</sup>

In typical solar water splitting systems, a single semiconductor light absorber i.e. a photoanode or a photocathode absorbs photons to produce electron-hole pairs that split water. A variety of n-type and p-type semiconductor photoelectrodes,<sup>12, 20, 23, 26, 29, 90</sup> such as TiO<sub>2</sub>,<sup>110, 112, 159</sup> BiVO<sub>4</sub>,<sup>99</sup> and p-Cu<sub>2</sub>O<sup>119-122</sup> have been reported. However, as described in Section 1.2.3.2 of the introduction (Chapter I), the use of a single light absorber for solar water splitting limits solar energy utilization and results in lower overall solar to hydrogen conversion (%STH) efficiencies.<sup>31</sup> In addition, there is a trade-off between semiconductor materials that possess valance and conduction band edges matching HER/OER potentials and bandgap/stability.

The use of multiple light absorbers can increase overall solar energy utilization and in addition provide a solution to the trade-off between overall band gap and band edge positioning specific to solar water oxidation and water reduction. In a typical dual absorber 4 photon (D4) cell,<sup>32</sup> two light absorbing semiconductors absorb a total of four photons to produce four electron hole pairs required to split one molecule of water.

Considering these factors, multiple absorber based photoelectrochemical cells can provide more efficient overall water splitting performance.

Co-catalysts currently used for photoelectrochemical water splitting in tandem cells have primarily been based on noble metals such as Pt and Ru.<sup>40-41</sup> However, the high cost of these materials necessitates studies on earth abundant and non-noble metal<sup>2, 34-35, 91</sup> based HER and OER catalysts. In previous chapters, photoelectrochemical studies on transition metal polyoxometalates in solution and solid-state co-catalysts based on metal chalcogenides have been described. This chapter focuses on their water splitting performance in dual absorber configurations.

Due to high cost and presence of indirect band gaps in crystalline Si, it cannot be used efficiently in flexible and light weight photovoltaics. A few recent studies have focused on amorphous Si triple junction (3 jn Si) based materials for photovoltaic<sup>160</sup> and photoelectrochemical<sup>39</sup> applications. This configuration can greatly enhance solar energy utilization owing to the presence of three distinct p-n junctions and result in progressive absorption of different wavelengths of light.<sup>160</sup> They could be combined with HER photocathodes and can serve as an alternative to metal oxide photoanodes in multiple-absorber based. In this chapter, two-electrode with zero bias photocurrent measurements will be performed to study the overall water splitting performance of dual absorber cells based on co-catalysts and photoelectrodes discussed in previous chapters. Dual absorber configurations based on metal oxide photoanode/photocathode and 3jn Si photoanode/photocathode with non-noble metal based co-catalysts were studied to compare the difference between overall photocurrents and in single absorber and tandem cell based systems. Reports on multiple absorber cells based entirely on non noble metal

based co-catalysts are limited in literature. These studies highlight the best performing systems based on co-catalysts discussed in this dissertation, and would offer initial insights into further research towards the development of non-noble metal based water splitting cells.

## **6.2 Materials and Methods**

### **6.2.1 Materials**

Materials used for the preparation of catalysts and photoelectrodes have been listed in previous chapters. Deionized water produced from Millipore Advantage 5 system was used when preparing all aqueous solutions. Triple junction a-Si solar cells on stainless steel substrates were obtained from Xunlight Corp. (Toledo, OH).

### **6.2.2 Preparation of Photoelectrodes**

Previous sections have described the procedures for preparation of FTO/Cu<sub>2</sub>O (Section 4.2.2) FTO/Cu<sub>2</sub>O-MnSe (Section 4.2.2), FTO/Cu<sub>2</sub>O-WSe<sub>x</sub> (Section 4.2.2), FTO/Cu<sub>2</sub>O-Co<sub>x</sub>Se-Ni<sub>y</sub>Se (Section 4.2.2), FTO/Cu<sub>x</sub>Se (Section 3.2.2), FTO/TiO<sub>2</sub> (Section 2.2.2), FTO/BiVO<sub>4</sub> (Section 5.2.2), FTO/BiVO<sub>4</sub>-Co<sub>x</sub>P (Section 5.2.2), FTO/Fe<sub>2</sub>O<sub>3</sub> (Section 5.2.2), FTO/Fe<sub>2</sub>O<sub>3</sub>-FeSe (Section 5.2.2), Ni<sub>5</sub>-POM (Section 2.2.2) and Co<sub>9</sub>-POM (Section 3.2.2).

### **6.2.3 Photoelectrochemical Measurements**

Photoelectrochemical studies to measure overall water splitting were conducted in a two electrode setup in a 50 mL quartz beaker with an electrochemical workstation (CH Instruments, model 660A). The working electrode lead was connected to the photoanode, and the reference/counter electrode leads were connected to Pt wire (for single photo-absorber) or the photocathode (for multiple-absorber cells). Though the term “tandem

cells” has been used interchangeably for multiple absorber configurations, our mode of cell design for current studies does not follow a typical stacked photoelectrode approach. In the case of multiple absorber systems for this chapter, the photoanode (or 3 jn Si) and photocathode were placed in a side by side configuration across the illuminated area. Compared to a stacked photoanode/photocathode cell, this is a simplified design and helps reduce light absorption losses during transmission and blocking of incident light by heterogeneous water oxidation and reduction co-catalysts. This is especially relevant in the case of configurations based on 3 jn Si coupled with heterogeneous co-catalyst based HER photocathodes presented in this study, where it would not be possible to transmit light if it was used as the front electrode in a stacked configuration. Oxygen measurements were conducted using a dissolved oxygen sensor (Hanna Instruments, Model HI9164). Experiments were performed at a scan rate of 0.020 V/s in a 0.050 M pH 9.0 borate buffer electrolyte. Unless otherwise mentioned, the Co<sub>9</sub>-POM and Ni<sub>5</sub>-POM concentrations in solution were 20 μM whenever they were used for tests in this chapter. All electrodes used had an exposed area of 1 cm<sup>2</sup>.

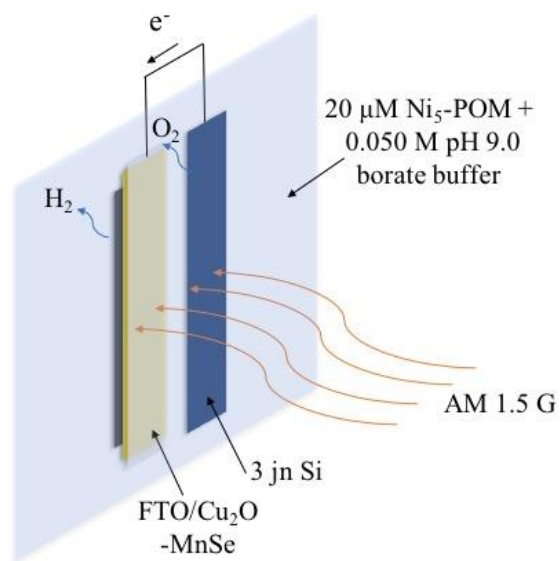


Figure 6.1 Representative scheme for solar water splitting using 3jn Si/Ni<sub>5</sub>-POM [photoanode]:FTO/Cu<sub>2</sub>O-MnSe [photocathode] water splitting cell.

## 6.3 Results and Discussion

### 6.3.1 Photocurrent Measurements

Overall photocurrent studies for single absorber and tandem cells were performed using two electrode measurements. Since the overall objective of tandem cells is to produce water splitting photocurrents at zero applied bias, measurements of zero bias photocurrents would be an effective method to compare various single absorber and tandem solar water splitting systems (Table. 6.1).

Table 6.1 Comparison of zero bias photocurrents of single absorber and tandem water splitting systems (conditions in Section 6.2.3).

<b>Photoanode</b>	<b>Photocathode</b>	<b>Zero Bias Photocurrent (mA/cm<sup>2</sup>)</b>
3jn Si	Pt (single absorber)	-0.06
3jn Si	Pt (single absorber)- Co <sub>9</sub> -POM	-0.09
3jn Si	FTO/Cu <sub>2</sub> O	-0.08
3jn Si	FTO/Cu <sub>2</sub> O-Co <sub>9</sub> -POM	-0.14
3jn Si	FTO/Cu <sub>2</sub> O-Co <sub>x</sub> Se-Ni <sub>y</sub> Se	-0.11
3jn Si	FTO/Cu <sub>x</sub> Se-Co <sub>9</sub> -POM	-0.60
3 jn Si	FTO/Cu <sub>2</sub> O-MnSe	-0.37
3jn Si	FTO/Cu <sub>2</sub> O-WSe <sub>x</sub>	-0.18
3jn Si-Ni <sub>5</sub> -POM	Pt (Single absorber)	-0.34
3jn Si-Ni <sub>5</sub> -POM	FTO/Cu <sub>2</sub> O-Co <sub>x</sub> Se-Ni <sub>y</sub> Se	-1.02
<b>3jn Si-Ni<sub>5</sub>-POM</b>	<b>FTO/Cu<sub>2</sub>O-MnSe</b>	<b>-3.60</b>
3jn Si-Ni <sub>5</sub> -POM	FTO/Cu <sub>2</sub> O-WSe <sub>x</sub>	-1.30
FTO/BiVO <sub>4</sub> -Co <sub>x</sub> P	Pt (single absorber)	0
FTO/BiVO <sub>4</sub> -Co <sub>x</sub> P	FTO/Cu <sub>2</sub> O-Co <sub>x</sub> Se-Ni <sub>y</sub> Se	-0.045
FTO/Fe <sub>2</sub> O <sub>3</sub>	Pt (single absorber)	0
FTO/Fe <sub>2</sub> O <sub>3</sub> -FeSe	FTO/Cu <sub>2</sub> O-Co <sub>x</sub> Se-Ni <sub>y</sub> Se	-0.03
FTO/TiO <sub>2</sub> -Ni <sub>5</sub> -POM	Pt (Single absorber)	-0.08
FTO/TiO <sub>2</sub> -Ni <sub>5</sub> -POM	FTO/Cu <sub>2</sub> O-Co <sub>x</sub> Se-Ni <sub>y</sub> Se	-0.16
FTO/TiO <sub>2</sub> -Ni <sub>5</sub> -POM	FTO/Cu <sub>2</sub> O-WSe <sub>x</sub>	-0.32
<b>FTO/TiO<sub>2</sub>-Ni<sub>5</sub>-POM</b>	<b>FTO/Cu<sub>2</sub>O-MnSe</b>	<b>-0.60</b>

The maximum zero bias photocurrents observed for 3jn Si and metal oxide semiconductor photoanode based tandem cells were  $-3.6 \text{ mA/cm}^2$  and  $-0.60 \text{ mA/cm}^2$  for 3jn Si/Ni<sub>5</sub>-POM [photoanode]:FTO/Cu<sub>2</sub>O-MnSe [photocathode] and FTO/TiO<sub>2</sub>/Ni<sub>5</sub>-POM [photoanode]:FTO/Cu<sub>2</sub>O-MnSe [photocathode] based multiple absorber water splitting cells, and this can be seen in Figures 6.2 and 6.3 respectively. Assuming a 100% Faradaic efficiency, the maximum solar to hydrogen conversion efficiencies of 3jn Si/Ni<sub>5</sub>-POM [photoanode]:FTO/Cu<sub>2</sub>O-MnSe [photocathode] and FTO/TiO<sub>2</sub>/Ni<sub>5</sub>-POM [photoanode]:FTO/Cu<sub>2</sub>O-MnSe [photocathode] were calculated (see Eq. 1.8, Chapter I) to be 4.2% and 0.73%. Figure 6.4 provides the two electrode linear sweep voltammogram for overall water splitting using 3jn Si/Ni<sub>5</sub>-POM [Photoanode]:FTO/Cu<sub>2</sub>O-MnSe [photocathode] cell. It can be clearly observed from the figure that the photocurrents in dual absorber cells (Figures 6.4a and 6.4b) are significantly higher than that obtained by using 3jn Si as the lone light absorber (Figure 6.4c and 6.4a). Similarly, it can be seen upon comparing the zero bias photocurrent for FTO/TiO<sub>2</sub>/Ni<sub>5</sub>-POM [photoanode]:FTO/Cu<sub>2</sub>O-MnSe [photocathode] cell in figure 6.3 and the zero bias photocurrent of FTO/TiO<sub>2</sub>-Ni<sub>5</sub>-POM (Figure 2.9, Chapter II) that the dual absorber cell photocurrent was ~7 times higher than using FTO/TiO<sub>2</sub>-Ni<sub>5</sub>-POM as the lone photoelectrode.

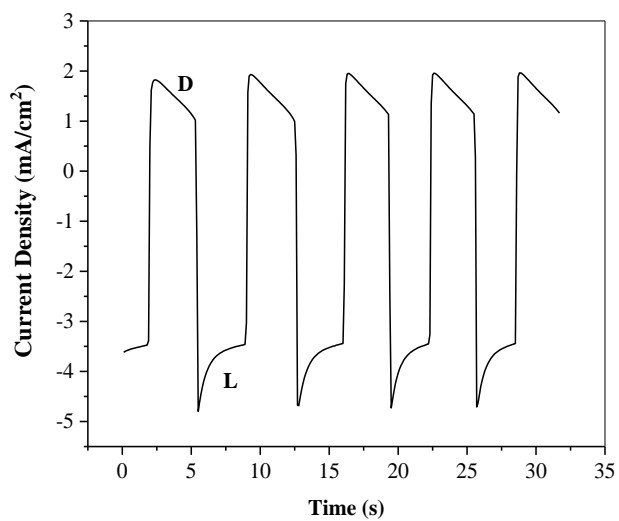


Figure 6.2 Zero bias photocurrent measurements on 3jn Si/Ni<sub>5</sub>-POM [photoanode]:FTO/Cu<sub>2</sub>O-MnSe [photocathode]. L: light irradiation, D: dark conditions. Conditions mentioned in Section 6.2.3.

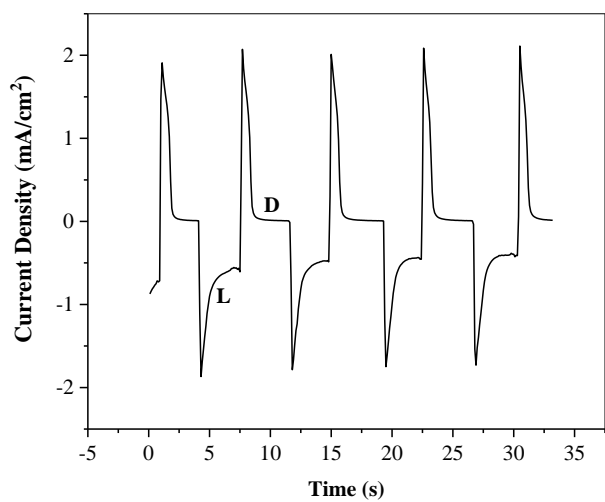


Figure 6.3 Zero bias photocurrent measurements on FTO/TiO<sub>2</sub>/Ni<sub>5</sub>-POM [photoanode]:FTO/Cu<sub>2</sub>O-MnSe [photocathode]. L: light irradiation, D: dark conditions. Conditions mentioned in Section 6.2.3.



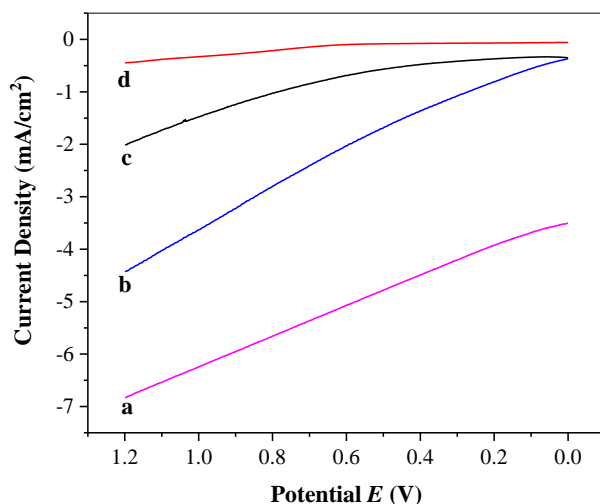


Figure 6.4 Two-electrode photocurrent measurements on (a) 3jn Si/Ni<sub>5</sub>-POM [photoanode]:FTO/Cu<sub>2</sub>O-MnSe [photocathode], (b) 3jn Si [photoanode]:FTO/Cu<sub>2</sub>O-MnSe [photocathode], (c) 3jn Si/Ni<sub>5</sub>-POM [photoanode]:Pt [cathode] and (d) 3jn Si [photoanode]: Pt [cathode] under simulated solar irradiation. Conditions mentioned in Section 6.2.3.

As explained in the Section 1.2.3.2 of the Chapter I, the high overall water splitting performance of dual absorber based cells could be attributed to increased solar energy utilization and overall generation of photo-induced charge carriers which can be used for solar water oxidation and water reduction. For instance, in the case of FTO/TiO<sub>2</sub>/Ni<sub>5</sub>-POM [photoanode]:FTO/Cu<sub>2</sub>O-MnSe [photocathode] dual absorber cell, TiO<sub>2</sub> has a band gap of 3.22 eV (Figure 2.5 of Chapter II), whereas Cu<sub>2</sub>O has a band gap of 2.4 eV (Figure 4.1 of Chapter IV). The wide band gap of TiO<sub>2</sub> limits its solar energy absorption range, though its valence and conduction band edges match the electrochemical potentials for water oxidation and water reduction. Despite the fact that Cu<sub>2</sub>O has a wider solar absorption range, it cannot oxidize water by itself since it is a p-type semiconductor and its valence band edge does not match adequately with the water oxidation potential. Hence, the multiple absorber water splitting systems would be able to

utilize a broader region of the solar spectrum and facilitate overall water splitting when compared to using FTO/TiO<sub>2</sub>-Ni<sub>5</sub>-POM or Cu<sub>2</sub>O alone as photoelectrodes.

Table 6.2 Zero bias photocurrent comparison

<b>Water splitting system</b>	<b>Electrolyte</b>	<b>Zero Bias Current Density (mA/cm<sup>2</sup>)<sup>a</sup></b>	<b>Ref.</b>
BiVO <sub>4</sub> photocathode (Co-Pi catalyst): Cu <sub>2</sub> O photoanode (RuO <sub>2</sub> catalyst), stacked configuration	0.50 M Na <sub>2</sub> SO <sub>4</sub> , 0.090 M KH <sub>2</sub> PO <sub>4</sub> , 0.010 M K <sub>2</sub> HPO <sub>4</sub> , pH 6.0.	> -1	33
Tandem heterostructure photoanode: p <sup>+</sup> n black silicon (Si)/SnO <sub>2</sub> interface/W-doped bismuth vanadate (BiVO <sub>4</sub> )/cobalt phosphate (CoPi) catalyst.	pH 7.0 phosphate buffer	~-0.35	161
Cu <sub>2</sub> O/Cu <sub>2</sub> S photocathodes, ZnO/CdS photoanodes	0.50 M Na <sub>2</sub> SO <sub>4</sub>	~-0.15	162
Dual junction perovskite solar cell/hematite photoanode tandem cell	1 M NaOH	~-1.8	163
FTO/Cu <sub>2</sub> O-MnSe photocathode, 3 jn Si photoanode, 20 μM Ni <sub>5</sub> -POM in solution.	0.050 M pH 9.0 Borate Buffer	~-3.5	This work
FTO/Cu <sub>2</sub> O-MnSe photocathode, FTO/TiO <sub>2</sub> photoanode, 20 μM Ni <sub>5</sub> -POM in solution.	0.050 M pH 9.0 Borate Buffer	~-0.60	This work

<sup>a</sup> The mathematical sign of obtained photocurrents were changed to follow ACS convention.

These results are promising since there have been no previous studies on the use of polyoxometalate and metal chalcogenide based water oxidation and reduction co-catalysts in tandem cells. Especially, the FTO/TiO<sub>2</sub>-Ni<sub>5</sub>-POM dual absorber cell has been developed completely using earth abundant co-catalysts and inexpensive photoelectrode processing techniques such as spin coating and electrodeposition. Table 6.2 compares the

obtained zero bias photocurrents to a few highly cited or recent reports based on non-noble metal based tandem cells.

It can also be seen in most cases that dual absorber based systems having solution based polyoxometalate co-catalysts for either water oxidation or water reduction exhibited better overall water splitting performance than cells containing purely heterogeneous co-catalysts on both electrode surfaces. Increased overall resistance resulting from the addition of heterogeneous catalysts on both photoelectrodes could be one of the factors causing this difference. Moreover, the use of homogeneous catalysts on an industrial standpoint has unique advantages over heterogeneous co-catalysts, since stability of catalyst films in the face of prolonged gas evolution is not a factor, and it is more convenient to design flow systems that can replace inactivated homogeneous catalysts. Future studies could focus on engineering stacked tandem cell designs with lower overall resistance, increased rates charge transfer and diffusion of homogeneous catalysts to the electrode surface could result in higher photocurrents.

### **6.3.2 Dissolved Oxygen Measurements**

O<sub>2</sub> detection was carried out using a Clark electrode-type dissolved oxygen (DO) sensor during multi-potential pulse experiments. The cell was degassed with ultrapure N<sub>2</sub> (Airgas, Hattiesburg, MS) for 15 min prior to the start of the experiment, and was placed under a N<sub>2</sub> blanket throughout the course of measurements. During measurements, the applied potential was stepped between 0 and 1.10 V, each for a period of 3 s. It can be seen from the difference between Figure 6.5a and 6.5b, c that the overall increase in dissolved oxygen concentration higher for the tandem cell is significantly higher than that using 3 jn Si/Ni<sub>5</sub>-POM as the lone light absorber. Over a period of 200 s, the maximum

amount of DO produced by the 3jn Si/Ni<sub>5</sub>-POM (Photoanode):FTO/Cu<sub>2</sub>O-MnSe (Photocathode) dual absorber cell is ~10 times higher than the 3 jn Si/Ni<sub>5</sub>-POM photoanode by itself. As the oxygen sensor was placed near the photoelectrode, the recorded DO levels should be a reflection of instant local oxygen concentrations and could be an over-estimation of real time values and Faradaic efficiencies (185%, 210% and 194% for systems in Figures 6.5a, b, and c respectively). However, the observed overall trends clearly confirm oxygen evolution, co-relate with observed photocurrent trends and indicate the superiority of non-noble metal co-catalyst based dual absorber cell configurations to single absorber systems.

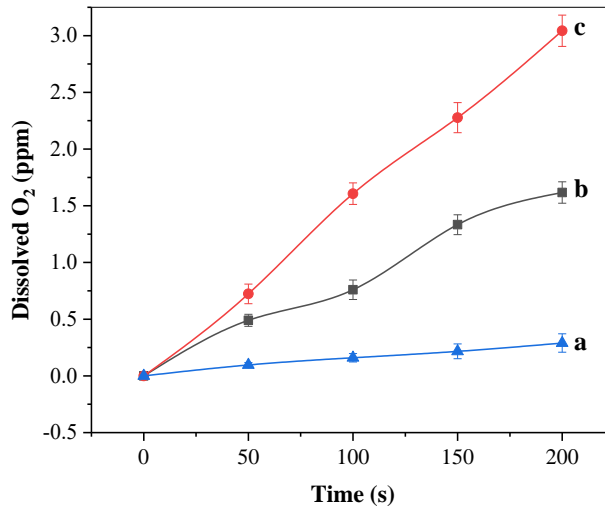


Figure 6.5 Two electrode dissolved oxygen measurements on (a) 3jn Si/Ni<sub>5</sub>-POM [photoanode]:Pt [cathode] (b) FTO/TiO<sub>2</sub>/Ni<sub>5</sub>-POM [photoanode]:FTO/Cu<sub>2</sub>O-MnSe [photocathode] (c) 3jn Si/Ni<sub>5</sub>-POM [Photoanode]:FTO/Cu<sub>2</sub>O-MnSe [Photocathode]. Conditions mentioned in Section 6.2.3.

### 6.3.3 Stability Studies

Multiple-potential step experiments in a typical two-electrode system were used to study the stability of 3jn Si/Ni<sub>5</sub>-POM [Photoanode]:FTO/Cu<sub>2</sub>O-MnSe [Photocathode] water splitting cell. The applied potential was regularly shifted from 0 to 1.10 V in 5 s intervals for a time period of 1400 s, and responses of photocurrent were recorded. Figure 6.6A is the plot of photocurrent density vs time under multi-potential step excitations from the full range of 1400 s. The high observed photocurrents caused vigorous gas evolution, and the noisy spikes in the observed data are due to the blocking and release of oxygen gas on the electrode surfaces. No major loss of catalyst coating was visibly observed at the end of the experiment. The true indication of change in photocurrent is given by Figure 6.6B, which is the zero bias photocurrent plot of 3jn Si/Ni<sub>5</sub>-POM [Photoanode]:FTO/Cu<sub>2</sub>O-MnSe [Photocathode] after potential pulsing, It can be seen that the photocurrent stabilizes at  $\sim 3.3$  mA/cm<sup>2</sup>, which is a small decrease of  $\sim 0.20$  mA/cm<sup>2</sup> ( $\sim 6.5\%$ ) compared to that before pulsing (Figure 6.2). Considering these observations and the operating potentials required to split water, this system can be considered stable under a wide water electrolysis potential range.

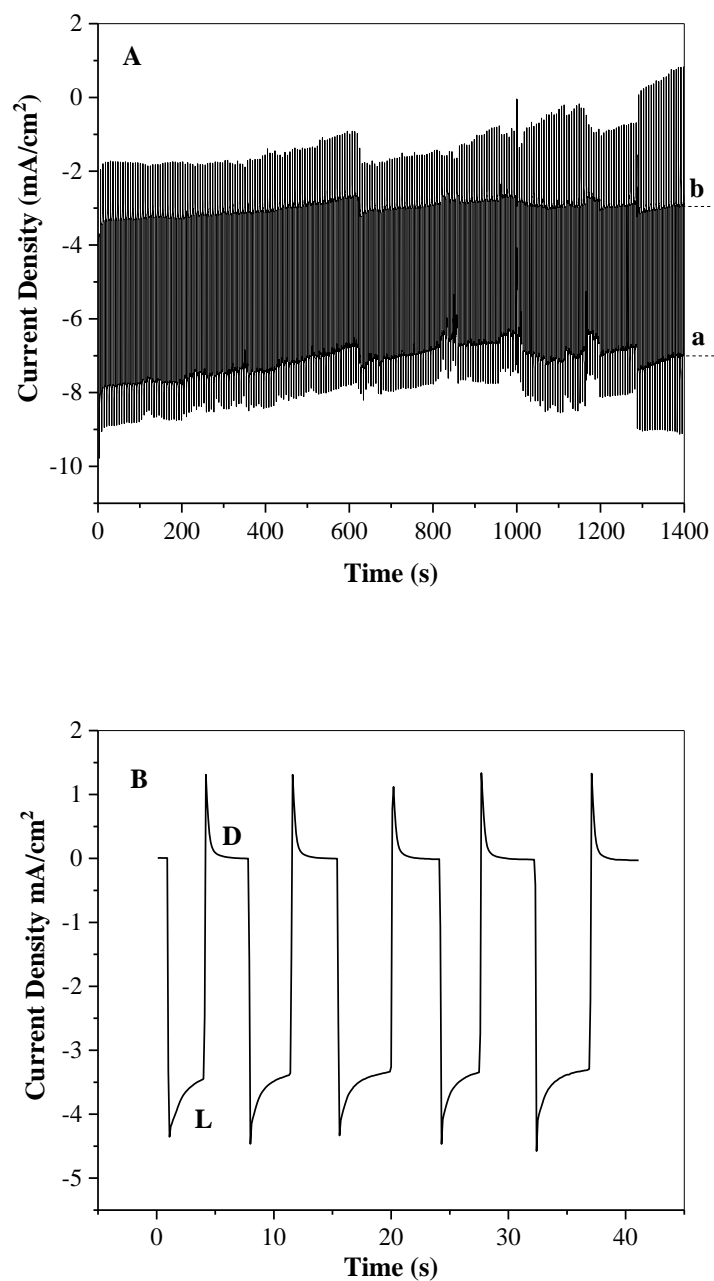


Figure 6.6 (A) Multi-potential step stability studies of 3jn Si/Ni<sub>5</sub>-POM [Photoanode]:FTO/Cu<sub>2</sub>O-MnSe [Photocathode] under simulated solar light. Potentials applied at a. 1.10 V and b. 0 V. (B) Zero bias photocurrent plot of 3jn Si/Ni<sub>5</sub>-POM [Photoanode]:FTO/Cu<sub>2</sub>O-MnSe [Photocathode] after stability measurements. L: light irradiation, D: dark conditions. Conditions mentioned in Section 6.2.3.

## 6.4 Conclusion

In this chapter, a variety of multiple light absorber configurations were studied based on non-noble metal co-catalysts discussed in the previous chapters. Photoelectrochemical measurements and dissolved oxygen measurements clearly showed that overall water splitting performance and photocurrents were higher in multiple light absorber systems than those of single absorber photoelectrodes. FTO/TiO<sub>2</sub>/Ni<sub>5</sub>-POM [photoanode]:FTO/Cu<sub>2</sub>O-MnSe [photocathode] and 3jn Si/Ni<sub>5</sub>-POM [photoanode]:FTO/Cu<sub>2</sub>O-MnSe [photocathode] produced the maximum zero bias photocurrents for the multiple absorber configurations based on metal oxide semiconductor and 3 jn Si based photoanode respectively. Current data are promising since there is limited literature on non-noble metal co-catalyst based tandem cells as of writing. Engineering stacked tandem cell designs with lower overall resistance, increased rates charge transfer and diffusion of homogenous catalysts to the electrode surface could be the focus of future studies.

## CHAPTER VII . SUMMARY AND FUTURE PERSPECTIVES

Photoelectrochemical water splitting is a safe, localized and room temperature technique to produce hydrogen directly from earth abundant water using solar energy. Water oxidation and reduction co-catalysts play an important role in decreasing onset potential and electron hole recombination through electron/hole capture for catalytic activity. Studies on non-noble metal based catalysts are essential to reduce overall operating costs. This dissertation studies focused on two classes of non-noble metal based co-catalysts viz. transition metal polyoxometalates in solution and metal chalcogenide based heterogenous co-catalysts

Chapters II and III presented data on the photoelectrochemical studies of polyoxometalate based water oxidation and water reduction catalysts in solution. In Chapter II, photoelectrochemical studies on earth abundant water oxidation catalyst Ni<sub>5</sub>-POM in solution for solar water oxidation using spin coated FTO/TiO<sub>2</sub>-Ni<sub>5</sub>POM photoanodes were reported. A maximum photocurrent of -0.20 mA/cm<sup>2</sup> at 0.70 vs Ag/AgCl (3.0 M KCl) was observed under illumination (1 sun) in the presence of 20 μM Ni<sub>5</sub>-POM (pH 9.0, 0.050M Borate buffer), and the EIS measurements provided evidence on the effect of catalyst in increasing electron-hole separation through hole capture and catalytic activity. This system is also significant considering that unbiased photocurrent was produced from anatase TiO<sub>2</sub> photoelectrode under simulated solar light in presence of Ni<sub>5</sub>-POM. Oxygen was detected using a Clark electrode-type dissolved oxygen sensor, and stability studies indicated that the TiO<sub>2</sub> film on FTO was stable even under harsh operating potential ranges.



Chapter III focused on the use of transition metal polyoxometalate based catalysts for solar water reduction, and provided photoelectrochemical studies on electrodeposited  $\text{Cu}_x\text{Se}$  photocathodes in the presence of nonacobalt polyoxometalate  $\text{Co}_9\text{-POM}$ . Three-electrode photocurrent measurements under dark conditions indicated a significant  $\sim 0.1$  V positive shift in electrocatalytic positive shift in water reduction upon addition of  $20 \mu\text{M}$   $\text{Co}_9\text{-POM}$ . The maximum observed current density under light illumination in the presence of  $\text{Co}_9\text{-POM}$  was  $\sim 1.3 \text{ mA/cm}^2$  at  $-0.40 \text{ V vs Ag/AgCl (3.0 M KCl)}$ , which is amongst the highest reported in literature within our measured potential range. EIS measurements and Mott Schottky plots pointed at the effect of  $\text{Co}_9\text{-POM}$  in increasing electron-hole separation and charge carrier concentration through electron capture for HER catalytic activity. There have been no previous studies on  $\text{Co}_9\text{-POM}$  and  $\text{Ni}_5\text{-POM}$  as solution based catalysts for solar water splitting, and the use of  $\text{Cu}_x\text{Se}$  as a HER photocathode in itself was limited in literature. Considering these factors and the photoelectrocatalytic HER/OER performance observed, this project could lead to further studies in the area.

Chapters IV and V presented data on electrodeposited heterogeneous metal chalcogenide based co-catalysts for solar water oxidation and water reduction. In Chapter IV, three transition metal selenide based water reduction catalysts viz.  $\text{MnSe}$ ,  $\text{WSe}_x$ , and  $\text{Co}_x\text{Se-Ni}_y\text{Se}$ . It was seen from photocurrent measurements and SEM that catalyst deposition time influenced thickness and morphology, and played a role in the overall HER performance. A maximum photocurrent of  $\sim 2 \text{ mA/cm}^2$  at  $-0.45 \text{ V vs Ag/AgCl}$  was observed from  $\text{FTO/Cu}_2\text{O-MnSe}$  photocathode of optimized deposition time (20 min). This study is significant since the HER photocurrent is amongst the highest till date in

this applied potential range and pH, and the use of MnSe as a co-catalyst for solar water reduction is limited in literature.

In Chapter V, transition metal phosphides and selenides had been used as heterogenous catalysts for solar water oxidation. Two photoanodes viz FTO/Fe<sub>2</sub>O<sub>3</sub>-FeSe and FTO/BiVO<sub>4</sub>-Co<sub>x</sub>P were reported for PEC water oxidation. Photocurrent measurements on optimized photoelectrodes showed increased OER current densities due to catalytic activity and increased charge separation. The FTO/BiVO<sub>4</sub>-Co<sub>x</sub>P photoanodes produced a maximum photocurrent of -0.67 mA/cm<sup>2</sup> at 0.70 V vs Ag/AgCl (3.0 M KCl), and Impedance spectroscopic studies and Mott Schottky plots indicated the effect of co-catalysts in increasing electron-hole separation and overall charge carrier density. This trend was reflected in dissolved oxygen measurements, which provided definitive evidence of increased oxygen evolution in the presence of Co<sub>x</sub>P co-catalyst. FTO/BiVO<sub>4</sub>-Co<sub>x</sub>P was also found to be stable in a wide operating potential window, as evidenced by multi-potential step stability studies.

In Chapter VI, the photoelectrodes studied in Chapters II-V were studied in multiple light absorber configurations. Photoelectrochemical measurements and dissolved oxygen measurements clearly showed that overall water splitting performance and photocurrents were higher in multiple light absorber systems than single absorber photoelectrodes. FTO/TiO<sub>2</sub>/Ni<sub>5</sub>-POM [photoanode]:FTO/Cu<sub>2</sub>O-MnSe [photocathode] and 3jn Si/Ni<sub>5</sub>-POM [photoanode]:FTO/Cu<sub>2</sub>O-MnSe [photocathode] produced zero bias photocurrents of -0.6 mA/cm<sup>2</sup> and -3.6 mA/cm<sup>2</sup>, which were the maximum values obtained for the multiple absorber configurations based on metal oxide semiconductor and 3jn Si based photoanodes respectively in this dissertation. In addition, the unbiased

photocurrent from 3jn Si/Ni<sub>5</sub>-POM [photoanode]:FTO/Cu<sub>2</sub>O-MnSe [photocathode] is also amongst the upper end of photocurrents reported from present non-noble metal based tandem systems reported in literature.

Considering the higher overall tandem cell performance of polyoxometalate based catalysts in solution for multiple absorber PEC water splitting, future directions can proceed further in this direction. Moreover, the use of homogenous catalysts in solution could solve the problem of added resistance on the electrode surface and blocking of light transmission due to the presence of heterogeneous catalysts. Moving forward, studies on engineering stacked tandem cell designs with lower overall resistance, increased rates charge transfer and diffusion of homogenous catalysts could increase water splitting performance further.

## REFERENCES

1. Mayer, M. T., Photovoltage At Semiconductor–Electrolyte Junctions. *Curr. Op. Electrochem.* **2017**, 2 (1), 104-110.
2. Du, P.; Eisenberg, R., Catalysts Made of Earth-Abundant Elements (Co, Ni, Fe) for Water Splitting: Recent Progress and Future Challenges. *Energy Environ. Sci.* **2012**, 5 (3), 6012-6021.
3. Ran, J.; Zhang, J.; Yu, J.; Jaroniec, M.; Qiao, S. Z., Earth-Abundant Cocatalysts for Semiconductor-based Photocatalytic Water Splitting. *Chem. Soc. Rev.* **2014**.
4. Yang, G.; Jiang, Z.; Shi, H.; Xiao, T.; Yan, Z., Preparation of Highly Visible-Light Active N-Doped TiO<sub>2</sub> Photocatalyst. *J. Mater. Chem.* **2010**, 20 (25), 5301-5309.
5. Pacala, S.; Socolow, R., Stabilization Wedges: Solving the Climate Problem for the Next 50 Years with Current Technologies. *Science* **2004**, 305 (5686), 968-972.
6. Hoffert, M. I., Farewell to Fossil Fuels? *Science* **2010**, 329 (5997), 1292-1294.
7. Lewis, N. S.; Nocera, D. G., Powering the planet: Chemical challenges in solar energy utilization. *Proc. Natl. Acad. Sci.* **2006**, 103 (43), 15729-15735.
8. Lewis, N. S., Crabtree, G In *Basic Research Needs for Solar Energy Utilization: report of the Basic Energy Sciences*, Workshop on Solar Energy Utilization, Washington DC, US Department of Energy, Washington DC, 2005.
9. Juan Carlos, C.; Rafael, L., Heterogeneous Photocatalytic Nanomaterials: Prospects and Challenges in Selective Transformations of Biomass-derived Compounds. *Chem. Soc. Rev.* **2013**, 43 (3), 765-778.
10. Colmenares, J. C.; Luque, R.; Campelo, J. M.; Colmenares, F.; Karpiński, Z.; Romero, A. A., Nanostructured Photocatalysts and Their Applications in the

Photocatalytic Transformation of Lignocellulosic Biomass: An Overview. *Materials* **2009**, 2 (4), 2228-2258.

11. Qu, Y.; Duan, X., Progress, Challenge and Perspective of Heterogeneous Photocatalysts. *Chem. Soc. Rev.* **2013**, 42 (7), 2568-2580.
12. Roel van de Krol, M. G., *Photoelectrochemical Hydrogen Production*. Springer: 2012; Vol. 102.
13. Krishnan Rajeshwar, R. M., Stuart Licht, *Solar Hydrogen Generation: Toward a Renewable Energy Future*. Springer: 2008.
14. Grimes, C. A., Varghese, O.K., Ranjan, S., *Light, Water, Hydrogen*. 2008.
15. Jia, J.; Seitz, L. C.; Benck, J. D.; Huo, Y.; Chen, Y.; Ng, J. W. D.; Bilir, T.; Harris, J. S.; Jaramillo, T. F., Solar Water Splitting By Photovoltaic-Electrolysis with a Solar-To-Hydrogen Efficiency Over 30%. *Nat. Commun.* **2016**, 7, 13237.
16. Goikoetxea, N. B.; Gómez-Mancebo, M. B.; Fernández-Saavedra, R.; García-Pérez, F.; Jiménez, J. A.; Rodríguez, J.; Rucandio, I.; Quejido, A. J., Study of The Performance Of Co And Ni Ferrites After Several Cycles Involved in Water-Splitting Thermochemical Cycles. *Int. J. Hydrogen Energy* **2016**, 41 (38), 16696-16704.
17. Lange, M.; Roeb, M.; Sattler, C.; Pitz-Paal, R., Efficiency Assessment of a Two-Step Thermochemical Water-Splitting Process Based On A Dynamic Process Model. *Int. J. Hydrogen Energy* **2015**, 40 (36), 12108-12119.
18. Akkerman, I.; Janssen, M.; Rocha, J.; Wijffels, R. H., Photobiological Hydrogen Production: Photochemical Efficiency And Bioreactor Design. *Int. J. Hydrogen Energy* **2002**, 27 (11), 1195-1208.

19. Bandyopadhyay, A.; Stöckel, J.; Min, H.; Sherman, L. A.; Pakrasi, H. B., High Rates Of Photobiological H<sub>2</sub> Production By A Cyanobacterium Under Aerobic Conditions. *Nat. Commun.* **2010**, *1*, 139.
20. Walter, M. G.; Warren, E. L.; McKone, J. R.; Boettcher, S. W.; Mi, Q.; Santori, E. A.; Lewis, N. S., Solar Water Splitting Cells. *Chem. Rev.* **2010**, *110* (11), 6446-6473.
21. <http://3.bp.blogspot.com/>
22. Fujishima, A.; Honda, K., Electrochemical photolysis of water at a semiconductor electrode. *Nature* **1972**, *238* (5358), 37-8.
23. Peter, L. M.; Wijayantha, K. G. U., Photoelectrochemical Water Splitting at Semiconductor Electrodes: Fundamental Problems and New Perspectives. *Chemphyschem* **2014**, *15* (10), 1983-1995.
24. Sivula, K.; Le Formal, F.; Grätzel, M., Solar Water Splitting: Progress Using Hematite ( $\alpha$ -Fe<sub>2</sub>O<sub>3</sub>) Photoelectrodes. *ChemSusChem* **2011**, *4* (4), 432-449.
25. Prévot, M. S.; Sivula, K., Photoelectrochemical Tandem Cells for Solar Water Splitting. *J.Phys. Chem. C* **2013**, *117* (35), 17879-17893.
26. Bolton, J. R., Solar Photoproduction of Hydrogen: A Review. *Solar Energy* **1996**, *57* (1), 37-50.
27. Imanishi, A.; Okamura, T.; Ohashi, N.; Nakamura, R.; Nakato, Y., Mechanism of Water Photooxidation Reaction at Atomically Flat TiO<sub>2</sub> (Rutile) (110) and (100) Surfaces: Dependence on Solution pH. *J. Am. Chem. Soc.* **2007**, *129* (37), 11569-11578.
28. Kisumi, T.; Tsujiko, A.; Murakoshi, K.; Nakato, Y., Crystal-face and illumination intensity dependences of the quantum efficiency of photoelectrochemical etching, in

- relation to those of water photooxidation, at n-TiO<sub>2</sub> (rutile) semiconductor electrodes. *J. Electroanal. Chem.* **2003**, *545* (0), 99-107.
29. Gratzel, M., Photoelectrochemical Cells. *Nature* **2001**, *414* (6861), 338-344.
30. J. R. Bolton, A. F. H., R. T. Ross., *Photoelectrochemical Conversion and Storage of Solar Energy*. J S Connolly, Academic New York,,: 1981.
31. Weber, M. F.; Dignam, M. J., Efficiency of Splitting Water with Semiconducting Photoelectrodes. *J. Electrochem. Soc.* **1984**, *131* (6), 1258-1265.
32. Sivula, K.; Gratzel, M., CHAPTER 4 Tandem Photoelectrochemical Cells for Water Splitting. In *Photoelectrochemical Water Splitting: Materials, Processes and Architectures*, The Royal Society of Chemistry: 2013; pp 83-108.
33. Bornoz, P.; Abdi, F. F.; Tilley, S. D.; Dam, B.; van de Krol, R.; Graetzel, M.; Sivula, K., A Bismuth Vanadate–Cuprous Oxide Tandem Cell for Overall Solar Water Splitting. *J. Phys. Chem. C* **2014**, *118* (30), 16959-16966.
34. Yang, J.; Wang, D.; Han, H.; Li, C., Roles of Cocatalysts in Photocatalysis and Photoelectrocatalysis. *Acc. Chem. Res.* **2013**, *46* (8), 1900-1909.
35. Wen, F.; Li, C., Hybrid Artificial Photosynthetic Systems Comprising Semiconductors as Light Harvesters and Biomimetic Complexes as Molecular Cocatalysts. *Acc. Chem. Res.* **2013**, *46* (11), 2355-2364.
36. Kumar, B.; Beyler, M.; Kubiak, C. P.; Ott, S., Photoelectrochemical Hydrogen Generation by an [FeFe] Hydrogenase Active Site Mimic at a p-Type Silicon/Molecular Electrocatalyst Junction. *Chem. – Eur. J.* **2012**, *18* (5), 1295-1298.

37. Ye, H.; Park, H. S.; Bard, A. J., Screening of Electrocatalysts for Photoelectrochemical Water Oxidation on W-Doped BiVO<sub>4</sub> Photocatalysts by Scanning Electrochemical Microscopy. *J. Phys. Chem. C* **2011**, *115* (25), 12464-12470.
38. Jia, Q.; Iwashina, K.; Kudo, A., Facile Fabrication of an Efficient BiVO<sub>4</sub> Thin Film Electrode for Water Splitting under Visible Light Irradiation. *Proc. Natl. Acad. Sci. USA* **2012**, *109* (29), 11564-11569.
39. Reece, S. Y.; Hamel, J. A.; Sung, K.; Jarvi, T. D.; Esswein, A. J.; Pijpers, J. J. H.; Nocera, D. G., Wireless Solar Water Splitting Using Silicon-Based Semiconductors and Earth-Abundant Catalysts. *Science* **2011**, *334* (6056), 645.
40. Bockris, J. O. M.; Ammar, I. A.; Huq, A. K. M. S., The Mechanism of the Hydrogen Evolution Reaction on Platinum, Silver and Tungsten surfaces in Acid Solutions. *J. Phys. Chem.* **1957**, *61* (7), 879-886.
41. Parsons, R., Hydrogen Evolution on Platinum Electrodes. the Heats of Activation for the Component Reactions. *Trans. Faraday Soc.* **1960**, *56* (0), 1340-1350.
42. Nohra, B.; El Moll, H.; Rodriguez Albelo, L. M.; Mialane, P.; Marrot, J.; Mellot-Draznieks, C.; O'Keefe, M.; Ngo Biboum, R.; Lemaire, J.; Keita, B.; Nadjo, L.; Dolbecq, A., Polyoxometalate-Based Metal Organic Frameworks (POMOFs): Structural Trends, Energetics, and High Electrocatalytic Efficiency for Hydrogen Evolution Reaction. *J. Am. Chem. Soc.* **2011**, *133* (34), 13363-13374.
43. Hu, W.; Chen, S. L.; Xia, Q. H., IrO<sub>2</sub>/Nb-TiO<sub>2</sub> Electrocatalyst for Oxygen Evolution Reaction in Acidic Medium. *Int. J. Hydrogen Energ.* **2014**, *39* (13), 6967-6976.



44. Stoerzinger, K. A.; Qiao, L.; Biegalski, M. D.; Shao-Horn, Y., Orientation-Dependent Oxygen Evolution Activities of Rutile IrO<sub>2</sub> and RuO<sub>2</sub>. *J. Phys. Chem. Lett.* **2014**, *5* (10), 1636-1641.
45. Swierk, J. R.; McCool, N. S.; Saunders, T. P.; Barber, G. D.; Strayer, M. E.; Vargas-Barbosa, N. M.; Mallouk, T. E., Photovoltage Effects of Sintered IrO<sub>2</sub> Nanoparticle Catalysts in Water-Splitting Dye-Sensitized Photoelectrochemical Cells. *J. Phys. Chem. C* **2014**, *118* (30), 17046-17053.
46. Godwin, I. J.; Doyle, R. L.; Lyons, M. E. G., The Mechanism of Oxygen Reactions at Porous Oxide Electrodes III. Water Oxidation Catalysis at RuO<sub>2</sub>/NiO Mixed Oxide Electrodes. *J. Electrochem. Soc.* **2014**, *161* (9), F906-F917.
47. Janaky, C.; Chanmanee, W.; Rajeshwar, K., On the Substantially Improved Photoelectrochemical Properties of Nanoporous WO<sub>3</sub> Through Surface Decoration with RuO<sub>2</sub>. *Electrocatal.* **2013**, *4* (4), 382-389.
48. Jeon, H. S.; Permana, A. D. C.; Kim, J.; Min, B. K., Water splitting for hydrogen production using a high surface area RuO<sub>2</sub> electrocatalyst synthesized in supercritical water. *Int. J. Hydrogen Energ.* **2013**, *38* (14), 6092-6096.
49. Nocera, D. G., The Artificial Leaf. *Acc. of Chem. Res.* **2012**, *45* (5), 767-776.
50. Basil, B. S. Transition Metal containing Silico and Germanotungstates. Jacobs University, Germany, 2008.
51. Geletii, Y. V.; Yin, Q.; Hou, Y.; Huang, Z.; Ma, H.; Song, J.; Besson, C.; Luo, Z.; Cao, R.; O'Halloran, K. P.; Zhu, G.; Zhao, C.; Vickers, J. W.; Ding, Y.; Mohebbi, S.; Kuznetsov, A. E.; Musaev, D. G.; Lian, T.; Hill, C. L., Polyoxometalates in the Design of Effective and Tunable Water Oxidation Catalysts. *Isr. J. Chem.* **2011**, *51* (2), 238-246.

52. Han, Z.; Bond, A. M.; Zhao, C., Recent Trends in the use of Polyoxometalate-based Material for Efficient Water Oxidation. *Sci. China-Chem.* **2011**, *54* (12), 1877-1887.
53. Lv, H.; Geletii, Y. V.; Zhao, C.; Vickers, J. W.; Zhu, G.; Luo, Z.; Song, J.; Lian, T.; Musaev, D. G.; Hill, C. L., Polyoxometalate Water Oxidation Catalysts and the Production of Green Fuel. *Chem. Soc. Rev.* **2012**, *41* (22), 7572-7589.
54. Lv, H.; Song, J.; Zhu, H.; Geletii, Y. V.; Bacsa, J.; Zhao, C.; Lian, T.; Musaev, D. G.; Hill, C. L., Visible-light-driven Hydrogen Evolution from Water Using a Noble-Metal-Free Polyoxometalate Catalyst. *J. Catal.* **2013**, *307*, 48-54.
55. Song, F.; Ding, Y.; Zhao, C., Progress in Polyoxometalates-Catalyzed Water Oxidation. *Acta Chim. Sinica* **2014**, *72* (2), 133-144.
56. Falkenhagen, J. P.; Braun, B.; Bill, E.; Sattler, D.; Limberg, C., A Cubic Fe<sub>4</sub>Mo<sub>4</sub> Oxo Framework and Its Reversible Four-Electron Redox Chemistry. *Inorg. Chem.* **2014**, *53* (14), 7294-7308.
57. Orlandi, M.; Argazzi, R.; Sartorel, A.; Carraro, M.; Scorrano, G.; Bonchio, M.; Scandola, F., Ruthenium Polyoxometalate Water Splitting Catalyst: Very Fast Hole Scavenging from Photogenerated Oxidants. *Chem. Commun.* **2010**, *46* (18), 3152-3154.
58. Sumliner, J. M.; Lv, H.; Fielden, J.; Geletii, Y. V.; Hill, C. L., Polyoxometalate Multi-Electron-Transfer Catalytic Systems for Water Splitting. *Eur. J. Inorg. Chem.* **2014**, (4), 635-644.
59. Yang, Y.; Zhang, B.; Wang, Y.; Yue, L.; Li, W.; Wu, L., A Photo-driven Polyoxometalate Complex Shuttle and its Homogeneous Catalysis and Heterogeneous Separation. *J. Am. Chem. Soc.* **2013**, *135* (39), 14500-14503.

60. Piccinin, S.; Fabris, S., A first Principles study of Water Oxidation Catalyzed by a Tetra-ruthenium-oxo Core Embedded in Polyoxometalate Ligands. *Phys. Chem. Chem. Phys.* **2011**, *13* (17), 7666-7674.
61. Guo, S.-X.; Liu, Y.; Lee, C.-Y.; Bond, A. M.; Zhang, J.; Geletii, Y. V.; Hill, C. L., Graphene-supported  $\{\text{Ru}_4\text{O}_4(\text{OH})_2(\text{H}_2\text{O})_4\}$ - $(\gamma\text{-SiW}_{10}\text{O}_{36})_2^{10-}$  for Highly Efficient Electrocatalytic Water Oxidation. *Energ. & Environ. Sci.* **2013**, *6* (9), 2654-2663.
62. Kar, P.; Rana, P. J. S., Ruthenium Polyoxometalate as Water Splitting Catalyst: Enhancement of Photochemical Water Oxidation in Presence of CAN. *Bull. Korean Chem. Soc.* **2014**, *35* (7), 1931-1932.
63. Sartorel, A.; Miro, P.; Salvadori, E.; Romain, S.; Carraro, M.; Scorrano, G.; Di Valentin, M.; Llobet, A.; Bo, C.; Bonchio, M., Water Oxidation at a Tetra-ruthenate Core Stabilized by Polyoxometalate Ligands: Experimental and Computational Evidence To Trace the Competent Intermediates. *J. Am. Chem. Soc.* **2009**, *131* (44), 16051.
64. Huang, Z.; Luo, Z.; Geletii, Y. V.; Vickers, J. W.; Yin, Q.; Wu, D.; Hou, Y.; Ding, Y.; Song, J.; Musaev, D. G.; Hill, C. L.; Lian, T., Efficient Light-Driven Carbon-Free Cobalt-Based Molecular Catalyst for Water Oxidation. *J. Am. Chem. Soc.* **2011**, *133* (7), 2068-2071.
65. Lv, H.; Song, J.; Geletii, Y. V.; Vickers, J. W.; Sumliner, J. M.; Musaev, D. G.; Koegele, P.; Zhuk, P. F.; Bacsa, J.; Zhu, G.; Hill, C. L., An Exceptionally Fast Homogeneous Carbon-Free Cobalt-Based Water Oxidation Catalyst. *J. Am. Chem. Soc.* **2014**, *136* (26), 9268-9271.

66. Soriano-Lopez, J.; Goberna-Ferron, S.; Vigarra, L.; Carbo, J. J.; Poblet, J. M.; Ramon Galan-Mascaros, J., Cobalt Polyoxometalates as Heterogeneous Water Oxidation Catalysts. *Inorg. Chem.* **2013**, *52* (9), 4753-4755.
67. Zhao, C.; Kambara, C. S.; Song, J.; Lv, H.; Geletii, Y. V.; Zhu, G.; Vickers, J.; Hill, C. L., Water Oxidation by a Polyoxometalate Catalyst Containing Single-Site Cobalt Center. *Abstracts of Papers of the American Chemical Society* **2011**, 242.
68. Zhu, G.; Glass, E. N.; Zhao, C.; Lv, H.; Vickers, J. W.; Geletii, Y. V.; Musaev, D. G.; Song, J.; Hill, C. L., A Nickel containing Polyoxometalate Water Oxidation Catalyst. *Dalton Trans.* **2012**, *41* (42), 13043-13049.
69. Swesi, A. T.; Masud, J.; Nath, M., Nickel Selenide as a High-Efficiency Catalyst for Oxygen Evolution Reaction. *Energy Environ. Sci.* **2016**, *9* (5), 1771-1782.
70. Masud, J.; Swesi, A. T.; Liyanage, W. P. R.; Nath, M., Cobalt Selenide Nanostructures: An Efficient Bifunctional Catalyst with High Current Density at Low Coverage. *ACS Appl. Mater. Interfaces* **2016**, *8* (27), 17292-17302.
71. Du, Y.; Cheng, G.; Luo, W., NiSe<sub>2</sub>/FeSe<sub>2</sub> Nanodendrites: A Highly Efficient Electrocatalyst for Oxygen Evolution Reaction. *Catal. Sci. Tech.* **2017**, *7* (20), 4604-4608.
72. Li, Y.; Yan, D.; Zou, Y.; Xie, C.; Wang, Y.; Zhang, Y.; Wang, S., Rapidly Engineering the Electronic Properties and Morphological Structure of NiSe Nanowires for the Oxygen Evolution Reaction. *J. Mater. Chem. A* **2017**, *5* (48), 25494-25500.
73. Mabayoje, O.; Shoola, A.; Wygant, B. R.; Mullins, C. B., The Role of Anions in Metal Chalcogenide Oxygen Evolution Catalysis: Electrodeposited Thin Films of Nickel Sulfide as "Pre-catalysts". *ACS Energy Lett.* **2016**, *1* (1), 195-201.

74. Cao, S.; Wang, C.-J.; Fu, W.-F.; Chen, Y., Metal Phosphides as Co-Catalysts for Photocatalytic and Photoelectrocatalytic Water Splitting. *ChemSusChem* **2017**, *10* (22), 4306-4323.
75. Wang, Y.; Kong, B.; Zhao, D.; Wang, H.; Selomulya, C., Strategies for Developing Transition Metal Phosphides as Heterogeneous Electrocatalysts for Water Splitting. *Nano Today* **2017**, *15*, 26-55.
76. Shi, Y.; Zhang, B., Recent Advances in Transition Metal Phosphide Nanomaterials: Synthesis and Applications in Hydrogen Evolution Reaction. *Chem. Soc. Rev.* **2016**, *45* (6), 1529-1541.
77. Miao, Y.-E.; Li, F.; Zhou, Y.; Lai, F.; Lu, H.; Liu, T., Engineering a Nanotubular Mesoporous Cobalt Phosphide Electrocatalyst by the Kirkendall Effect Towards Highly Efficient Hydrogen Evolution Reactions. *Nanoscale* **2017**, *9* (42), 16313-16320.
78. Anantharaj, S.; Ede, S. R.; Sakthikumar, K.; Karthick, K.; Mishra, S.; Kundu, S., Recent Trends and Perspectives in Electrochemical Water Splitting with an Emphasis on Sulfide, Selenide, and Phosphide Catalysts of Fe, Co, and Ni: A Review. *ACS Catal.* **2016**, *6* (12), 8069-8097.
79. Subbaraman, R.; Tripkovic, D.; Chang, K.-C.; Strmcnik, D.; Paulikas, A. P.; Hirunsit, P.; Chan, M.; Greeley, J.; Stamenkovic, V.; Markovic, N. M., Trends in Activity for the Water Electrolyser Reactions on 3d M(Ni,Co,Fe,Mn) Hydr(Oxy)Oxide Catalysts. *Nat. Mater.* **2012**, *11*, 550.
80. Jin, S., Are Metal Chalcogenides, Nitrides, and Phosphides Oxygen Evolution Catalysts or Bifunctional Catalysts? *ACS Energy Letters* **2017**, *2* (8), 1937-1938.

81. Stern, L.-A.; Feng, L.; Song, F.; Hu, X., Ni<sub>2</sub>P as a Janus Catalyst for Water Splitting: The Oxygen Evolution Activity of Ni<sub>2</sub>P Nanoparticles. *Energy Environ. Sci.* **2015**, 8 (8), 2347-2351.
82. Lincot, D., Electrodeposition of semiconductors. *Thin Solid Films* **2005**, 487 (1–2), 40-48.
83. Schwartz, R. W.; Schneller, T.; Waser, R., Chemical solution deposition of electronic oxide films. *Comptes Rendus Chimie* **2004**, 7 (5), 433-461.
84. Chen, Z.; Deutsch, T.; Dinh, H.; Domen, K.; Emery, K.; Forman, A.; Gaillard, N.; Garland, R.; Heske, C.; Jaramillo, T.; Kleiman-Shwarsstein, A.; Miller, E.; Takanabe, K.; Turner, J., UV-Vis Spectroscopy. In *Photoelectrochemical Water Splitting*, Springer New York: 2013; pp 49-62.
85. Chen, Z.; Deutsch, T. G.; Dinh, H. N.; Domen, K.; Emery, K.; Forman, A. J.; Gaillard, N.; Garland, R.; Heske, C.; Jaramillo, T. F.; Kleiman-Shwarsstein, A.; Miller, E.; Takanabe, K.; Turner, J., Flat-Band Potential Techniques. In *Photoelectrochemical Water Splitting: Standards, Experimental Methods, and Protocols*, Chen, Z.; Dinh, H. N.; Miller, E., Eds. Springer New York: New York, NY, 2013; pp 63-85.
86. Orazem, M. E.; Tribollet, B., Equivalent Circuit Analogs. In *Electrochemical Impedance Spectroscopy*, John Wiley & Sons, Inc.: 2008; pp 153-162.
87. Chen, Z.; Deutsch, T.; Dinh, H.; Domen, K.; Emery, K.; Forman, A.; Gaillard, N.; Garland, R.; Heske, C.; Jaramillo, T.; Kleiman-Shwarsstein, A.; Miller, E.; Takanabe, K.; Turner, J., Flat-Band Potential Techniques. In *Photoelectrochemical Water Splitting*, Springer New York: 2013; pp 63-85.

88. Chen, Z.; Deutsch, T. G.; Dinh, H. N.; Domen, K.; Emery, K.; Forman, A. J.; Gaillard, N.; Garland, R.; Heske, C.; Jaramillo, T. F.; Kleiman-Shwarsstein, A.; Miller, E.; Takahabe, K.; Turner, J., 2-Electrode Short Circuit and  $j$ - $V$ . In *Photoelectrochemical Water Splitting: Standards, Experimental Methods, and Protocols*, Chen, Z.; Dinh, H. N.; Miller, E., Eds. Springer New York: New York, NY, 2013; pp 99-103.
89. Chen, Z.; Deutsch, T.; Dinh, H.; Domen, K.; Emery, K.; Forman, A.; Gaillard, N.; Garland, R.; Heske, C.; Jaramillo, T.; Kleiman-Shwarsstein, A.; Miller, E.; Takahabe, K.; Turner, J., Efficiency Definitions in the Field of PEC. In *Photoelectrochemical Water Splitting*, Springer New York: 2013; pp 7-16.
90. Prévot, M. S.; Sivula, K., Photoelectrochemical Tandem Cells for Solar Water Splitting. *J. Phys. Chem. C* **2013**, *117* (35), 17879-17893.
91. Zhong, D. K.; Choi, S.; Gamelin, D. R., Near-Complete Suppression of Surface Recombination in Solar Photoelectrolysis by "Co-Pi" Catalyst-Modified W:BiVO<sub>4</sub>. *J. Am. Chem. Soc.* **2011**, *133* (45), 18370-18377.
92. Grimaud, A.; May, K. J.; Carlton, C. E.; Lee, Y.-L.; Risch, M.; Hong, W. T.; Zhou, J.; Shao-Horn, Y., Double Perovskites as a family of Highly Active Catalysts for Oxygen Evolution in Alkaline Solution. *Nat. Commun.* **2013**, *4*.
93. Nepal, B.; Das, S., Sustained Water Oxidation by a Catalyst Cage-Isolated in a Metal–Organic Framework. *Angew. Chem. Int. Ed.* **2013**, *52* (28), 7224-7227.
94. Qu, Y.; Duan, X., Progress, Challenges and Perspectives of Heterogeneous Photocatalysts. *Chem. Soc. Rev.* **2013**, *42* (7), 2568-2580.
95. Bazzan, I.; Volpe, A.; Dolbecq, A.; Natali, M.; Sartorel, A.; Mialane, P.; Bonchio, M., Cobalt Based Water Oxidation Catalysis with Photogenerated Ru(bpy)<sub>3</sub><sup>3+</sup>: Different

- Kinetics and Competent Species starting from a Molecular Polyoxometalate and Metal Oxide Nanoparticles capped with a Bisphosphonate Alendronate Pendant. *Catal. Today* **2015**, *290*, 39-50.
96. Burian, M.; Syrgiannis, Z.; La Ganga, G.; Puntoriero, F.; Natali, M.; Scandola, F.; Campagna, S.; Prato, M.; Bonchio, M.; Amenitsch, H.; Sartorel, A., Ruthenium based Photosensitizer/Catalyst Supramolecular Architectures in Light Driven Water Oxidation. *Inorg. Chim. Acta* **2017**, *454*, 171-175.
97. Folkman, S. J.; Finke, R. G., Electrochemical Water Oxidation Catalysis Beginning with Co(II) Polyoxometalates: The Case of the Precatalyst  $\text{Co}_4\text{V}_2\text{W}_{18}\text{O}_{68}^{10-}$ . *ACS Catal.* **2017**, *7* (1), 7-16.
98. Guo, S.-X.; Liu, Y.; Lee, C.-Y.; Bond, A. M.; Zhang, J.; Geletii, Y. V.; Hill, C. L., Graphene-supported  $\{\text{Ru}_4\text{O}_4(\text{OH})_2(\text{H}_2\text{O})_4\}$ - $(\gamma\text{-SiW}_{10}\text{O}_{36})_2\}^{10-}$  for Highly Efficient Electrocatalytic Water Oxidation. *Energy Environ. Sci.* **2013**, *6* (9), 2654-2663.
99. Cho, S. K.; Park, H. S.; Lee, H. C.; Nam, K. M.; Bard, A. J., Metal Doping of  $\text{BiVO}_4$  by Composite Electrodeposition with Improved Photoelectrochemical Water Oxidation. *J. Phys. Chem. C* **2013**, *117* (44), 23048-23056.
100. Fielden, J.; Sumliner, J. M.; Han, N. N.; Geletii, Y. V.; Xiang, X.; Musaev, D. G.; Lian, T. Q.; Hill, C. L., Water Splitting with Polyoxometalate-treated Photoanodes: Enhancing Performance through Sensitizer Design. *Chemi. Sci.* **2015**, *6* (10), 5531-5543.
101. Yano, J.; Kern, J.; Pushkar, Y.; Sauer, K.; Glatzel, P.; Bergmann, U.; Messinger, J.; Zouni, A.; Yachandra, V. K., High-Resolution Structure of the Photosynthetic  $\text{Mn}_4\text{Ca}$  Catalyst from X-ray Spectroscopy. *Phil. Trans. of Royal Soc. B: Biol. Sci.* **2008**, *363* (1494), 1139-1147.



102. McEvoy, J. P.; Brudvig, G. W., Water-Splitting Chemistry of Photosystem II. *Chem. Rev.* **2006**, *106* (11), 4455-4483.
103. Car, P.-E.; Guttentag, M.; Baldrige, K. K.; Alberto, R.; Patzke, G. R., Synthesis and Characterization of Open and Sandwich-Type Polyoxometalates Reveals Visible-Light-Driven Water Oxidation via POM-Photosensitizer Complexes. *Green Chemistry* **2012**, *14* (6), 1680-1688.
104. Wang, Z.; Helmersson, U.; Käll, P.-O., Optical Properties of Anatase TiO<sub>2</sub> Thin Films Prepared by Aqueous Sol–Gel Process at Low Temperature. *Thin Solid Films* **2002**, *405* (1), 50-54.
105. Jeba Beula, R.; Devadason, S.; Mahesh Kumar, V., Effect of Titanium Coating on the Structural and Optical Properties of TiO<sub>2</sub> Thin Films for Improved Performance in Dye-Sensitized Solar Cells. In *Recent Trends in Materials Science and Applications: Nanomaterials, Crystal Growth, Thin films, Quantum Dots, & Spectroscopy (Proceedings ICRTMSA 2016)*, Ebenezar, J., Ed. Springer International Publishing: Cham, 2017; pp 437-449.
106. Momeni, M.; Golestani-Fard, F.; Saghafian, H.; barati, n.; Khanahmadi, A., Development of Visible Light Activated TiO<sub>2</sub> Thin Films on Stainless Steel via Sol Spraying with Emphasis on Microstructural Evolution and Photocatalytic Activity. *Appl. Surf. Sci.* **2015**, *357*, 1902-1910.
107. Stefan, M.; Pana, O.; Leostean, C.; Bele, C.; Silipas, D.; Senila, M.; Gautron, E., Synthesis and Characterization of Fe<sub>3</sub>O<sub>4</sub>–TiO<sub>2</sub> Core-Shell Nanoparticles. *J. Appl. Phys.* 2014; Vol. 116, p 114312.

108. Dette, C.; Pérez-Osorio, M. A.; Kley, C. S.; Punke, P.; Patrick, C. E.; Jacobson, P.; Giustino, F.; Jung, S. J.; Kern, K., TiO<sub>2</sub> Anatase with a Bandgap in the Visible Region. *Nano Lett.* **2014**, *14* (11), 6533-6538.
109. Sreedhar, A.; Sreekanth, T. V. M.; Kwon, J. H.; Yi, J.; Sohn, Y.; Gwag, J. S., Ag Nanoparticles Decorated ion-Beam-Assisted Titanium dioxide Thin Films for Tuning the Water Splitting Activity from UV to Visible Light Harvesting. *Ceramics Int.* **2017**, *43* (15), 12814-12821.
110. Cao, C.; Hu, C.; Shen, W.; Wang, S.; Wang, J.; Tian, Y., Fabrication of a Novel Heterostructure Of Co<sub>3</sub>O<sub>4</sub>-Modified TiO<sub>2</sub> Nanorod Arrays and its Enhanced Photoelectrochemical Property. *J. Alloys Compd.* **2013**, *550* (Supplement C), 137-143.
111. Meng, A.; Zhu, B.; Zhong, B.; Zhang, L.; Cheng, B., Direct Z-scheme TiO<sub>2</sub>/CdS Hierarchical Photocatalyst for Enhanced Photocatalytic H<sub>2</sub>-production activity. *Appl. Surf. Sci.* **2017**, *422* (Supplement C), 518-527.
112. Palmas, S.; Polcaro, A. M.; Ruiz, J. R.; Da Pozzo, A.; Mascia, M.; Vacca, A., TiO<sub>2</sub> Photoanodes for Electrically Enhanced Water Splitting. *Int. J. Hydrogen Energy* **2010**, *35* (13), 6561-6570.
113. Macdonald, D. D., Reflections on the History of Electrochemical Impedance Spectroscopy. *Electrochim. Acta* **2006**, *51* (8-9), 1376-1388.
114. Chang, B.-Y.; Park, S.-M., Electrochemical Impedance Spectroscopy. *Annu. Rev. Anal. Chem.* **2010**, *3*, 207-229.
115. Orazem, M. E.; Tribollet, B.; Editors, *Electrochemical Impedance Spectroscopy*. John Wiley & Sons, Inc.: 2008; p 523 pp.

116. Bard, A. J.; Faulkner, L. R., *Electrochemical Methods: Fundamentals and Applications*. 2nd ed. ed.; John Wiley & Sons, Inc.: New York, 2001; p 736-745.
117. Langland, M., & Cronin, T. *A Summary Report of Sediment Processes in Chesapeake Bay and Watershed*. In *Water-Resources Investigations Report 03-4123*; New Cumberland, PA, 2003.
118. Costentin, C.; Passard, G.; Savéant, J.-M., Benchmarking of Homogeneous Electrocatalysts: Overpotential, Turnover Frequency, Limiting Turnover Number. *J. Am. Chem. Soc.* **2015**, *137* (16), 5461-5467.
119. Yang, Y.; Xu, D.; Wu, Q.; Diao, P., Cu<sub>2</sub>O/CuO Bilayered Composite as a High-Efficiency Photocathode for Photoelectrochemical Hydrogen Evolution Reaction. *Sci. Rep.* **2016**, *6*, 35158.
120. Cao, D.; Nasori, N.; Wang, Z.; Wen, L.; Xu, R.; Mi, Y.; Lei, Y., Facile Surface Treatment on Cu<sub>2</sub>O Photocathodes for Enhancing the Photoelectrochemical Response. *Appl. Catal. B: Environ.* **2016**, *198* (Supplement C), 398-403.
121. Hsu, Y.-K.; Yu, C.-H.; Chen, Y.-C.; Lin, Y.-G., Fabrication of Coral-Like Cu<sub>2</sub>O Nanoelectrode for Solar Hydrogen Generation. *J. Power Sources* **2013**, *242* (Supplement C), 541-547.
122. Hsu, Y.-K.; Yu, C.-H.; Chen, Y.-C.; Lin, Y.-G., Synthesis of Novel Cu<sub>2</sub>O Micro/Nanostructural Photocathode for Solar Water Splitting. *Electrochim. Acta* **2013**, *105* (Supplement C), 62-68.
123. Chen, Z.-G.; Han, G.; Yang, L.; Cheng, L.; Zou, J., Nanostructured Thermoelectric Materials: Current Research and Future Challenge. *Prog. Nat. Sci. Mater. Int.* **2012**, *22* (6), 535-549.

124. Yu, B.; Liu, W.; Chen, S.; Wang, H.; Wang, H.; Chen, G.; Ren, Z., Thermoelectric Properties of Copper Selenide with Ordered Selenium Layer and Disordered Copper Layer. *Nano Energy* **2012**, *1* (3), 472-478.
125. Gahtori, B.; Bathula, S.; Tyagi, K.; Jayasimhadri, M.; Srivastava, A. K.; Singh, S.; Budhani, R. C.; Dhar, A., Giant Enhancement in Thermoelectric Performance of Copper Selenide by incorporation of Different Nanoscale Dimensional Defect Features. *Nano Energy* **2015**, *13* (Supplement C), 36-46.
126. Yang, L.; Chen, Z.-G.; Han, G.; Hong, M.; Zou, Y.; Zou, J., High-Performance Thermoelectric Cu<sub>2</sub>Se Nanoplates through Nanostructure Engineering. *Nano Energy* **2015**, *16* (Supplement C), 367-374.
127. Neshkova, M.; Sheytanov, H., Ion-Selective Electrodes with Sensors of Electrolytically Plated Chalcogenide Coatings: Part I. Copper Ion-Selective Electrode based on Plated Copper Selenide. *J. Electroanal. Chem. Interfacial Electrochem.* **1979**, *102* (2), 189-198.
128. Chopra, K. L.; Paulson, P. D.; Dutta, V., Thin-Film Solar Cells: an Overview. *Prog. Photovoltaics Res. Appl.* **2004**, *12* (2-3), 69-92.
129. Jackson, P.; Hariskos, D.; Lotter, E.; Paetel, S.; Wuerz, R.; Menner, R.; Wischmann, W.; Powalla, M., New World Record Efficiency for Cu(In,Ga)Se<sub>2</sub> Thin-Film Solar Cells Beyond 20%. *Prog. Photovoltaics. Res. Appl.* **2011**, *19* (7), 894-897.
130. Jackson, P.; Würz, R.; Rau, U.; Mattheis, J.; Kurth, M.; Schlötzer, T.; Bilger, G.; Werner, J. H., High Quality Baseline for High Efficiency, Cu(In<sub>1-x</sub>,Ga<sub>x</sub>)Se<sub>2</sub> Solar Cells. *Prog. Photovoltaics. Res. Appl.* **2007**, *15* (6), 507-519.

131. Soriano-López, J.; Goberna-Ferrón, S.; Carbó, J. J.; Poblet, J. M.; Galán-Mascarós, J. R., Chapter Six -  $[\text{Co}_9(\text{H}_2\text{O})_6(\text{OH})_3(\text{HPO}_4)_2(\text{PW}_9\text{O}_{34})_3]^{16-}$ : A Highly Efficient Catalyst for Water Oxidation. In *Adv. Inorg. Chem.*, van Eldik, R.; Cronin, L., Eds. Academic Press: 2017; Vol. 69, pp 155-179.
132. Galán-Mascarós, J. R.; Gómez-García, C. J.; Borrás-Almenar, J. J.; Coronado, E., High Nuclearity Magnetic Clusters: Magnetic Properties of a Nine Cobalt Cluster Encapsulated in a Polyoxometalate,  $[\text{Co}_9(\text{OH})_3(\text{H}_2\text{O})_6(\text{HPO}_4)_2(\text{PW}_9\text{O}_{34})_3]^{16-}$ . *Adv. Mater.* **1994**, 6 (3), 221-223.
133. Palve, B. M.; Jagtap, C. V.; Bhalekar, V. P.; Jadkar, S. R.; Pathan, H. M., Synthesis of Crystalline Umangite Phase of Copper Selenide ( $\text{Cu}_3\text{Se}_2$ ) for  $\text{TiO}_2$  Photoanode-Based Solar Cell Application. *J. Solid State Electrochem.* **2017**, 21 (9), 2677-2685.
134. Bottecchia, O. L., A Model of the Growth of Copper Selenide Thin Films Controlled by Diffusion and Chemical Reaction. *J. Brazilian Chem. Soc.* **1998**, 9, 515-520.
135. Liu, F. W., Bo; Lai, Yanqing; Li, Jie; Zhang, Zhian; Liu, Yexiang Electrodeposition of Cobalt Selenide Thin Films. *J. Electrochem. Soc.* **2010**, 157 (10), D523- D527.
136. Kowalik, R.; Kazimierzak, H.; Żabiński, P., Electrodeposition Of Cadmium Selenide. *Mater. Sci. Semicond. Proc.* **2016**, 50, 43-48.
137. Zhao, Y.-F.; Yang, Z.-Y.; Zhang, Y.-X.; Jing, L.; Guo, X.; Ke, Z.; Hu, P.; Wang, G.; Yan, Y.-M.; Sun, K.-N.,  $\text{Cu}_2\text{O}$  Decorated with Cocatalyst  $\text{MoS}_2$  for Solar Hydrogen

- Production with Enhanced Efficiency under Visible Light. *J. Phys. Chem. C* **2014**, *118* (26), 14238-14245.
138. Lan, T.; Mundt, C.; Tran, M.; Padalkar, S., Effect of Gold Underlayer on Copper(I) Oxide Photocathode Performance. *J. Mater. Res.* **2017**, *32* (9), 1656-1664.
139. Qi, H.; Wolfe, J.; Fichou, D.; Chen, Z., Cu<sub>2</sub>O Photocathode for Low Bias Photoelectrochemical Water Splitting Enabled by NiFe-Layered Double Hydroxide Co-Catalyst. *Sci. Rep.* **2016**, *6*, 30882.
140. Soyoung, K.; Hyojin, K.; Soon-Ku, H.; Dojin, K., Fabrication and Photoelectrochemical Properties of a Cu<sub>2</sub>O/CuO Heterojunction Photoelectrode for Hydrogen Production from Solar Water Splitting. *J. Mater. Res.* **2016**, *26* (11), 604-610.
141. Ma, X.; Zhang, J.; Wang, B.; Li, Q.; Chu, S., Hierarchical Cu<sub>2</sub>O foam/g-C<sub>3</sub>N<sub>4</sub> Photocathode for Photoelectrochemical Hydrogen Production. *Appl. Surf. Sci.* **2018**, *427*, 907-916.
142. Zhang, L.; Wang, S.; Shao, Y.; Wu, Y.; Sun, C.; Huo, Q.; Zhang, B.; Hu, H.; Hao, X., One-Step Fabrication of Porous GaN Crystal Membrane and Its application in Energy Storage. *Sci. Rep.* **2017**, *7*, 44063.
143. Zhang, Y.; Feng, T.; Zhou, X.; Pei, Q.; Hao, T.; Zhang, W.; Wu, S.; Mao, H.; Song, X.-M., Facile Preparation of One Dimension ZnO/Chalcogenide Semiconductor Heterostructure for Efficient Photoelectrochemical Water Splitting. *J. Alloys Compd.* **2016**, *685*, 581-586.
144. Sun, H.; Guo, L.-Y.; Li, J.-S.; Bai, J.-P.; Su, F.; Zhang, L.-C.; Sang, X.-J.; You, W.-S.; Zhu, Z.-M., Two New Armtype Polyoxometalates Grafted on Titanium Dioxide

- Films: Towards Enhanced Photoelectrochemical Performance. *ChemSusChem* **2016**, *9* (10), 1125-1133.
145. Salavati-Niasari, M.; Davar, F., Synthesis of Copper and Copper(I) Oxide Nanoparticles by Thermal Decomposition of a New Precursor. *Mater. Lett.* **2009**, *63* (3), 441-443.
146. Derin, H.; Kantarli, K., Optical Characterization of Thin Thermal Oxide Films on Copper by Ellipsometry. *Appl. Phys. A* **2002**, *75* (3), 391-395.
147. Cui, J.; Gibson, U. J., A Simple Two-Step Electrodeposition of Cu<sub>2</sub>O/ZnO Nanopillar Solar Cells. *J. Phys. Chem. C* **2010**, *114* (14), 6408-6412.
148. Zhou, H.; Yu, F.; Huang, Y.; Sun, J.; Zhu, Z.; Nielsen, R. J.; He, R.; Bao, J.; Goddard Iii, W. A.; Chen, S.; Ren, Z., Efficient Hydrogen Evolution by Ternary Molybdenum Sulfoselenide Particles on Self-Standing Porous Nickel Diselenide Foam. *Nat. Commun.* **2016**, *7*, 12765.
149. Wang, F.; Li, Y.; Shifa, T. A.; Liu, K.; Wang, F.; Wang, Z.; Xu, P.; Wang, Q.; He, J., Selenium-Enriched Nickel Selenide Nanosheets as a Robust Electrocatalyst for Hydrogen Generation. *Angew. Chem. Int. Ed.* **2016**, *55* (24), 6919-6924.
150. Irshad, A.; Munichandraiah, N., Electrodeposited Nickel–Cobalt–Sulfide Catalyst for the Hydrogen Evolution Reaction. *ACS Appl. Mater. Interfaces* **2017**, *9* (23), 19746-19755.
151. Long, X.; Li, G.; Wang, Z.; Zhu, H.; Zhang, T.; Xiao, S.; Guo, W.; Yang, S., Metallic Iron–Nickel Sulfide Ultrathin Nanosheets as a Highly Active Electrocatalyst for Hydrogen Evolution Reaction in Acidic Media. *J. Am. Chem. Soc.* **2015**, *137* (37), 11900-11903.

152. Huang, M.-C.; Wang, T.; Chang, W.-S.; Lin, J.-C.; Wu, C.-C.; Chen, I. C.; Peng, K.-C.; Lee, S.-W., Temperature Dependence on p-Cu<sub>2</sub>O Thin Film Electrochemically Deposited onto Copper Substrate. *Appl. Surf. Sci.* **2014**, *301*, 369-377.
153. Wang, Z.; Xu, H.; Zhang, Z.; Zhou, X.; Pang, S.; Cui, G., High-Performance Cobalt Selenide and Nickel Selenide Nanocomposite Counter Electrode for Both Iodide/Triiodide and Cobalt(II/III) Redox Couples in Dye-Sensitized Solar Cells. *Chin. J. Chem.* **2014**, *32* (6), 491-497.
154. N. Gawale, R. M. M., A. M. Sargar, S. R. Mane, R. R. Kharade, P. N. Bhosale, Electrosynthesis and Characterization of WSe<sub>2</sub> Thin Films. *Archives. Appl. Sci. Res.* **2010**, *2* (1), 218-224.
155. Mahalingam, T.; Thanikaikarasan, S.; Dhanasekaran, V.; Kathalingam, A.; Velumani, S.; Rhee, J.-K., Preparation and Characterization Of MnSe Thin Films. *Mater. Sci. Eng. B* **2010**, *174* (1), 257-262.
156. Rahman, G.; Joo, O.-S., Electrodeposited Nanostructured  $\alpha$ -Fe<sub>2</sub>O<sub>3</sub> Thin Films for Solar Water Splitting: Influence of Pt Doping on Photoelectrochemical Performance. *Mater. Chem. Phys.* **2013**, *140* (1), 316-322.
157. Chen, P. Y.; Hu, S. F.; Liu, R. S.; Huang, C. Y., Electrodeposition Of Nano-Dimensioned Fese. *Thin Solid Films* **2011**, *519* (23), 8397-8400.
158. Jiang, N.; You, B.; Sheng, M.; Sun, Y., Electrodeposited Cobalt-Phosphorous-Derived Films as Competent Bifunctional Catalysts for Overall Water Splitting. *Angew. Chem. Int. Ed.* **2015**, *54* (21), 6251-6254.
159. Nguyen, N. T.; Altomare, M.; Yoo, J.; Schmuki, P., Efficient Photocatalytic H<sub>2</sub> Evolution: Controlled Dewetting–Dealloying to Fabricate Site-Selective High-Activity



- Nanoporous Au Particles on Highly Ordered TiO<sub>2</sub> Nanotube Arrays. *Adv. Mater.* **2015**, 27 (20), 3208-3215.
160. Yang, J.; Banerjee, A.; Guha, S., Amorphous Silicon based Photovoltaics—from Earth to the “Final Frontier”. *Sol. Energy Mater. Sol. Cells* **2003**, 78 (1), 597-612.
161. Chakthranont, P.; Hellstern, T. R.; McEnaney, J. M.; Jaramillo, T. F., Design and Fabrication of a Precious Metal-Free Tandem Core–Shell p<sup>+</sup>n Si/W-Doped BiVO<sub>4</sub> Photoanode for Unassisted Water Splitting. *Adv. Energy Mater.* **2017**, 7 (22), 1701515-n/a.
162. Bai, Z.; Zhang, Y., A Cu<sub>2</sub>O/Cu<sub>2</sub>S-ZnO/CdS Tandem Photoelectrochemical Cell for Self-Driven Solar Water Splitting. *J. Alloys Compd.* **2017**, 698, 133-140.
163. Gurudayal; Sabba, D.; Kumar, M. H.; Wong, L. H.; Barber, J.; Grätzel, M.; Mathews, N., Perovskite–Hematite Tandem Cells for Efficient Overall Solar Driven Water Splitting. *Nano Lett.* **2015**, 15 (6), 3833-3839.